MICRO-CT CHARACTERIZATION OF PORE-SIZE DISTRIBUTION AND EFFECTS ON MATRIX ACIDIZING

A Thesis

by

DAVID ALEXANDER DUBETZ

Submitted to the Office of Graduate and Professional Studies of
Texas A&M University
in partial fulfillment of the requirements for the degree of

MASTER OF SCIENCE

Chair of Committee,	Ding Zhu
Co-Chair of Committee,	Alfred Daniel Hill
Committee Members,	Yuefang Sun
Head of Department,	Alfred Daniel Hill

December 2016

Major Subject: Petroleum Engineering

ABSTRACT

Carbonate rocks have complex heterogeneities that result from syn- and post-depositional stressors. These heterogeneities invariably affect the movement of fluid through the formation. When considering an acid treatment procedure, care must be taken to optimize the acid concentration and pumping schedule to encourage the formation of wormholes. Despite the abundance of carbonate formations (60% of conventional reserves), there is little consensus on the effect of physical formation properties related to acidizing efficiency. This study characterizes the pore-size distribution for different carbonate rocks and evaluates how the optimum pore-volume to breakthrough, $PV_{bt,opt}$, and the optimal interstitial flux, $v_{i,opt}$, are related to various physical properties of the rock.

The pore-size distributions evaluated in this study are constructed with micro-computer tomography (micro-CT) imaging, a non-invasive X-Ray imaging technique pioneered in the medical field. Micro-CT is improved over medical CT because it can scan at higher energies and higher resolution. In this work, resolution for scanned samples are from 5-8 μm/voxel and sample sizes are approximately $1cm^3$. From the raw data, image processing is applied to distinguish pore space from the surrounding matrix. Object counter software is used to identify and measure individual pores, which can then be organized into a pore-size distribution. This study finds that the shape of the pore-size distribution is influenced by the type of carbonate rock, where the primary difference between scanned samples is their pore structure. Statistical parameters are calculated by fitting a lognormal distribution function to each sample's pore-size distribution.

ACKNOWLEDGEMENTS

I would like to thank my committee chair, Dr. Ding Zhu, and my committee members, Dr. A. Daniel Hill and Dr. Yuefang Sun, for their guidance, support, and patience throughout the course of this research.

Thanks to my friends, colleagues, and department faculty and staff for making my time at Texas A&M University a memorable experience. I would especially like to thank Kai Dong for his early guidance when I first arrived to the University, Haoran Cheng and Jordan Etten for contributions to experimental portions of this work, and Don Conlee for support with micro-CT scanning and software advice. I also extend my gratitude to the Acid Stimulation Research Program (ASRP) partners for their financial support during the course of this research.

Finally, I would like to thank my family for their love, advice, and constant support through some difficult times during my studies at Texas A&M University.

NOMENCLATURE

A	Cross-sectional area of core, cm^2
B	Formation volume factor, dimensionless, RB/STB
C_v	Coefficient of variation, dimensionless
d	Wormhole diameter, cm
d_f	Fractal dimension, dimensionless
f	Porosity field fluctuation, dimensionless
h	Reservoir thickness, ft
k	Permeability, md
L	Wormhole length, cm
p_e	Reservoir pressure, psi
p_{wf}	Bottomhole flowing pressure, psi
PV_{bt}	Pore volumes to breakthrough
$PV_{bt,opt}$	Optimum pore volumes to breakthrough, dimensionless
N_{Da}	Damkohler number, dimensionless
N_{Pe}	Peclet number, dimensionless
q	Volumetric flow rate, cm^3/min
r_e	Wellbore drainage radius, ft
r_w	Wellbore radius, ft
s	Skin factor, dimensionless
v_i	Interstitial velocity, cm/min
$v_{i,opt}$	Optimum interstitial velocity, cm/min
x	Pore diameter, μm

Greek

κ	Overall dissolution rate constant cm/s

ϕ	Porosity, dimensionless
ϕ_0	Initial porosity, dimensionless
η	Viscosity, cp
μ	Lognormal distribution location parameter, dimensionless
σ	Lognormal distribution shape parameter, dimensionless
ψ	Pore growth rate (cm/min)

TABLE OF CONTENTS

Page

LIST OF FIGURES

Page

LIST OF TABLES

Page

CHAPTER I

BACKGROUND AND LITERATURE REVIEW

1.1 – Background: Carbonate Matrix Acidizing

Matrix acidizing is a well stimulation technique applicable to both sandstone and carbonate formations in which acids are pumped into the reservoir below fracture pressure in an effort to remove near-wellbore damage. In carbonate formations, acidizing is additionally effective due to the highly reactive nature of calcite with strong acid, such as HCl. Under correct conditions, this reactivity facilitates the creation of high-conductivity channels extending far beyond the near-wellbore region. These channels are called wormholes, which act as low-resistance pathways through which fluids can be produced more effectively than through non-stimulated matrix. Wellbore damage can originate from a variety of sources such as fines migration, scale buildup, or perforation damage**.** These near-wellbore damages, regardless of their origin, can be grouped into a concept called skin factor, which acts as a limiting pressure drop at the wellbore.

For a well operating under steady-state conditions, the radial inflow function for porous media is displayed in oilfield units as **Eq 1.1.**

$$P_e - P_{wf} = \frac{141.2qB\eta}{kh}\left(ln\frac{r_e}{r_w} + s\right) \quad (1.1)$$

Where (P_e –P_{wf}) is the pressure difference between the bottomhole and surface (psi)**,** q is the volumetric flow rate in STB/d, η is fluid viscosity in cp, k is permeability in md, h is the vertical height of the pressure head in ft**,** r_e is the extent of the drainage radius in ft, r_w is the wellbore radius in ft, B is the formation volume factor, which can vary with different oils and converts STB into res bbl, and s is the aforementioned skin factor (unitless).

Rearranged to show the effect of parameters on q, the production flow rate, **Eq 1.2** is formed

$$q = \frac{kh(p_e - p_f)}{141.2B\eta\ (\ln\frac{r_e}{r_w} + s)} \quad (1.2)$$

One takeaway from **Eq 1.2** is that a negative value of skin increases production yield, q, if all other variables remain equal. Well stimulation is a broad technique to reduce the skin factor thereby increasing productivity of damaged wells. Another observation is the semi-logarithmic nature of the above equations, which means the effects of skin damage are greatly magnified closer to the wellbore.

Due to the high surface reaction rate between HCl and carbonate, mass transfer limits the overall reaction kinetics. This leads to a non-uniform etching pattern as acid is injected, and thus couples the dissolution pattern to the acid injection rate. The unique shape of a wormhole at a given injection rate depends on the rock pore structure. Field studies have shown wormholing to be an effective method for reducing skin factor (Glasbergen et al., 2009; Economides et al., 2012). Selected acidized carbonate reservoirs in the Middle East and North Sea have reported an average post-acidizing skin of -4, which suggests wormhole penetration of up to 20 ft and significant production enhancement (Furui et al., 2010).

As mentioned, acid injection rate plays an important role in wormhole formation and thus a science has grown around attempting to understand wormhole propagation and optimize field treatments. The relationship between dissolution structure and acid flow rate is such that there exists an optimum injection rate at which wormholes form. This is called the optimal acid injection rate, and can be visualized on an acid efficiency curve, such as the one presented in **Fig. 1.1.** Pore volumes to breakthrough (PV_{bt}) is defined as the volume of acid required to channel through a core, divided by the volume of pores in the core. In other words – the amount of acid needed to break through the core, measured in pore volumes. Note a global minimum on the plot, which indicates the minimum acid volume ($PV_{bt,opt}$) for core breakthrough takes place at a characteristic interstitial acid velocity, $v_{i,opt}$. The interstitial velocity is related to the injection velocity and is an average of the acid velocity within the porous rock.

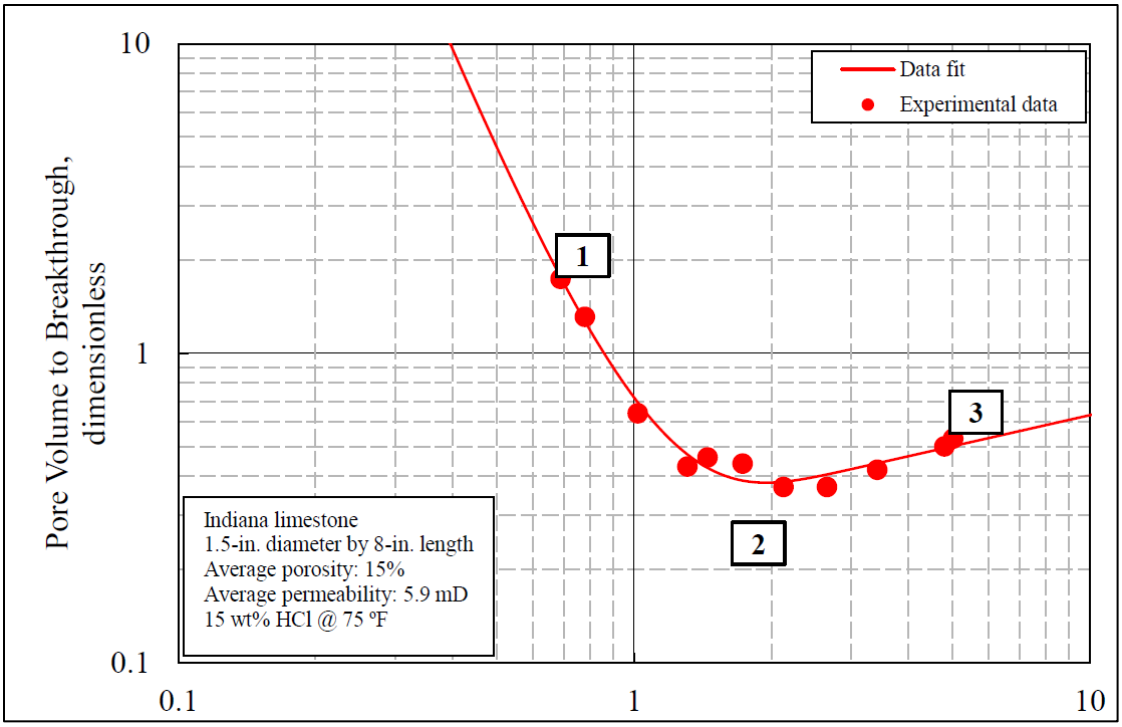

Figure 1.1: *Acid efficiency curve showing optimum point. This occurs where both* x *and* y*-axis values (*$v_{i,opt}$ *and* $PV_{bt,opt}$*, respectively) are at a minimum. The datapoints are fit using the Buijse & Glasbergen method to determine the optimum parameters. (Modified from Dong et al., 2012)*

If interstitial velocity is lower than the optimum, a significant amount of acid is wasted before breakthrough is achieved. This is shown by the steep slope of the curve labeled "1" in **Fig. 1.1** (note the log-log axes). Above $v_{i,opt}$, (label "3") the slope is significantly decreased, but still not optimum. Since determining the optimum rate is difficult, common field practice is to inject acid at the maximum allowable rate below the fracture pressure of the formation.

1.2 – Literature Review

The following section provides a review of literature pertinent to the field of matrix acidizing and digital analysis of micro-CT imaging of geologic media.

1.2.1 – Pore Enlargement and Wormhole Formation Models

One of the important impacts on acidizing performance is the pore structure of the rock. As acid is injected, it flows naturally into the highest-permeability regions. A dissolution reaction occurs and the pore structure is changed in a complex manner. Macro-scale properties, such as porosity and permeability, are altered during the dissolution process. To study this process more closely, Schechter and Gidley (1969) modeled the evolution of pore-size distribution and the permeability enhancement of rock resulting from surface reaction. They mathematically defined a rock model as a bundle of capillary tubes, which were allowed to enlarge and merge as dissolution proceeded. Input parameters include the pore-size distribution of the rock, which was discovered to have a large influence on the pore-growth process. The study concluded that larger pores have mass-transfer limited kinetics, which causes them to grow more quickly than smaller pores. Smaller pores do not readily receive acid and thus are reaction-limited. The pore growth functions from this study, and importance of the pore-size distribution, influenced subsequent authors to publish carbonate acidizing models based on similar principles.

Hung et al. (1989), produced a capillary tube-based model that described wormhole tip propagation as a strong function of injection rate, diffusion coefficient (for radial flow), and fluid loss along the wormhole walls. They concluded that wormhole length increases with injection rate, wormhole competition has an effect on growth rate, and they further suggested that large pores are most important in formation of wormholes. This model requires the pore-size distribution as an initial condition. Some limitations include that the model is only applicable for mass-transfer limited systems, capillary tubes are not allowed to collide, and the acid concentration at the wormhole tip is assumed to be the same as the concentration in the wellbore.

Hoefner & Fogler (1989) used a network model to simulate wormhole formation. In actuality, the network model is similar to previously-mentioned capillary tube models. They concluded that wormholes form only in diffusion/mass-transfer limited reactions. They also found that wormhole

formation is governed by the Damkohler number: defined as the ratio of net rate of dissolution to the rate of transport by convection. The net rate of dissolution is the rate of mass transfer for mass-transfer limited systems, or the rate of surface reaction for reaction-rate limited systems. This network model (and others in general), while showing good agreement with experimental results, cannot be scaled to even core-scale without requiring enormous computational power.

Later work by Fredd & Fogler (1998, 1999) investigated a wide range of fluid/mineral systems including dissolution of calcite by strong acids, weak acids, and chelating agents. They concluded that the formation of wormholes is governed by the Damkohler number for all fluid/mineral systems involved. The Damkohler approach is advantageous because it can be applied to mixed-kinetics reactions, unlike previous models which assumed mass-transfer limited kinetics. As quantitatively defined by Fredd & Fogler, the Damkohler number is shown in **Eq. 1.3**

$$N_{Da} = \frac{\pi\, d\, L\, \kappa}{q} \quad \text{.....(1.3)}$$

Where q is the flow rate in the wormhole, d and L are diameter and length of the wormhole, respectively, and κ is the overall dissolution rate constant. This constant is a function of various transport and reaction processes, and includes within it whether the reaction is mixed-kinetics, mass-transfer limited, or reaction-limited.

Wang et al. (1993), extended the work of Schechter & Gidley (1969) by using their pore-growth functions to define a transition pore size. Pores larger than this size exhibit mass-transfer limited kinetics and thus follow a growth function that allows them to become wormholes as dissolution progresses. The transition pore size is a function of the Damkohler number, mean pore length, and permeability. Smaller pores are defined by a separate growth function, and are not able to form wormholes until they reach the transition pore size (**Fig. 1.2**).

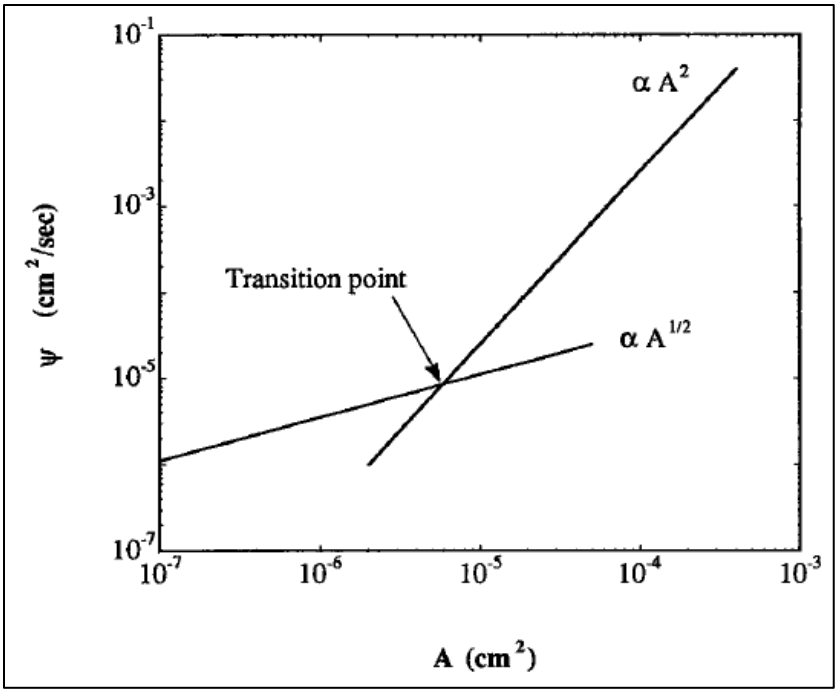

Figure 1.2: *Two pore growth functions with transition point shown. The A^2 function is mass-transfer limited, and pores following this function can become wormholes. (Wang et al., 1993)*

This study concluded that an optimum injection rate exists at which wormholing occurs, and this optimum depends on minerology, acid concentration, and reaction temperature. Again, this model emphasizes the importance of large pores and thus requires the pore-size distribution to determine how a rock will react to acidizing. The Wang et al. model is capable of predicting the optimum injection rate required for wormholing in linear corefloods, but cannot estimate the required acid volume ($PV_{bt,opt}$). It also cannot be applied to monitor skin evolution during treatment.

Huang et al. (1997) improved the transition-pore approach presented by Wang et al. (1993) by including a fluid loss model (based on Hung et al., 1989) and the effect of fluid competition on wormhole tip propagation. The main application for this was to upscale the Wang et al. (1993) model to field-scale. According to the Huang et al. (1997) study, the observed optimal acid flux from experiments compared well with values predicted by the transition pore theory model. This model has similar limitations to the original Wang et al. (1993) model.

Daccord et al. (1989) studied patterns of water injected into plaster to simulate a radial wormhole propagation process. They quantified wormholes by their equivalent hydraulic length, and demonstrated the fractal nature of wormhole structures formed under mass-transfer limited conditions. This model is fundamentally different from those previously mentioned due to consideration of the entire wormhole structure as fractals. The model shows that propagation of wormholes in radial systems is a function of the Peclet number $N_{Pe}^{(-1/3)}$, injected volume, and the fractal dimension (d_f). Peclet number is defined as the ratio of acid convection to diffusion. Their model only applies to mass-transfer limited systems, but does predict the existence of an optimum injection rate. The Daccord et al. (1989) model also predicts that a narrow pore-size distribution increases the width of acidized channels and these channels become more homogeneously etched (See **Fig. 1.3**) compared to a rock with a wider pore-size distribution.

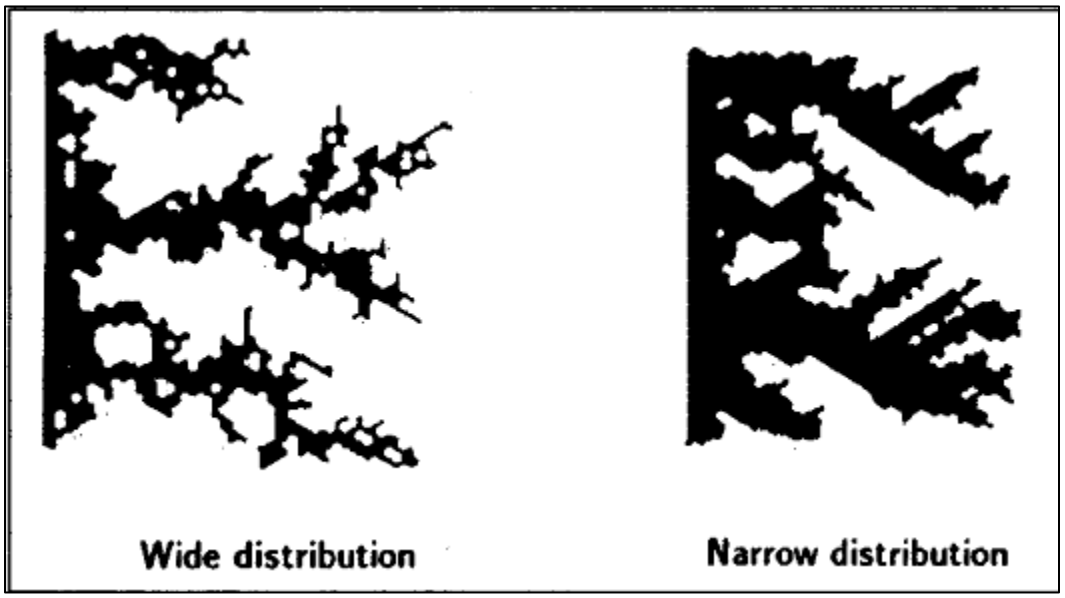

Figure 1.3: *Numerical simulations by Daccord et al. (1989) show the effect of pore-size distribution width on dissolution pattern. This image is from the linear application of the Daccord et al. model. Similar results were found for the radial case. (Daccord et al., 1989)*

Depending on what one wishes to accomplish with a model (monitor skin evolution during treatment, wormhole propagation estimate, or dissolution structure simulation), some models prevail in usefulness over others and model combinations are also possible. This section has described briefly some of the important models in matrix acidizing, with an emphasis on those that utilize pore-size distribution in some fashion. The next section will focus on optimal acidizing conditions ($PV_{bt,opt}$ & $v_{i,opt}$), models that estimate these parameters, and how heterogeneity and other pore-structure effects may influence the acidizing procedure. For a more detailed categorization and review of matrix acidizing models, the reader is referred to Fredd & Miller (2000) and Akanni & Nasr-El-Din (2015).

1.2.2 – Prediction of Optimum Flux and Pore-Volumes to Breakthrough

The presence of an optimum acid flux ($v_{i,opt}$) and acid volume ($PV_{bt,opt}$) has encouraged many studies in this area attempting to predict these values. Numerous studies have published findings illustrating the existence of the optimum condition (Wang et al., 1993; Fredd & Fogler, 1998; Bazin, 2001; and Buijse & Glasbergen, 2005). Factors affecting the location of the optimum point include temperature, acid type, and rock minerology.

Buijse & Glasbergen (2005) developed a semi-empirical model which requires the results of laboratory experiments to define an optimum interstitial velocity and corresponding pore-volume to breakthrough. The advantage of this semi-empirical approach is that the model is relatively simple in nature, with all complex rock/fluid dependencies contained in a parameter calculated from experimental data. The main output of the model is a curve-fit of experimental acidizing results, which can easily be used to find the optimum conditions. The disadvantage of this approach is that lab corefloods (or published literature) must be available for any and all fluid/mineral systems to be investigated. The Buijse & Glasbergen (2005) model was modified in a later study to account for radial and spherical flow and to allow for upscaling to field conditions (Furui et al., 2010).

A separate class of model has recently been developed called a two-scale continuum model. The 2D application of this model was demonstrated by Panga et al. (2005), which simulates reaction

and transport mechanisms of wormholing in carbonates. The two scales indicated by the model are Darcy-scale and pore-scale. Pore-scale phenomena are coupled to macroscopic variables (such as Darcy velocity) and structure-property relationships (such as porosity vs. permeability) to account for the relationship between pore and Darcy-scale. The pore-scale parameters are ultimately modeled by a dimensionless variable called the Thiele modulus (defined as the ratio of diffusion time to reaction time), which is coupled to a Damkohler-based model for core-scale characteristics. Full mathematical details of the model, which is limited to linear flow and two dimensions, can be found in Panga et al. (2005). The model was used to investigate the impact of heterogeneity on acidizing results. Porosity of each simulation grid cell is defined by summing a random number to global, averaged porosity of the medium. The random numbers are chosen based on a uniform distribution. Changing the bounds of the uniform distribution affects the limits of the porosity function, and thus the spatial heterogeneity of the simulated medium. This is shown mathematically in **Eq. 1.4**

$$\phi = \phi_0 + \hat{f} \quad \text{.....(1.4)}$$

In other words, each simulation grid cell is assigned a porosity, ϕ, based on a global porosity ϕ_0, plus a uniformly-distributed fluctuation function, *f*. Based on this definition of heterogeneity, the model predicts higher degrees of branching at higher heterogeneities (i.e., wider bounds on the uniform distribution function, *f)*. Results are shown in **Fig. 1.4.** Conclusions are in accordance with previously-discussed simulations by Daccord et al. (1989) on the effects of pore-size distribution width on dissolution shape (**Fig. 1.3)**.

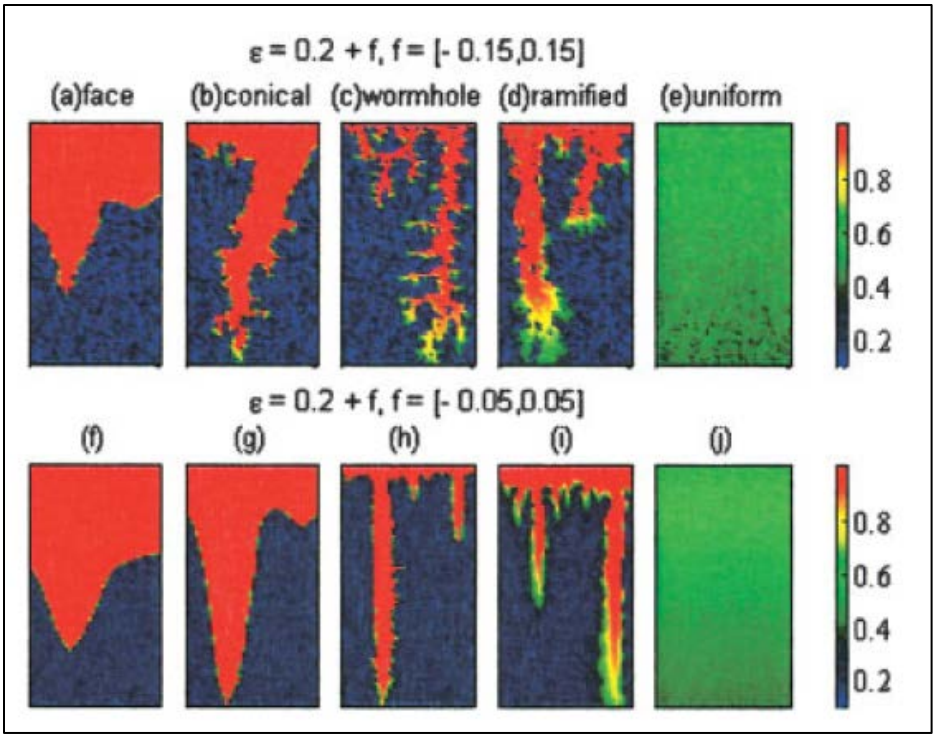

Figure 1.4: *Porosity profiles at different injection velocities with fluctuations in initial porosity distribution. Cases a-e have a wider porosity distribution (f=[-0.15,0.15]), compared with cases f-j (f=[-0.05,0.05]). The degree of fluctuation in porosity distribution is uniformly distributed in both cases, and used as a measure of rock heterogeneity. (Panga et al., 2005).*

An important observation is that, based on this model, changing heterogeneity magnitude affects wormhole structure/branching but does not change the category of dissolution pattern (conical, ramified, uniform, etc.) at a given injection rate. An acid efficiency curve generated for the above case indicates almost identical $PV_{bt,opt}$ and $v_{i,opt}$ for both variations of heterogeneity magnitudes. Thus, a conclusion of this study is that the magnitude of heterogeneity affects wormhole branching, but its influence on optimum conditions is negligible. This model was extended to the radial case by Kalia & Balakotaiah (2006) and similar results were found**.**

Maheshwari et al. (2013) extended the continuum model to 3D, and found similar effects of heterogeneity on dissolution shape and optimum acidizing properties. Heterogeneity in this case was modeled the same way as in the original Panga et al. (2005) paper, with a uniformly-distributed random

modifier to a global average porosity (**Eq. 1.4).** Also in this study, the effect of medium permeability was studied. This permeability is similar to the typical "average" permeability value measured for a given rock. Results of the simulation are shown in **Fig. 1.5.** Note that $PV_{bt,opt}$ increases while $v_{i,opt}$ decreases as permeability rises.

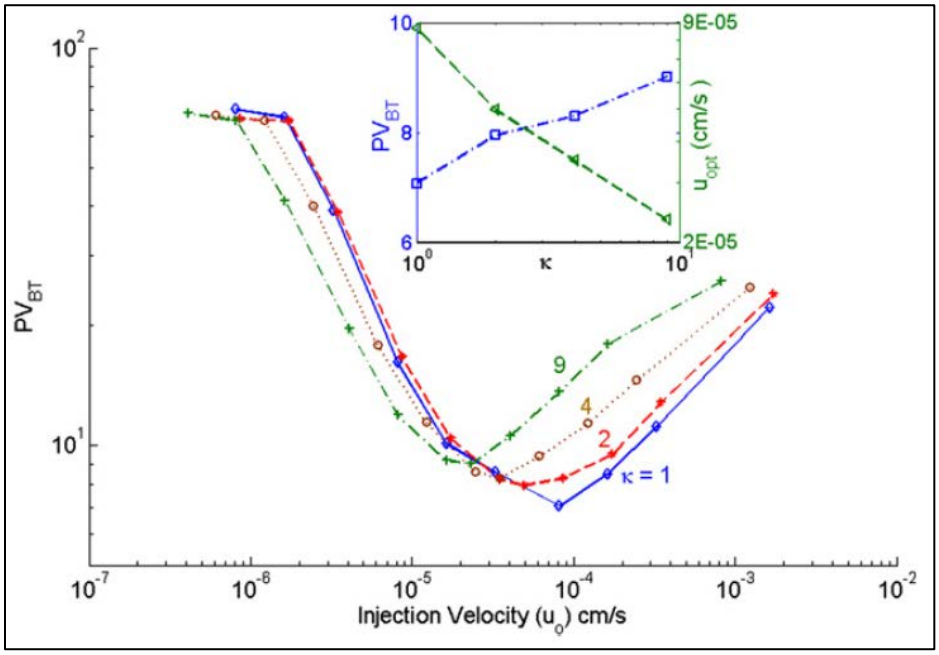

Figure 1.5: *Effect of initial permeability (κ) on the optimum injection rate and pore volumes to breakthrough. The insert shows the effects of κ on optimum values of both PV_{bt} and v_i (Maheshwari et al., 2013).*

Liu et al., (2012) extended the Panga et al. (2005) model by comparing the effect of the heterogeneity magnitude measured with a uniform distribution versus a normal distribution. Results of this simulation are shown in **Fig. 1.6**

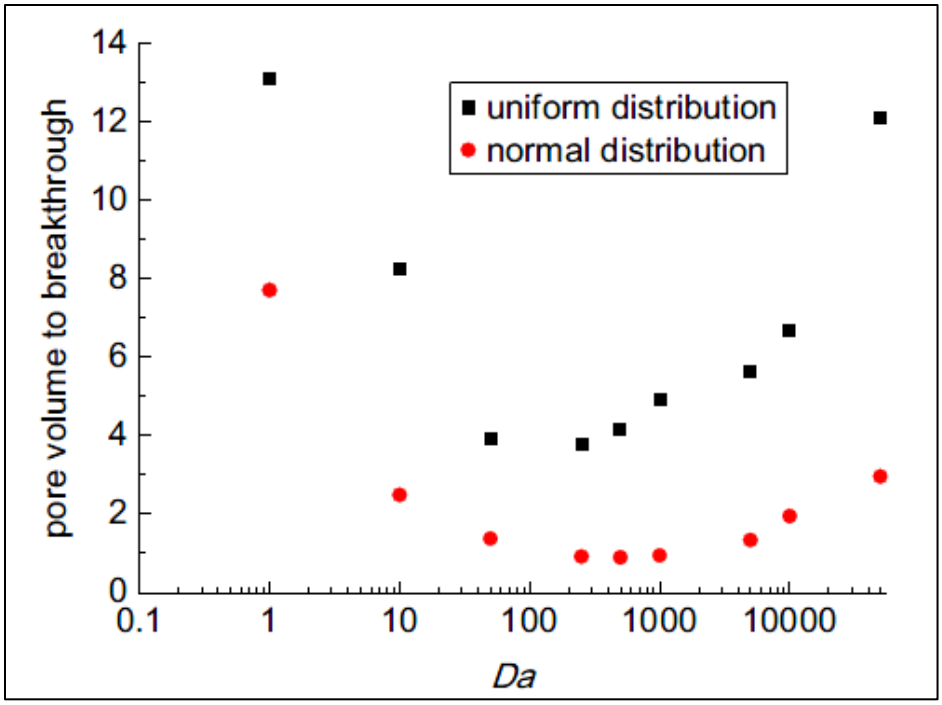

Figure 1.6: *Simulated acid efficiency curves for two different porosity generation methods using the two-scale continuum model of Panga et al. (2005). "Da" is the Damkohler number. (Liu et al., 2012).*

As can be clearly seen, choice of porosity distribution influences the $PV_{bt,opt}$ and Damkohler number. Note that the Damkohler number is inversely proportional to v_i, as shown in **Eq. 1.3**, where q in that equation is proportional to v_i**.** Thus, while results from the original two-scale continuum model seem to indicate that heterogeneity magnitude negligibly affects optimum conditions, the choice of distribution on which porosity is modeled may explain this result. Different rocks exhibit different porosity distributions, so the effect of pore structure on optimum conditions still holds true.

Ziauddin & Bize (2007) took an alternative approach to investigating heterogeneity effects by assigning carbonates into several reservoir rock types based on their geological features. Attempts to classify rocks has a long history, and the classification scheme adopted in this study is similar to the one by Lucia et al. (1999). Ziauddin & Bize (2007) found that carbonates grouped into a certain rock type had unique acidizing efficiency curves compared to carbonates assigned to other groups. This

opens the possibility of forgoing explicit modeling and instead using geological categorizations to estimate optimal conditions. While categorization systems seem promising, the process is labor-intensive (requiring manual analysis of thin-sections) and the complexity of carbonates do not lend themselves well to clear-cut categorization. Furthermore, the differences in displayed acid efficiency curves as a function of rock type are questionable (see **Fig. 1.7**). Despite this, rocks in different categories were found to show different dissolution patterns at a given injection rate which further suggests the importance of pore structure on both dissolution pattern and optimum conditions. 15 wt.% HCl was used in this study for all dissolution tests. In a separate plot, Winterset, Indiana, and Texas Cream limestone permeability evolution during acidizing versus porosity was found to be significantly different for these three rock types. Permeability evolution in Indiana and Winterset Limestones increased rapidly, while the Texas Cream plot shows hardly any permeability evolution during the acidizing process, again suggesting the importance of pore structure in acidizing performance. The reader is referred to Ziaudden & Bize (2007) for more details on rock characterization methods.

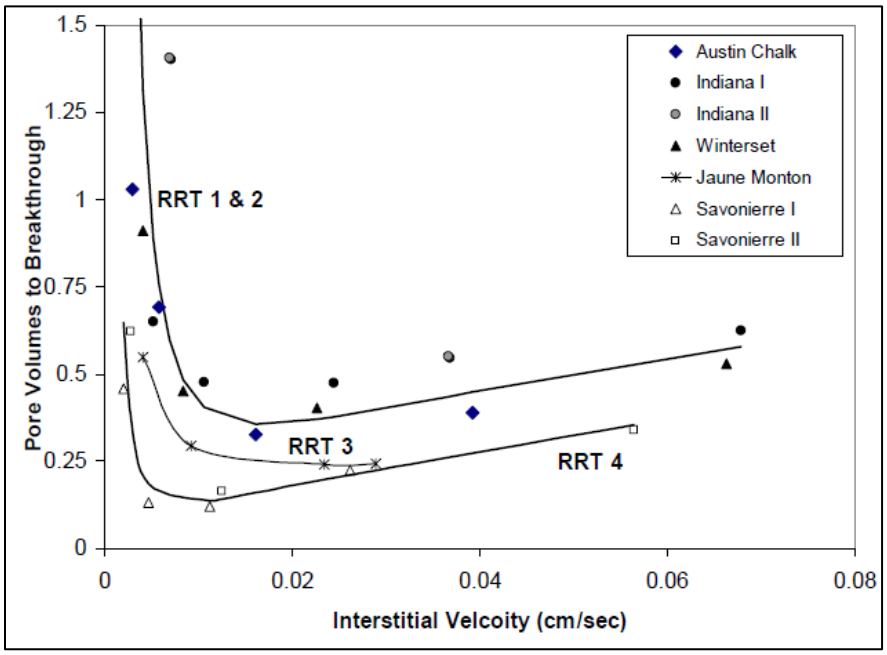

***Figure 1.7**: Acid efficiency curves for different carbonate rock categories. Four categories are shown in the image, but six are defined in the study (Ziaudden & Bize, 2007).*

Izgec et al. (2010) investigated the effect of large-scale heterogeneities (vugs) on optimum acidizing parameters of carbonate cores. This study found that acid propagates more efficiently (lower $PV_{bt,opt}$) through carbonate cores as the vug porosity fraction increases. Two measures of heterogeneity were used in this study. One is the coefficient of variation, C_v, which is proportional to the standard deviation as a fraction of the mean porosity of each CT slice. The value of C_v should remain about the same for each CT slice for homogenous cores, while vuggy cores are represented by drastic changes in the C_v value. A second measure of heterogeneity used was the variogram, which takes into account spatial correlation of pores along the core**.** A higher value of variability indicates a higher degree of spatial correlation (i.e. a value of zero indicates spatial randomness). These two measures, along with computed tomography analysis, were used to conclude that acid preferentially followed the path of the vug system as it channeled through the core. This result emphasizes the importance of spatial aspects of the pore system in carbonate acidizing. The study by Izgec et al. (2010) also attempted to construct an acid efficiency curve from the vuggy carbonate cores, but ultimately was unable to find the optimum values. Results from corefloods of vuggy carbonates are shown in **Fig. 1.8.** Izgec postulated that the optimum flux ($v_{i,opt}$) was much lower than those observed in homogeneous rocks, and thus the injection rates used in his experiments were too high to find this optimum on the plot.

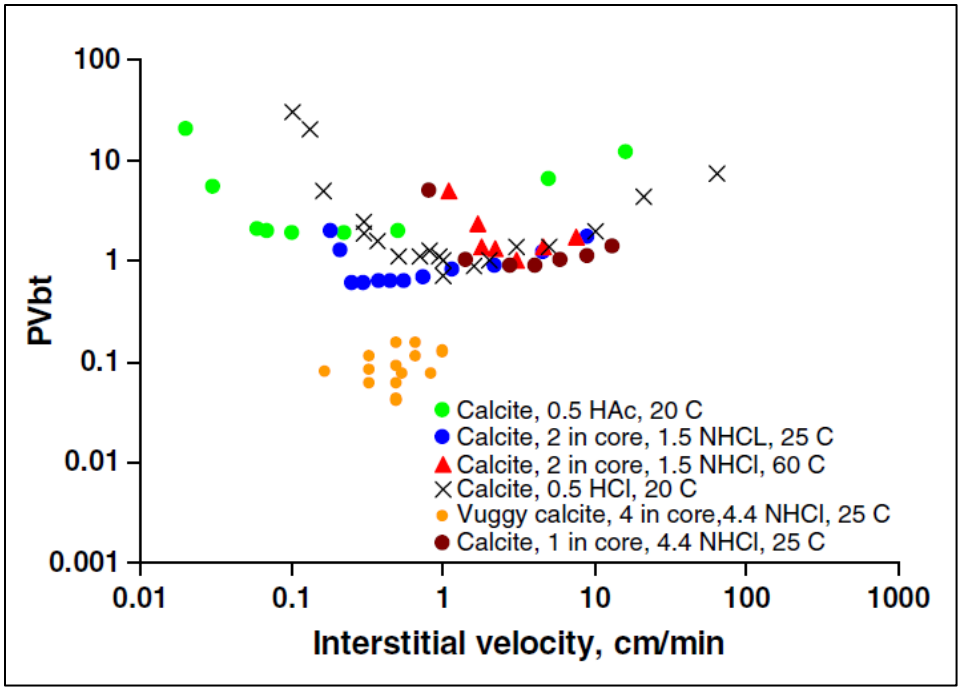

Figure 1.8: *Acid efficiency curve for vuggy calcite (orange points). Data from Wang et al. (1993) and Buijse & Glasbergen (2005) plotted for comparison. No optimum conditions were found for vuggy calcite. (Izgec et al., 2009)*

Etten et al. (2015) performed a study attempting to determine the effect of permeability on optimum acidizing conditions. In this study, efficiency curves were generated for limestone core samples of four different permeabilities, ranging from 6 md to 239 md. Three of the core sets were Indiana limestone, while a fourth of intermediate permeability (33 md) was Desert Pink limestone. Acidizing results fitted with the Buijse & Glasbergen model are shown in **Fig. 1.9.** Permeability was found to be logarithmically proportional to $PV_{bt,opt}$, regardless of rock type. The values of $v_{i,opt}$ increase with permeability up to the 239 md sample, at which point the optimum flux decreases to a lower value. Since determining the value of optimum conditions requires many acidizing experiments, it is important to ensure permeability and porosity values remain relatively constant for each curve. In the Etten et al. (2015) study, this condition is met for the lower-permeability samples but the 239 md conditions have a standard deviation of 132 md among the 6 cores used to create the breakthrough curve. This adds

uncertainty to the values of optimum conditions for the 239 md sample. Other than simple permeability and porosity measurements, no further attempts at quantifying rock heterogeneity were made in this study.

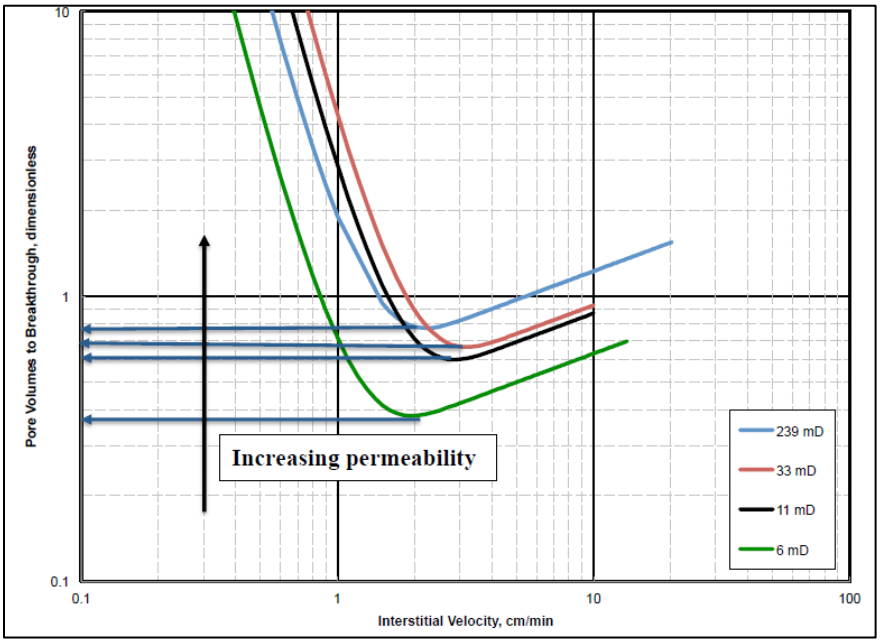

Figure 1.9: *Acid efficiency curves for four core sets fit with the Buijse & Glasbergen model. Three of the core sets were Indiana Limestone, while a fourth (33md) was Desert Pink limestone. (Etten et al., 2015).*

Zakaria et al. (2015) performed a study to predict the acidizing performance of various carbonates based on differences in their pore structure connectivity. This difference was quantified by measuring concentration of an effluent tracer after injection of the tracer through the core. Higher concentrations of the tracer in the effluent was said to mean the rock has higher comparative flow capacity, which was subsequently compared with core acidizing performance via acidizing efficiency curves. Residence time of tracer in the rock was also used as a quantitative measure of acidizing performance. For acidizing performance tests, 15 wt.% HCl was used. Carbonates with higher heterogeneity were found to have a larger flowing fraction, and thus a higher $PV_{bt,opt.}$ It is not clear if there is a difference between flowing fraction and permeability, which is known to increase with $PV_{bt,opt}$

as shown in Bazin (2001) and Etten et al. (2015). In any case, the study concludes that pore-scale heterogeneity has a significant impact on optimum acidizing conditions.

While current models can predict optimum conditions at lab-scale, upscaling to field-scale still presents problems. One manifestation of this is the dependency of optimal properties on core size for linear acidizing experiments. Research by Dong (2012) indicates a critical length at which point the $v_{i,opt}$ parameter is no longer affected by the length of the core (See **Fig. 1.10).**

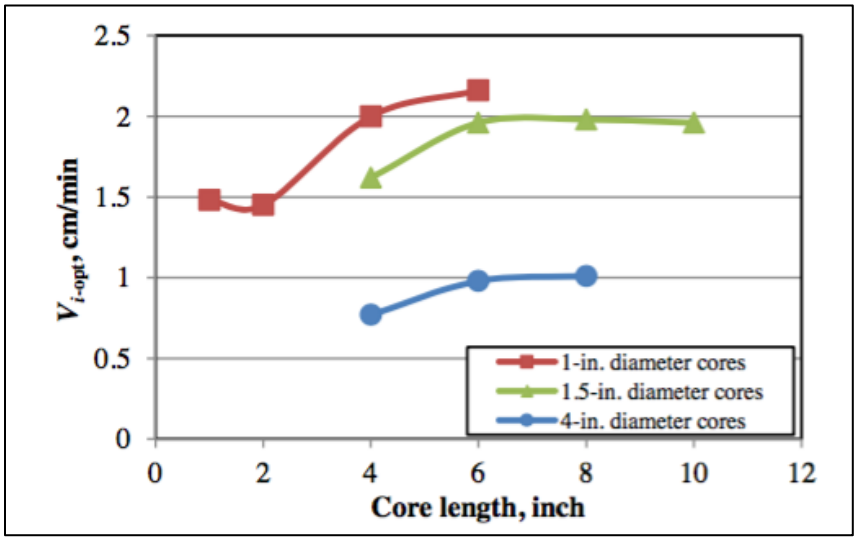

Figure 1.10: *Core-size effect on optimum flux. The dependency is noted up to a certain core length, after which the optimum value stabilizes (Dong, 2012)*

In addition to core length, core diameter also has an effect on optimum properties. Furui et al., (2010) showed that $v_{i,opt}$ and $PV_{bt,opt}$ decrease as the core diameter increases. While the reasons for core-size dependency on optimum parameters are not entirely understood, Dong (2012) postulates that it is due to wormhole competition effects, while Buijse (2000) found similar results but concluded that the dependency was due to boundary effects of the core itself. Nevertheless, it is clear that optimum acidizing parameters are sensitive to a variety of factors, including properties of the rock, fluid, flow geometry, reservoir geometry, and pore structure.

1.2.3 – Micro-CT Image Acquisition and Digital Image Processing

Pioneered in the medical field in the 1970s, computed tomography (CT) has a long history of research behind it. The main designation between medical CT and micro-CT is the higher energy used in the latter process, which would expose patients to unhealthy amounts of radiation. Higher energy allows for higher magnification, hence the "micro" designation. CT scanners work in principle by emitting X-rays at a target (the sample) while a receiver behind the sample measures the attenuation of the X-rays as they pass through the sample material. Since X-ray attenuation is density-dependent, a greyscale image is output where high-density objects are shown as bright, and low-density objects (such as air or liquid-filled pores) show up darker. The output greyscale image provides a relative measure of the sample density, though in micro-CT there is no equivalent to the Hounsfield scale where a precise density can be determined based on greyscale values. For application to petroleum engineering, the idea is to segment air-filled pore spaces from the rock matrix, thus acquiring a map of the rock pore structure.

While this may sound simple in rocks with clearly-defined boundaries such as sandstones, carbonates are much more challenging to segment properly. There are a few reasons for this. Firstly, the subsurface geology of carbonate formations often erases easily defined boundaries between matrix and pore space. Additionally, carbonates tend to contain a microporosity element that is below the resolution of micro-CT scanners, assuming a reasonable sample size (1 cm^3) is desired to be imaged. Thus, the boundary between pores and matrix is often blurred and post-process filtering is required to enhance contrast for accurate segmentation. In this work, "segmentation" refers to the process of differentiating between pore and matrix space in the sample.

Ruzyla (1986) provided an early review of methods for quantifying pore-scale features from digital images. Key topics discussed in this work are the process of image binarization, calculation of digital porosity, construction of pore-diameter distributions, and measures for quantifying pore shapes. While this study used thin-sections to discuss the aforementioned topics, the results remain important

for 3D images from micro-CT and image processing in general. Of the aforementioned subjects discussed, one of the most important is the binarization procedure. Binarization refers to the process of reducing a greyscale image, which contains 255 shades of grey for an 8-bit image, to a binary image – one that contains only two colors, or intensity values. The result of an ideal binarization procedure should highlight pore space as one of the two colors and matrix space the other color. A binary image is an important starting point for image analysis, and some macro-scale features, such as porosity, can be directly calculated from the binary image. From now on, we define pore space as black and matrix space as white in a binary image. In this case, the porosity of an image can simply be defined as the ratio of black pixels to white pixels. In a 3D object, a pixel becomes a voxel and the porosity measurement is attained in the same manner. The process of binarization is not straightforward. The procedure will often use the greyscale histogram as a means to properly segment pores from matrix. They greyscale histogram is a plot of pixel grey levels versus their frequency in an image. An idealized grey-level histogram is shown in **Fig. 1.11.**

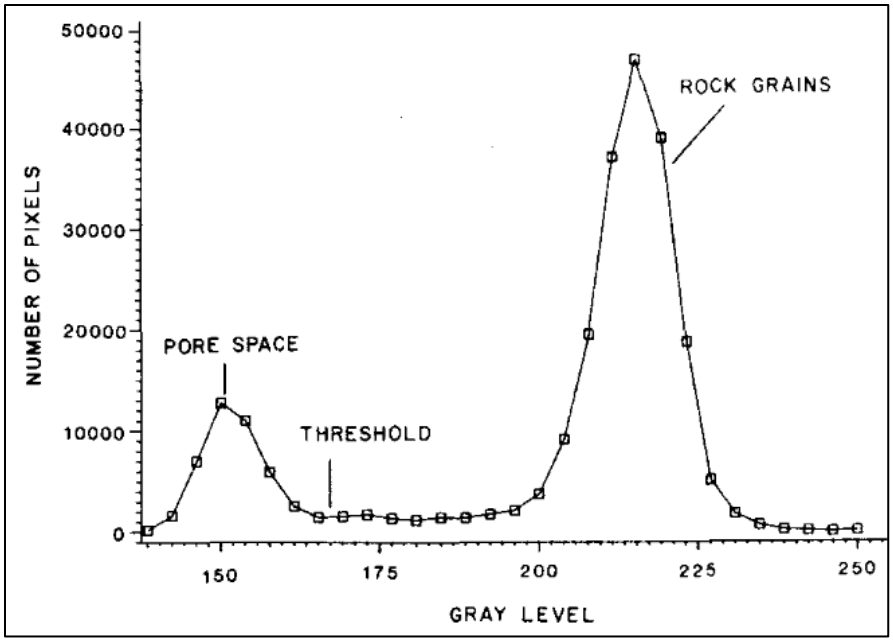

Figure 1.11: *Grey-scale histogram clearly showing the difference in grey level intensities between matrix and pore space (Ruzyla, 1986)*

Not shown in **Fig. 1.11**, but ever-present in digital imaging, is the impact of noise on the histogram. Noise may show up as a separate peak on the greyscale histogram, or as a widened base of the pore or rock peaks. Reduction of noise by digital filtering will be discussed later. Notice in **Fig. 1.11** the presence of a "threshold" grey value, defined somewhere between the peaks of pore space and rock grains. The binarization procedure involves setting this threshold greyscale value such that pore space and rock grains are entirely segmented. In reality, greyscale histograms are not as idealized as shown above and setting the threshold value is more difficult, especially in carbonates.

Ruzyla (1986) also compared cumulative pore-size distributions of several different rock types (carbonates, dolomites, and sandstones) and found that the distribution shapes differed both for different rock types, and different samples within a certain rock type. Pore shapes were quantified in each rock type according to a parameter called Form Factor, related to pore surface area and curvature. Pore shape can also be quantified by aspect ratio, or as a normalized shape factor where a perfect sphere

has a value of 1. In general, quantifying shapes of irregular objects, such as pores, is challenging. Multiple measures exist even for pore diameter, including Feret diameter - which measures the longest line segment that can fit within the irregular body – or equivalent diameter, defined as the diameter of the largest inscribed sphere that fits within the pore space. Equivalent diameter tends to underestimate the true pore diameter, but is more computationally efficient than Feret diameter, which requires up to 32 measurements per pore in 3-dimensional space. In the current work, Feret diameter is the chosen method due to its increased accuracy and ability to handle measuring irregular shapes. Modern post-process filters used in this work will be described in more detail in **Chapter II**.

1.2.3.a - Thresholding Algorithms and Binarization

Sezgin & Sankur (2004) provide a comprehensive review of 40 image thresholding methods for image processing. The full results of this study will not be described here; however each method was quantitatively evaluated for segmentation accuracy. In general, thresholding techniques can be categorized as global or local (Iassonov et al., 2009). Local methods depend on the spatial variation of greyscale values within the image, while global methods take into consideration the greyscale histogram of the entire image (or image stack, in 3D cases). This makes global methods more suitable for 3D volumes, such as those output from micro-CT scans. Because of the large number of algorithms considered in the Sezgin & Sankur study, and the different ways in which they work, comparing the results is non-trivial. As such, five different criteria were used to determine algorithm effectiveness. Ultimately, Otsu cluster thresholding (Otsu, 1979), a global histogram-based method, was found to be adequate in all cases considered. Despite this conclusion, the Sezgin & Sankur (2004) study did not specifically apply any algorithms to micro-CT scans of geologic media.

A study by Iassonov et al. (2009) compared Otsu thresholding against other methods specifically for the purpose of segmenting micro-CT scans of geologic media. Methods were scored based on porosity measurements and visual inspection of the results. They concluded that Otsu thresholding was superior to other methods for the purpose of consistently segmenting geological media

in an accurate manner. They also concluded that pre-processing steps were essential to accurate segmentation. In addition to the aforementioned study, the Otsu method has been widely used in the literature (Ji et al., 2012; Gharbi & Blunt, 2012; Andrä et al., 2013) and is the method used in this study. The Otsu method is described briefly in the following paragraph.

In Otsu's method, the greyscale histogram is divided into two regions, black and white, separated by a threshold (similar to the histogram shown in **Fig. 1.11**). The threshold is determined by minimizing the variance between greyscale values of the voxels above and below the evaluated threshold. The greyscale threshold is iteratively searched along the histogram until a value is reached where the aforementioned variance reaches a minimum value. A limitation of Otsu's method is that it tends to underestimate the porosity of carbonates with dual porosity, such as Indiana Limestone (Ji et al., 2012). Dual porosity is defined as a rock having two distinct sets of pore sizes, otherwise categorized as a macro and micro porosity. Microporosity is below the resolution of micro-CT imaging, but is still effective in promoting fluid flow so it contributes to the laboratory-measured porosity. To overcome this limitation, Ji et al. (2012) modified the Otsu (1979) technique by segmenting the greyscale histogram into three separate regions: solid, microporous, and macroporous. Although the theoretical basis for the Ji et al. (2012) method is sound, and Indiana Limestone does exhibit microporosity, a separate study (Freire-Gormaly et al., 2015) found that the difference between porosity derived from Otsu and Ji et al. methods in Indiana Limestone was negligible (13±1% and 14±5 % porosity for each method, respectively). Additionally, Otsu thresholding porosity values were found to agree well with laboratory results in the current work. Thus, the original Otsu procedure is used henceforth whenever "thresholding" is mentioned in the subsequent sections of this work.

1.2.3.b – Post-Binarization Procedures & Morphological Operations

Binarization procedures are not perfect, and many artifacts may still remain even after correct segmentation. These artifacts are mostly seen in the form of small pore specks in the matrix space, or holes in the pore space. An example of each from this study is shown in **Chapter II**, specifically **Figs.**

2.7 and **2.9.** These artifacts, only a few pixels wide, are due to noise or incomplete segmentation and are unphysical. If left untreated, these artifacts will eventually be labeled as small pores (in the case of specks), or cause problems with pore identification and connectivity measurements (in the case of holes). For example, the presence of small specks will artificially inflate the pore count, significantly reduce the average pore diameter, and affect numerous other measurements that depend on pore size. Thus, it is important to remove these artifacts and to recreate the pore and matrix space as accurately as possible to ensure correct labeling of individual pores in subsequent steps. Common ways of dealing with these types of artifacts in the image processing literature are called morphological operations (Haralick et al., 1987). Specifically, erosion and dilation are the most important of these operations. Erosion refers to the reduction of the perimeter of each pore element by a desired pixel amount. In this work, 1 pixel is used in all cases. Dilation refers to the opposite of erosion, whereby one pixel is added to the edges of each binarized pore section. Erosion and dilation are most always used together. The process of erosion followed by dilation is called an "opening" procedure. While at first glance an opening procedure (whereby 1 pixel is subtracted then added to all pore space edges) may seem a fruitless operation, in fact the output of the operation is different from the input. The purpose of the operation is to eliminate small, unphysical noise of a specific size (in this case 1 pixel). The advantage of this morphological operation is that specks and holes are eliminated while pore shape is maintained. This is best explained by visual example, as seen in this work in the figures mentioned above. Another example of the opening procedure, unrelated to this work, is shown below in **Fig. 1.12**

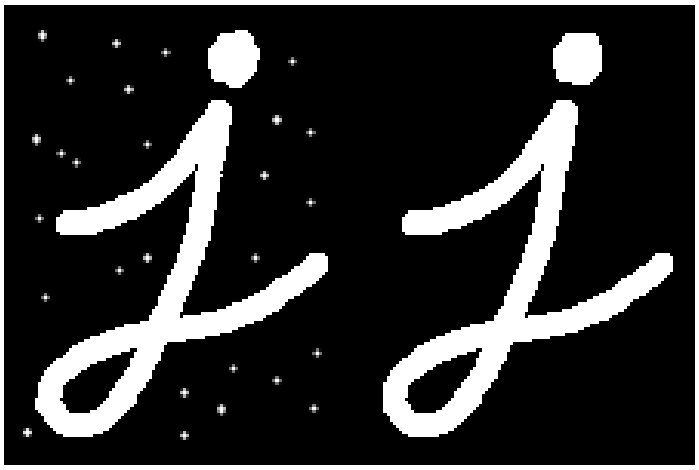

Figure 1.12: *Input image (left) prior to a morphological opening operation. Output image (right) maintains the figure of interest's shape while removing speckle noise. Holes within the figure would also be removed from the image by this procedure. (OpenCV-Python Documentation, 2014)*

1.2.3.c – Pore Labeling and Measurements

The final image processing step before pore measurements can be made is identification of the actual pores. Like binarization, this process is non-trivial and heavily dependent on the algorithms used and the quality of segmentation and filtering performed in the previous steps. In this study, the input to the labeling process (which involves a series of algorithms) is a binary image and the output is a "labeled image" – an image file that has individual pores identified and separated from each other. As always, this process is complicated further by consideration of pore boundaries in 3D. More information about the specific process used in this study can be found in **Chapter II.**

1.3 – Problem Statement

While pore-size distributions have been investigated as a way to categorize rocks, recent digital computing advances allow accurate recreation of the rock pore network. This reconstruction permits computation of pore sizes and many other measures, assuming correct pore segmentation can be attained.

This work investigates how the pore-size distribution of a given carbonate rock changes the values of optimum acidizing parameters ($PV_{bt,opt}$ and $v_{i,opt}$).

1.4 – Research Objectives

The purpose of this study is to characterize pore-size distributions from carbonate rocks and to relate them to optimum wormholing conditions values ($PV_{bt,opt}$ and $v_{i,opt}$) measured from linear corefloods. Trends from these relationships may give insights into more accurate models or help to reduce the need for lab experimental measurements of optimal conditions. Optimum acidizing parameters are also compared against pore measurements taken from image analysis.

CHAPTER II

METHODOLOGY

This section outlines the procedures undertaken in the present study to address the research objectives and problem statement posed above.

2.1 – Core Acidizing

Core acidizing was carried out at room temperature with 15 wt.% HCl on limestone cores (1-inch diameter by 6-inch length). The apparatus used to carry out acidizing procedures is shown in **Fig. 2.1.** The pressure drop across the core is monitored until breakthrough occurs. Pressure transducers output the measurements to a computer running LABVIEW software. A backpressure regulator is used to keep CO_2 generated from the calcite-HCl reaction in solution. A recent study found that allowing the CO_2 to come out of solution can slow down wormhole propagation, so regulation of backpressure is an important feature of the setup (Cheng et al., 2016). To determine optimum acidizing parameters, multiple acid corefloods must be completed at various injection rates for a given rock type. A sufficient number of corefloods are required until the optimal conditions are identified and an acid efficiency curve can be plotted. The curve is then fit with the Buijse & Glasbergen model to calculate optimum parameters ($PV_{bt,opt}$ and $v_{i,opt}$). More details on the acidizing apparatus, determination of breakthrough based on pressure drop, and curve-fitting procedures can be found in Izgec et al. (2010) and Etten et al. (2015).

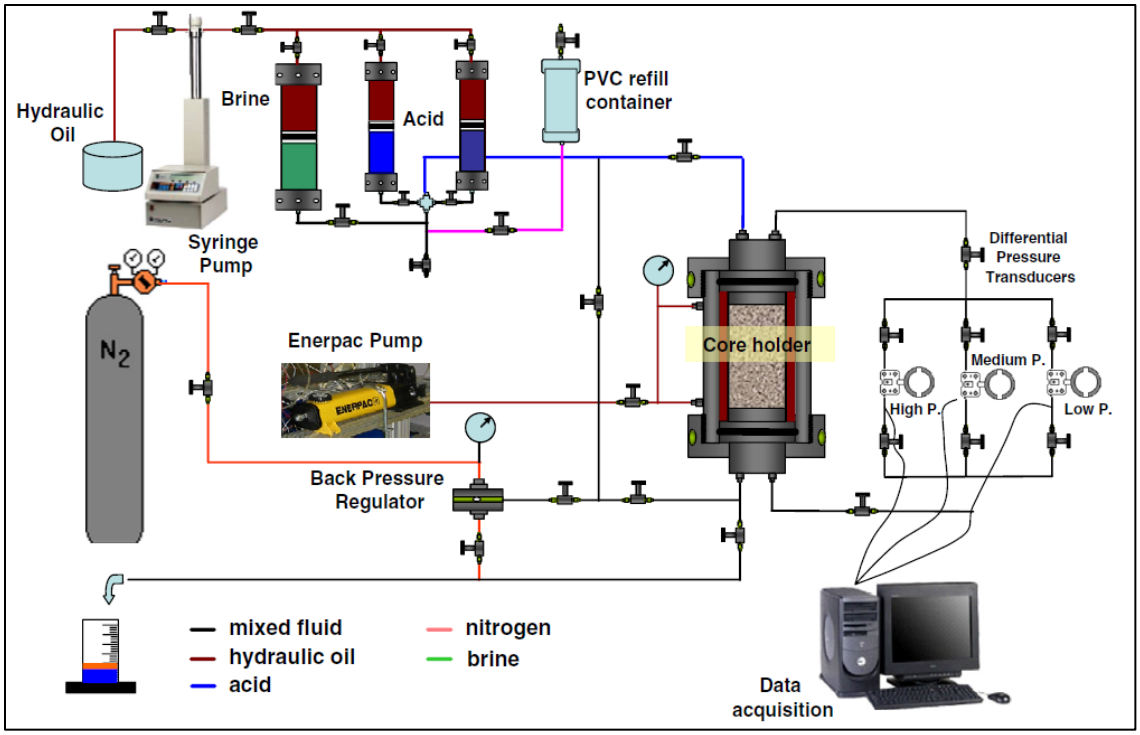

Figure 2.1: *Experimental setup for core acidizing experiments. Acid is injected from the top of the core and pressure is monitored to determine when breakthrough occurs. A backpressure regulator is used to keep CO_2 from acid reaction in solution. (Izgec et al., 2010).*

2.2 – Sample Preparation for Micro-CT Scanning

Samples for micro-CT scanning are significantly smaller than the 1 in. x 6 in. cores used in coreflooding. These cores are too large to be scanned with micro-CT, and medical CT (which allows for larger core-size samples) does not provide the resolution needed to perform pore-scale analysis of rock structure. Thus, two separate scales of rock samples are needed: cores for acidizing and samples for micro-CT analysis. To maintain consistency across these two scales, micro-CT samples were cut from the same block in the same orientation as the cores used for acid testing. This consideration was especially important with Travertine samples which showed high degrees of permeability anisotropy due to geological lamination. Cores and scanned samples were both cut parallel to the bedding to maintain consistency in the case of Travertine, since natural laminations in the rock prevented core breakthrough when acidized perpendicular to the bedding. **Table 2.1** lists the micro-CT samples studied

in this work, along with a naming convention that will henceforth be used in this study to refer to each sample. Each sample is named based on the type of limestone followed by a number representing its permeability. Samples within the same rock type are distinguished by their differing permeabilities. The permeabilities listed are measured from cores which are subsequently acidized to generate efficiency curves. In the case of Desert Pink, only one acid efficiency curve was created while two separate samples were scanned with micro-CT. Thus, the permeability (and optimum parameters) of the Desert Pink samples are the same.

Table 2.1: List of samples scanned using micro-CT in the current study.

Micro-CT Samples Scanned	Sample Reference Name
Desert Pink 1 (33md)	DP1-33
Desert Pink 2 (33md)	DP2-33
Indiana Limestone 1 (6md)	Indi-6
Indiana Limestone 2 (8md)	Indi-8
Indiana Limestone 3 (10 md)	Indi-10
Indiana Limestone 4 (239 md)	Indi-239
Travertine 1 (70md)	Trav-70
Travertine 2 (600md)	Trav-600

All samples for scanning were cut into $1cm^3$ cubes, except for the Indi-8 sample, which was approximately 0.5 cm^3. The size of the sample affects the scanning resolution, as described in the next section. Prior to scanning, the micro-CT samples were tested for their porosity. The method first involved measuring the volume and dry weight of each sample. The samples were then soaked in water overnight and the wet weight was measured. Porosity was calculated as the difference between wet and dry weight divided by the sample volume. Porosity of the micro-CT samples mostly matched well with

porosity of the acidized cores, but this was not always the case. **Table 2.2** compares the porosity of acidized cores with micro-CT sample porosity attained by the method described above. Note that the creation of acid efficiency curves requires multiple corefloods at different injection rates, so the listed core porosity is an average of all cores used to create the curve. The total number of cores used to create each curve is also listed.

Table 2.2: Comparison of porosity measured for cores and micro-CT samples for each rock type.

Rock Sample	Average Core Porosity (%)	Micro-CT Sample Porosity (%)
DP1-33	25 (9 samples)	30
DP2-33	25 (9 samples)	38
Indi-6	15 (11 samples)	19
Indi-8	15 (6 samples)	15
Indi-10	11 (6 samples)	13
Indi-239	16 (6 samples)	23
Trav-70	7 (4 samples)	17
Trav-600	9 (4 samples)	8

Table 2.2 shows that the DP2-33, Indi-239, and Trav-70 samples showed significant differences in porosity between core and micro-CT samples. For the most part, this is attributed to the effect of pore-structure heterogeneity which can be especially prevalent in high-permeability rocks like Travertine and Indi-239. Discrepancies between core porosity and micro-CT porosity are investigated further in **Chapter IV**. The porosity measured from the micro-CT samples is used for all correlations and subsequent analyses, since binary micro-CT images must be compared to the porosity of the scanned sample.

2.3 – Micro-CT Scanning Parameters

Micro-CT scans of sample rocks were performed at the Texas A&M Department of Petroleum Engineering. The model of scanner is a Phoenix Nanotom, manufactured by General Electric. As mentioned, the sample size for each rock type was $1cm^3$, except for the Indi-8 which was significantly smaller. This allowed the Indi-8 sample to be scanned at a higher resolution, at the expense of sample volume. Scanning resolution ranged from 5-8 microns per voxel. Care was taken to ensure the aspect ratio of voxels for each sample equaled 1, indicating the same resolution in the *x*, *y*, and *z* directions. **Table 2.3** lists the resolution of each sample.

Table 2.3: Resolution of each sample from micro-CT scanner.

Rock Sample	Resolution (µm/voxel)
DP1-33	8
DP2-33	7.2
Indi-6	6.5
Indi-8	5
Indi-10	6.5
Indi-239	8
Trav-70	7.6
Trav-600	7.5

2.4 – Image Processing

Unlike the medical CT scanner at Texas A&M Department of Petroleum Engineering, the micro-CT scanner does not provide methods for analysis of raw images. Thus, all processing of images was performed with open-source software. Specifically, a modified version of the software ImageJ, called FIJI, was used for image analysis (Schindelin et al., 2012). ImageJ has seen extensive use in the

field of biology, for which it was initially developed to analyze microscopy images**.** While the fields of geology and petroleum engineering tend to use professional analysis software (especially Avizo, by FEI Systems), ImageJ and FIJI are used frequently for studies where such premium software is unavailable. FIJI contains all the features of standard ImageJ software, but is modified with many plugins to make it more useful for analysis of 3D image stacks, such as those output from micro-CT. As the software is open-source, the plugins used come from many different developers which are credited accordingly in this thesis as they are mentioned. The main caveat when using such software is that there is no oversight to ensure accuracy or complete functionality of the plugins. Despite this stipulation, ImageJ and FIJI are widely regarded as the best free software for image analysis, mostly due to the extensive community support and availability of a wide variety of plugins.

In an effort to control the effect of resolution differences, the total digital volume to be analyzed was normalized across each sample. While the actual micro-CT samples were each $1cm^3$ (except Indi-8, which was $0.5cm^3$), the variability of noise and other CT scanner parameters means that the entire sample volume cannot be used for image analysis. Notably, edge artifacts were prominent near the top and bottom of each sample. Computing power limitations also must be considered during any digital analysis procedure. **Fig. 2.2** shows the volume normalization procedure visually.

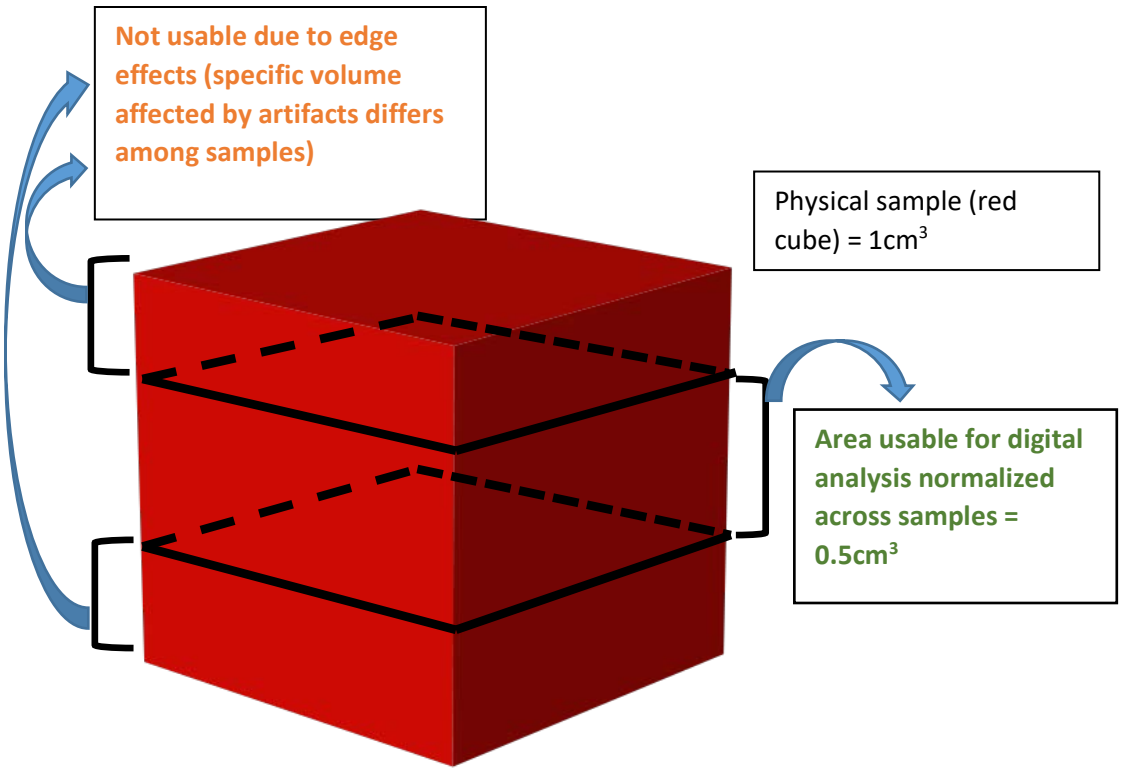

Figure 2.2: *Visualization of how digital sample volume is normalized to 0.5cm^3 to ensure comparability for pore count measurement. The Indi-8 sample is excluded from this normalization as only 0.133cm^3 of good-quality digital volume was available for analysis.*

The maximum volume that could be digitally analyzed, considering noise and artifacts across all samples, was 0.5 cm^3. Again, the exception is the Indi-8 sample. Since this sample was smaller than the others, only 0.133 cm^3 of the digital sample was usable for analysis. In theory, the only measurement this should affect is the number of resolved pores (pore count). All other measurements, including pore-size distributions, are normalized across the sample and frequencies are measured as a percent of overall pores. Even so, the digital volume of all other samples was normalized to 0.5 cm^3 to ensure consistency across pore measurements, including the pore count, which is an interesting value in itself and will be investigated in **Chapter IV**.

While every possible effort has been made to retain accuracy of results in this thesis, it must be noted that the software used was not written for complex segmentation of porous media and cannot

compete with the feature set available in premium software specifically tailored to analysis of geological media. At the end of this section is a visual representation of the image processing pipeline where the effects of filtering on images and greyscale histograms are shown.

2.4.1 – Filtering of Raw Data

Raw images from micro-CT vary in quality, but must always be post-processed before further analysis. In this study, the post-processing steps were normalized between all samples. Specific pre-binarization processes used were windows & level adjustment and a median blur 3D filter. These procedures are outlined below in more detail.

2.4.1.a – Window & Levels Adjustment

This is the first adjustment made to the raw micro-CT output images and is a standard feature of ImageJ. In **Figs. 2.3** and **2.4,** an example is shown of pre and post-processed images from this study. This adjustment allows the user to decide which greyscale intensities to include or discard in the image. Image contrast is affected by this selection. The adjustment is not necessarily an objective process, but generally, the "Auto" feature in ImageJ does an excellent job of selecting optimal window and level values. By experimenting with the sliders present in the software, and with the aid of the greyscale histogram visualization, the user selects values that optimally enhance pore-matrix contrast while reducing unwanted artifacts and noise.

2.4.1.b – Median Blur 3D Filter

This filter is applied to a greyscale image. It works by replacing a pixel's greyscale value with the median of intensity values of neighbor pixels. The neighborhood radius is defined by the user, and is kept constant at 2 pixels throughout this study. This filter helps reduce pore surface roughness while maintaining the pore volume and also eliminates speckle noise (intensity outliers). It is important to remove this type of noise because in subsequent steps, these speckles may incorrectly be labeled as

small pores. The 3D nature of this filter means that it can be applied to an entire stack of images. This is also a filter that comes standard with FIJI.

2.4.2 – Binarization Process

The thresholding algorithm used in this study for binarization is the one developed by Otsu (1979), which is a global, histogram-based procedure. Application of the Otsu method was performed through the built-in "Thresholding" option in FIJI. The binarization process is different from some of the aforementioned filters as it is more subjective, or a "semi-automatic" process. The Otsu algorithm chooses a threshold it defines as optimum, but the user can adjust sliders to add or remove areas of the screen that may not be correctly selected. FIJI dynamically overlays areas of threshold selection onto the greyscale image, so the user is easily able to adjust sliders as necessary with the objective being to fully include the pore space of the image while disregarding matrix space. In some cases, it is not entirely possible to include all pore space without including some matrix space. A common artifact present in Otsu thresholding are "speckles" or "holes", which are small-pixel areas incorrectly segmented in the matrix or pore space, respectively.

Notice that even after thresholding there are a number of areas where noise is still present (**Figs. 2.6** and **2.7**). If left this way, this noise would eventually be categorized as small, unconnected pores. A large number of these pores would significantly alter the mean pore diameter values and other measurements. Noise is present in both the matrix area, as single pixel pores, and in the pore area, as places where holes exist that are unphysical. To remove these small inconsistencies, mathematical morphology procedures are used, as described in **Chapter I**. Specifically, an "opening" procedure is used to remove the artifacts, which consists of an erosion followed by dilation procedure. The width of opening used is a conservative 1 pixel, as a balance must be struck between removing unwanted artifacts and avoiding the removal of legitimate small pores and holes. **Figs. 2.8** and **2.10** show the result after application of morphological procedures to the binarized images.

2.4.3 – Pore Identification, Labeling and Measurements

Pore labeling is performed by the 3D Objects Counter plugin in FIJI (Bolte & Cordelieres, 2006). The input to the plugin is a stack of binarized images and the output is the same binarized stack, but with individual pores labeled. Labeling of pores includes consideration of 3D connectivity of the pore network which is present in the binary image stack. As previously discussed, this process is non-trivial and one of the more complex areas of computer science research. The 3D Objects plugin does not allow the user to alter the labeled pore network, and there are certainly limitations to the algorithms used compared to the more advanced features present in premium software.

As mentioned, the user has no control over how the objects are labeled and how connectivity is defined. The only other inputs (in addition to the binary stack) is a selection of measurements to be performed on each labeled object. There are many selectable measurements, and the ones specifically used in this study are presented in **Chapter III.**

2.4.4 – Image Processing Pipeline

The full image processing pipeline is shown in this section for Trav-600 (**Figs. 2.3 – 2.8**). This visualization is presented as a summary of the above explanations. The steps shown in this section were completed for each of the 8 rock samples analyzed. Also note that while only a single image is shown in the following section, for each sample the process is performed on the entire image stack (i.e. in 3D).

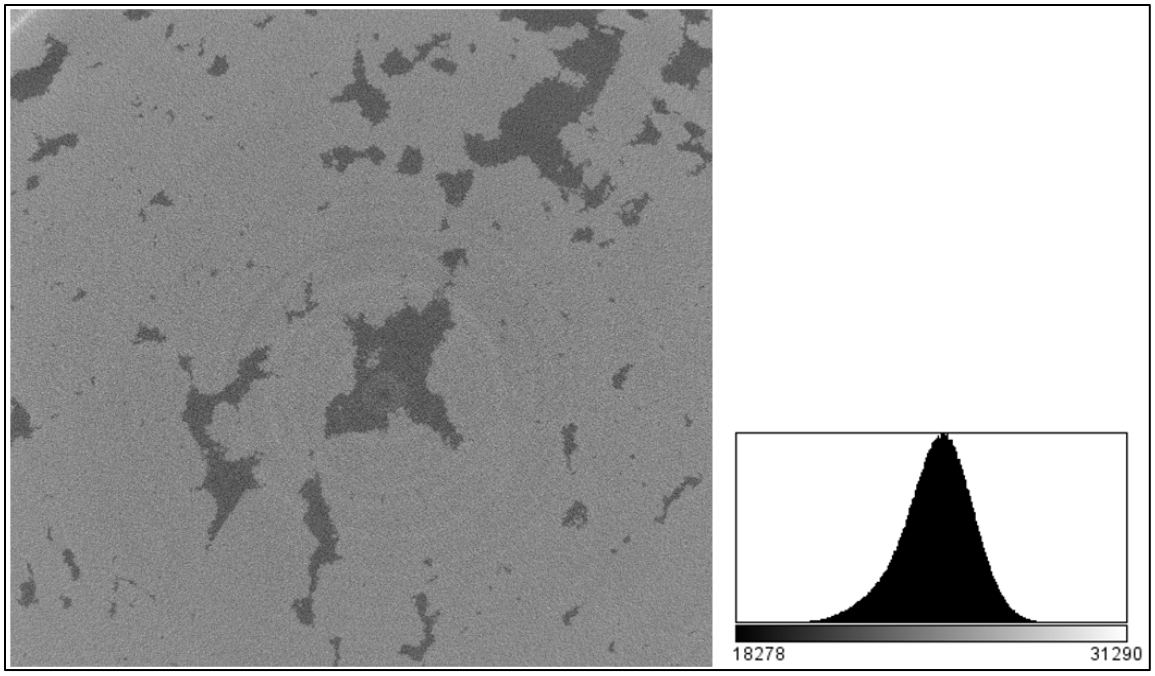

Figure 2.3: *Raw image output (after cropping) from micro-CT and associated intensity histogram. No post-processing has been applied. Note since the image is 16-bit greyscale, there are more than 255 grey values (as would be present in an 8-bit image).*

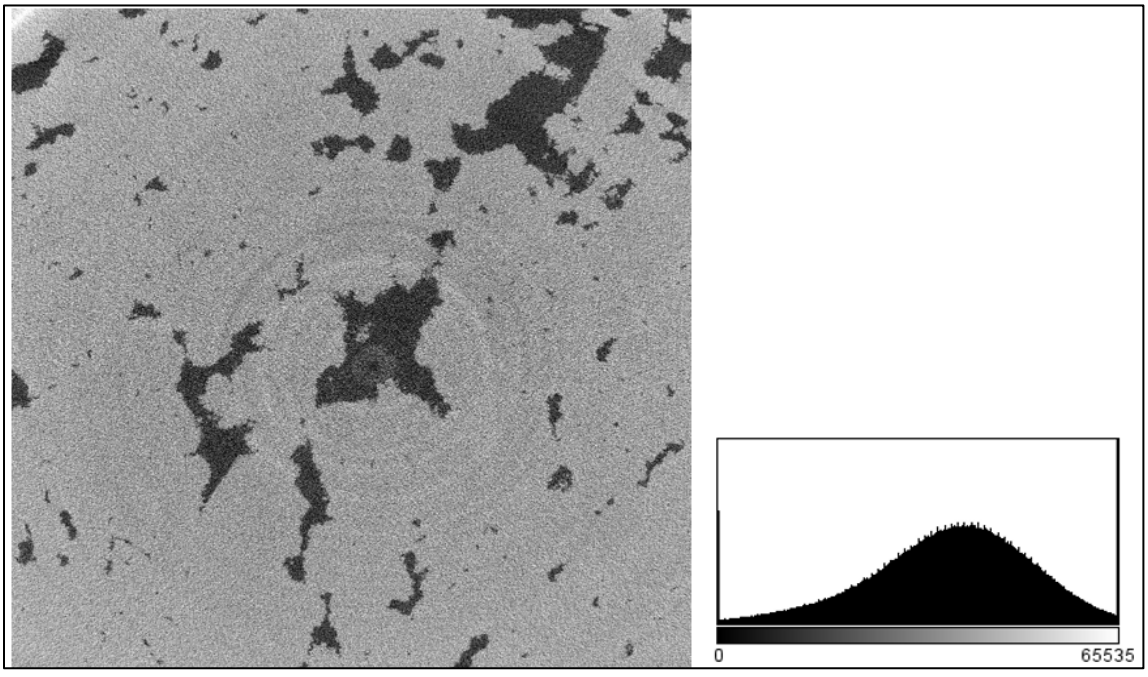

Figure 2.4: *Window & Level selection altered to enhance contrast and remove unwanted grey values from the image. The histogram height is reduced (and width increased) due to the Window/Level selection reassignment. Note on both ends of the histogram there are pure black (0 intensity value) and pure white (65535 intensity value for 16-bit images). Note the introduction of speckle noise.*

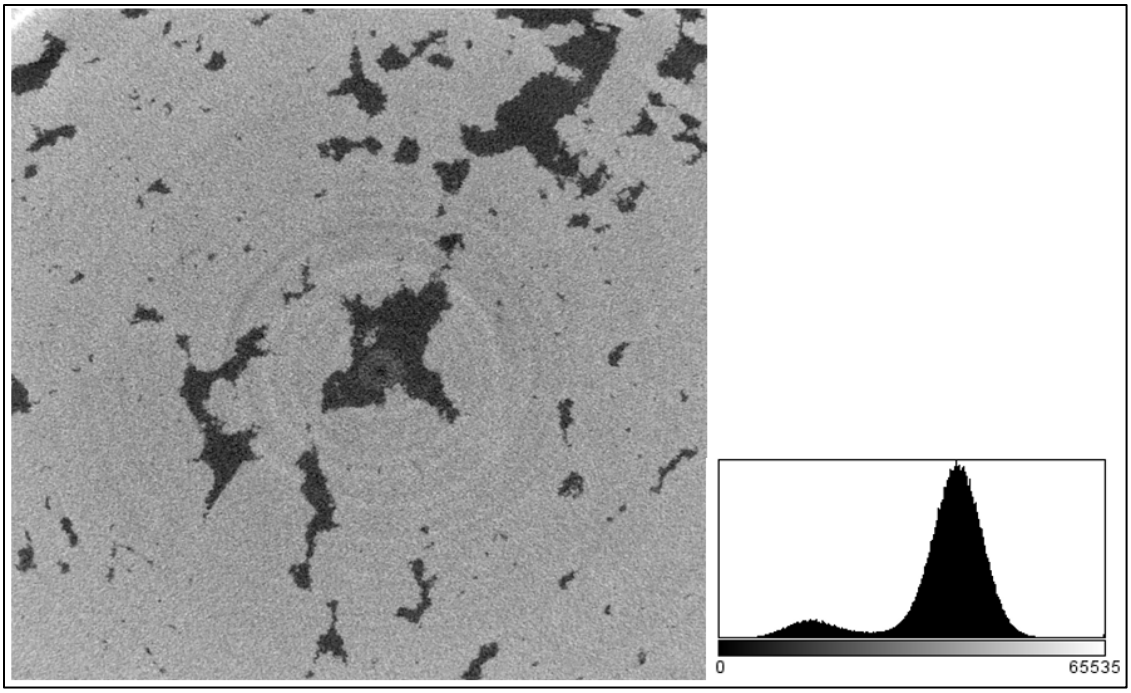

Figure 2.5: *Median filter applied to reduce speckle noise. Note the change in histogram shape, indicating pore (left peak) and matrix space (right peak)*

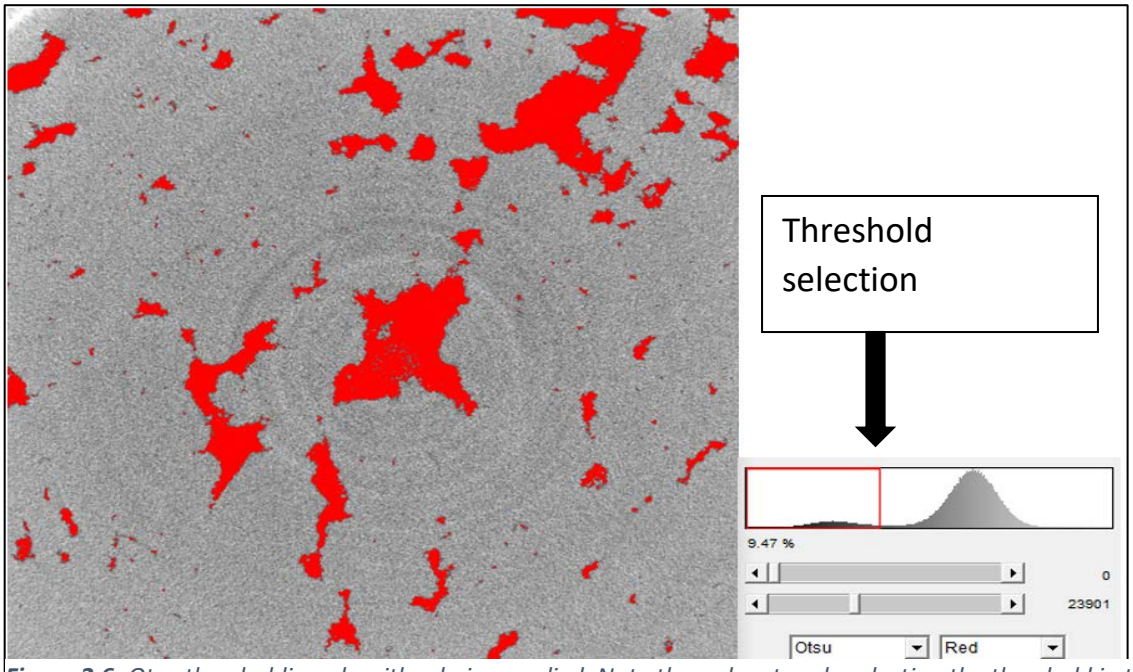

Figure 2.6: *Otsu thresholding algorithm being applied. Note the red rectangle selecting the threshold in the valley between the two peaks (recall* ***Fig. 1.11****).*

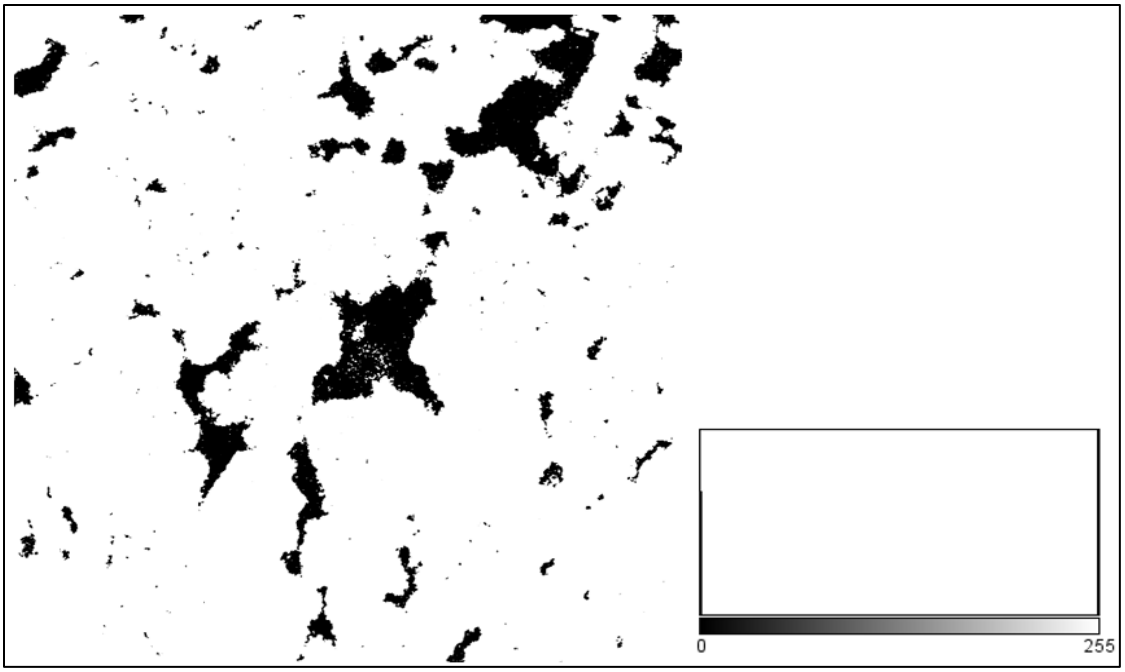

Figure 2.7: *Binary image after application of Otsu thresholding at above value. A few things to note: 1. Noise within the pore-space (holes). 2: Histogram only shows two intensities at extremes of the axis. 3. During binarization, the image is converted to 8-bit greyscale. This reduces the intensity scale to 0-255.*

Figure 2.8: *Opening procedure (erode followed by dilate) closes holes while maintaining the pore morphology. In a noisier image, speckles in the matrix space would also be reduced. Especially note the large middle pore.*

To better illustrate the abilities of the opening procedure, a binary image of Indi-10 is shown pre-and post-opening (**Figs. 2.9** and **2.10**, respectively).

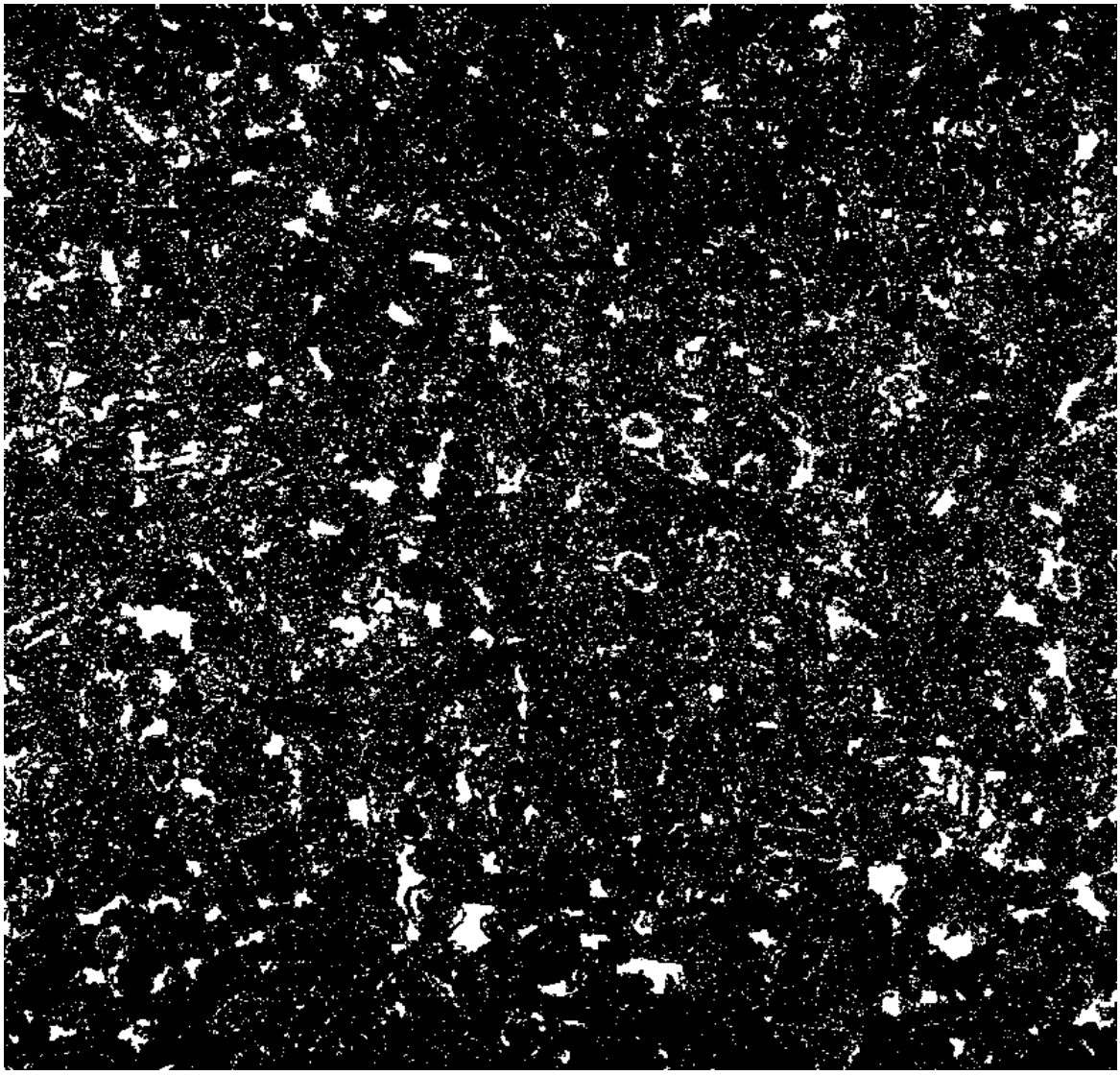

Figure 2.9: *Indi-10 binary image (pores in white) after Otsu thresholding.*

Trav-600 was a simpler image to segment as the pores are quite large and image quality good. Indi-10 is shown above (**Fig 2.9**) with all filtering completed up to the erosion + dilation (opening) procedure. Despite the median 3D speckle-reduction filter, there is prominent noise in the matrix area after Otsu thresholding. Below is the same image after the opening step.

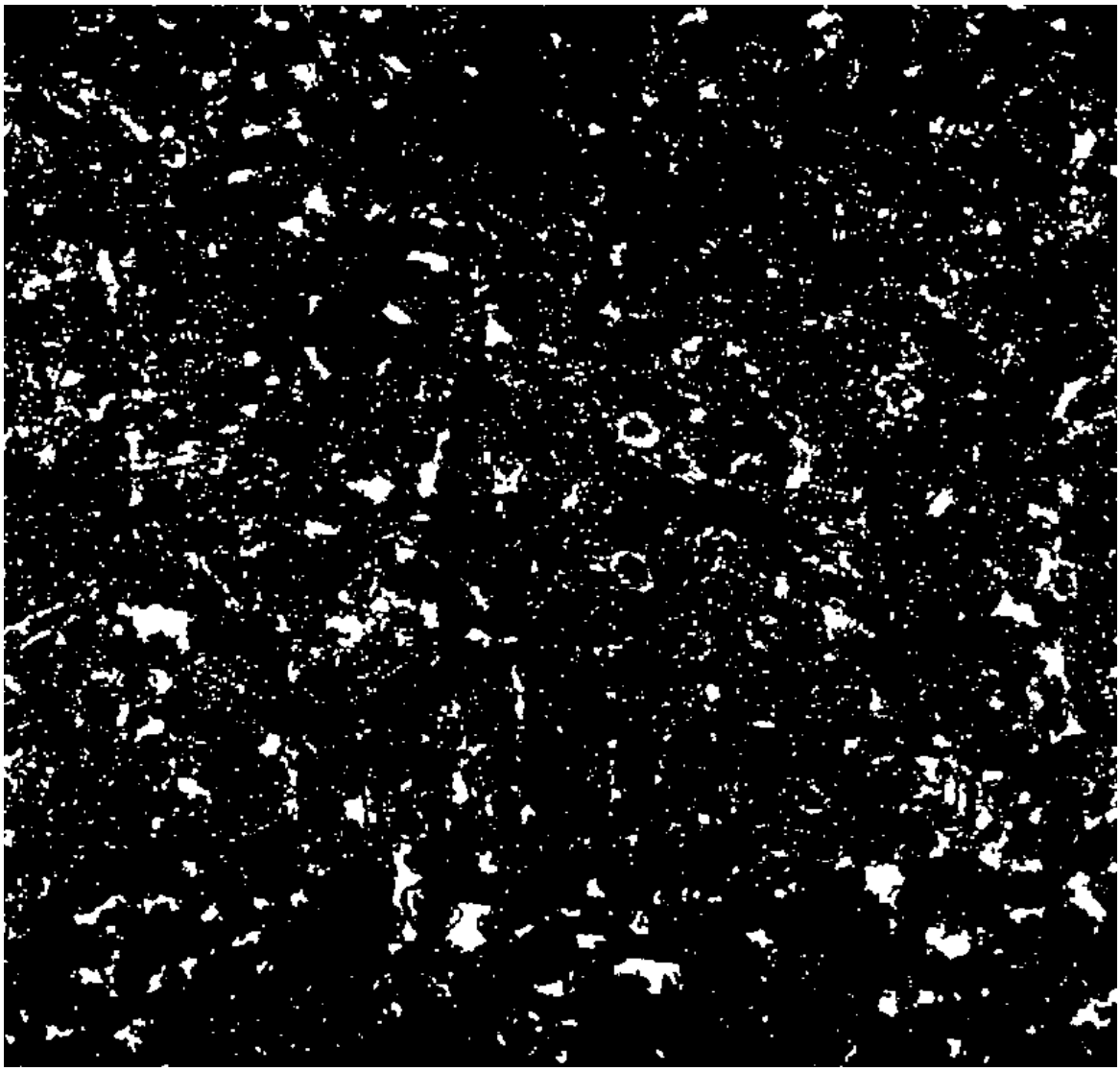

Figure 2.10: *Indi-10 binary image after morphological opening (pores in white).*

Note the reduction in matrix-space speckles while maintaining the shape of the pores. A balance must be struck between removing noise while still keeping legitimate small pores. Thus, the opening procedure is set to only remove holes or speckles that are 1 pixel in size. Computation of mean pore diameter of Indi-10 in **Fig. 2.9** vs. **Fig. 2.10** produces vastly different results: 26 μm vs. 48 μm.

2.5 – Pore-Size Distribution Construction

After measurements have been performed on individual pores by the object counter software, the results of pore diameter are organized into a frequency distribution. Because the resolution is different for each sample (due to optimization of micro-CT scanner parameters during scanning), the minimum pore size able to be resolved for each sample is slightly different. This is somewhat noticeable when comparing distributions, but the variation is very small.

Due to the large number of pores present in each sample, frequency distributions are created by sorting pores into distinct bins along the *x*-axis that encompass a range of pore sizes. There are a number of methods for determining an appropriate bin width, and each method can give different results. In general, a bin width must be selected that presents an adequate visualization of the data without presenting too much, or too little detail. For more information on choice of histogram bin width, the reader is referred to Wand (1997). Note that the samples have differing maximum pore diameters, so the total distribution length along the *x*-axis is not the same for each distribution. In this work, care is taken to ensure bin widths are similar across all sample pore-size distributions to ensure comparability.

The resolution difference is negated on the *y*-axis by normalizing each distribution. Instead of showing the exact number of pores falling within each bin, the percent of the total number of pores is shown. By performing this calculation, the distribution is normalized and made comparable to other samples of differing resolutions.

The standard way of displaying a frequency plot is either a bar-graph histogram or a scatter plot with markings at the determined frequency for each bin. In this work, the scatter plot is used with smoothed lines connecting the points to better show the shape of the plot (see **Fig. 3.2** for an example from this study). This method allows for easier comparison of different samples. Frequency distributions are plotted in both semi-log and log-log axes. The semi-log plot shows the familiar bell-shaped curve, while the log-log plot is qualitatively helpful because it highlights the presence of very

large pores that have a low frequency of occurrence. In the semi-log plots, these pores often do not have sufficient frequency to be seen at all.

This thesis focuses on fitting the semi-log visualization with a lognormal distribution equation. The lognormal distribution equation used for fitting is

$$P(x) = \frac{1}{x\sqrt{2\pi\sigma^2}} \exp\left(-\frac{(\ln(x) - \mu)^2}{\sqrt{2\sigma^2}}\right) \quad \text{.....(2.1)}$$

Where x is the pore diameter and μ and σ are used as fitting parameters. MATLAB's distribution fitting application is used to automatically generate μ and σ values that optimize the fit of the lognormal distribution to the semi-log visualization of pore-size data. These two variables affect the shape of the lognormal distribution in different ways. The μ variable, often called the location parameter, is related to the mean, median, and mode of the distribution and thus the location of the peak value along the *x*-axis. The other fitting variable, σ, is sometimes called the shape parameter as it affects the height and sharpness of the distribution peak. This variable is related to the skewness and kurtosis of the distribution. The distribution variance is affected by both μ and σ values. By taking these two variables together and using them to fit the distribution, an optimal curve fit can be attained by altering the shape and peak location of the function to fit the pore-size distribution. Pore-size distributions and fitted values are shown in **Chapter III** of this work.

CHAPTER III

RESULTS

This section displays results gained from experimental work of this study, including optimum wormholing parameters from acid coreflooding and results from image analysis of the micro-CT scanned rock sample pore structures.

3.1 – Core Acidizing

Optimum parameters for each rock type are shown in **Table 3.1.** Determination of these parameters required at least 4 acidized core samples to complete the acid efficiency curve. The data points were then fit with the Buijse & Glasbergen (2005) model to determine optimum parameters.

Table 3.1: Optimum parameters for each rock type as determined by acidizing coreflood tests.

Rock Sample	Optimum Pore Volumes To Breakthrough ($PV_{bt,opt}$)	Optimum Interstitial Flux ($v_{i,opt}$, cm/min)
DP1-33	0.64	3.25
DP2-33	0.64	3.25
Indi-6	0.34	1.60
Indi-8	0.34	1.56
Indi-10	0.58	2.92
Indi-239	0.75	2.25
Trav-70	0.49	24.5
Trav-600	0.70	20.0

Note that $PV_{bt,opt}$ increases with permeability across both Indiana Limestone and Travertine rock samples. The values of $v_{i,opt}$ do not show a clear trend, as the value decreases at large permeabilities in both Travertine and Indiana Limestone samples. Indiana Limestone (excluding Indi-8) and Desert

Pink optimum values were determined by Etten et al., (2015). Travertine and Indi-8 efficiency curves were created specifically for this study.

3.2 – Image Processing

Table 3.2 compares porosity derived from micro-CT images binarized using Otsu thresholding with porosity measured directly from the 1 cm^3 samples. The process of measuring laboratory-determined porosity of samples is discussed in **Chapter II**. Note that the listed micro-CT porosity results are those measured from the 1 cm^3 samples, and are not the same as those measured from acidized core samples. The latter comparison was discussed previously and is shown in **Table 2.2**.

Table 3.2: Comparison of porosity derived from lab experiments and image analysis.

Rock Sample	Micro-CT Sample Porosity (%)	Image Analysis Porosity (%)
DP1-33	30.0	28.0
DP2-33	37.6	36.8
Indi-6	19.0	13.2
Indi-8	15.0	13.6
Indi-10	12.6	12.0
Indi-239	22.7	21.3
Trav-70	17.4	16.3
Trav-600	8.3	8.0

From the above table, it is clear that the porosity measured from binary images thresholded with the Otsu algorithm match well with the sample porosity measured in lab. **Fig. 3.1** plots the values against each other for a visual representation of the porosity comparison.

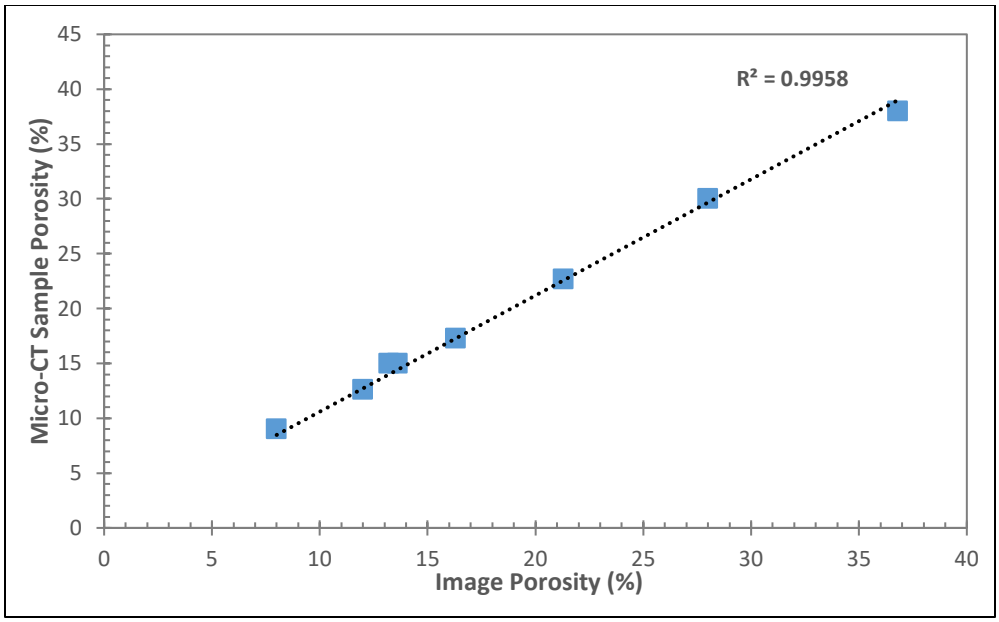

Figure 3.1: *Comparison of lab-derived porosity measurements of micro-CT samples versus image-derived porosity calculated from binary images after Otsu thresholding.*

A summary of measurements relating to pore size are shown in **Table 3.3**

Table 3.3: Measured parameters from image analysis of each rock type relating to pore size.

Rock Sample	Mean Pore Diameter (µm)	Median Pore Diameter (µm)	Mean Pore Volume (µm^3)	Median Pore Volume (µm^3)
DP1-33	72.1	44.4	521,911	10,997
DP2-33	97.3	39.8	1,171,980	8,885
Indi-6	17.4	13.0	66,763	1,373
Indi-8	16.5	10.0	65,398	3,747
Indi-10	47.8	34.7	66,267	4,939
Indi-239	62.8	40.2	391,674	7,269
Trav-70	62.4	40.4	488,854	8,014
Trav-600	116.2	54.4	3,945,680	19,502

When attempting to describe sample pore size with a single number (i.e. mean or median), it appears that the median number is the best figure to use. As previously discussed, noise inherent in the imaging and post-processing steps can drastically affect the mean values. For example, notice that while DP1-33 and DP2-33 are the same rock with equal permeability, the mean pore diameter is quite different between them. This difference lessens when observing the median pore diameter value. The same can be said about the pore volume measurements for Desert Pink samples. Some difference is still expected between the pore size values between these two samples because of the difference in porosity of DP1-33 and DP2-33 (30% vs. 38%, respectively). Using the median value reduces the effect of very large or small pores on the value of interest. Thus, for heterogeneous rocks with wide pore variance, the mean may be more appropriate. Ideally, both values should be attained along with the pore-size distribution to more accurately decide which value is suitable.

For Indiana Limestone, the pores trend towards increasing size as the permeability increases. The Indi-6 and Indi-8 samples are very close in pore diameter, permeability, porosity, and optimum acidizing parameters. Note that the pore diameter increases sharply from the Indi-8 to the Indi-10 samples. This corresponds with an increase in $PV_{bt,opt}$ values (from 0.34 to 0.58, respectively). The optimum flux, $v_{i,opt}$, also increases from the Indi-8 to Indi-10 sample (from 1.56 to 2.92 cm/min). These trends will be explored further in **Chapter IV**.

The Travertine samples show an increase in all measures of pore size as permeability increases from Trav-70 to Trav-600. This occurs despite the higher porosity of the Trav-70 sample (17%) compared to the Trav-600 sample (9%).

3.3 Pore-Size Distributions

In this section, pore-size distributions are first shown for each sample individually with semi-log and log-log axes. Next, samples of the same rock type are compared by overlaying the distributions onto one plot. Finally, the plots of rock types with similar optimum acidizing values are compared to determine how these parameters affect pore-size distribution shape.

3.3.1 – Pore-Size Distributions for Each Rock Type

In this section, pore-size distributions are presented for each sample. Plots are shown for each sample in both semi-log and log-log plotting styles. Semi-log plots emphasize the shape of the distribution along the area of most frequently-occurring pore diameter, while log-log plots encompass the entire distribution of pore sizes within the sample and show larger pores with a low-frequency of occurrence. The presence of such pores may not appear on semi-log axes, but they do affect measurements relating to mean pore diameter and pore volume gathered from the image analysis dataset. At the end of this section, after plots are presented, analysis of the results will be presented. Further in-depth discussion is reserved for **Section 3.3.2**, which compares pore-size distributions of different samples plotted on the same graph.

3.3.1.a – Desert Pink 1 (DP1-33)

Fig. 3.2 shows frequency plots on semi-log and log-log axes of the DP1-33 sample.

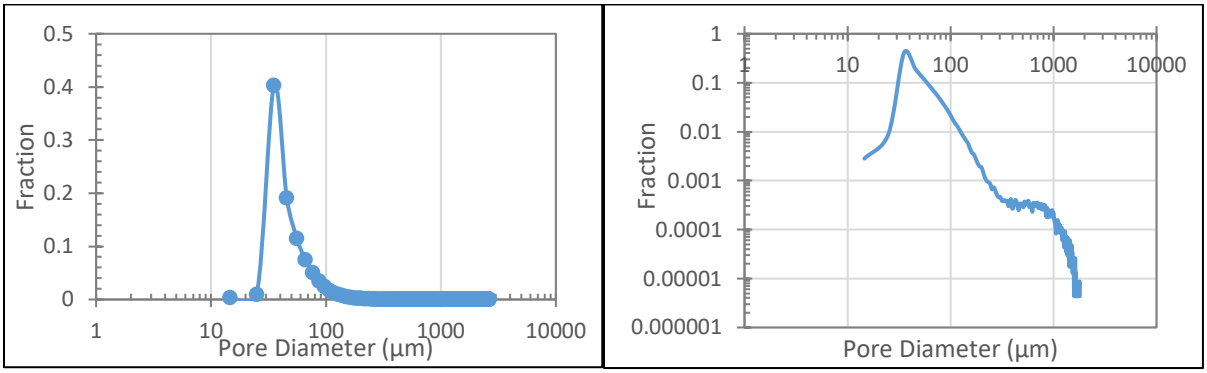

***Figure 3.2**: DP1-33 pore-size distribution on semi-log (left) and log-log (right) axes*

3.3.1.b – Desert Pink 2 (DP2-33)

Fig. 3.3 shows frequency plots on semi-log and log-log axes of the DP2-33 sample.

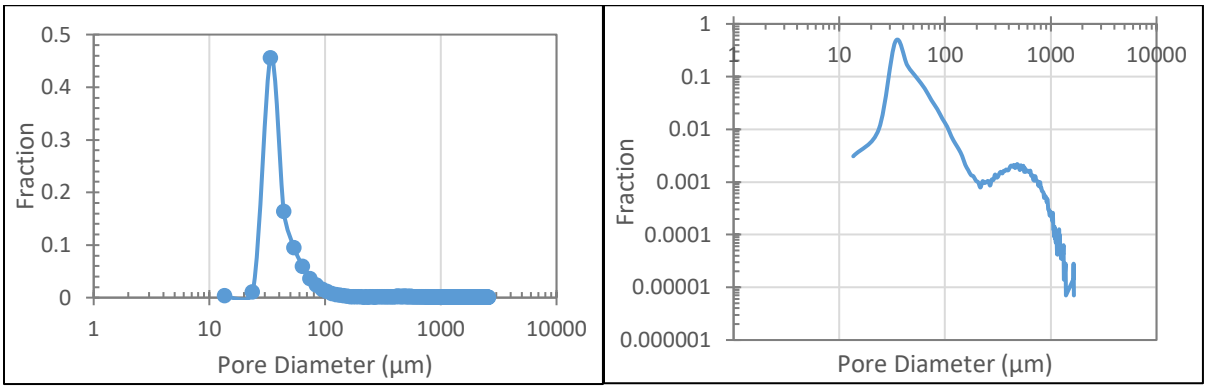

***Figure 3.3:** DP2-33 pore-size distribution on semi-log (left) and log-log (right) axes.*

3.3.1.c – Indiana Limestone 6md (Indi-6)

Fig. 3.4 shows frequency plots on semi-log and log-log axes of the Indi-6 sample.

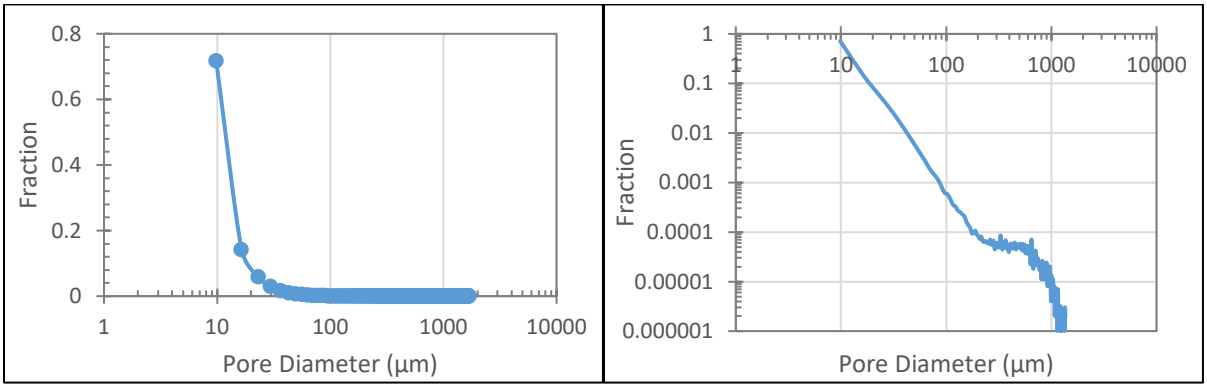

Figure 3.4: *Indi-6 pore-size distribution on semi-log (left) and log-log (right) axes.*

3.3.1.d – Indiana Limestone 8md (Indi-8)

Fig. 3.5 shows frequency plots on semi-log and log-log axes of the Indi-8 sample.

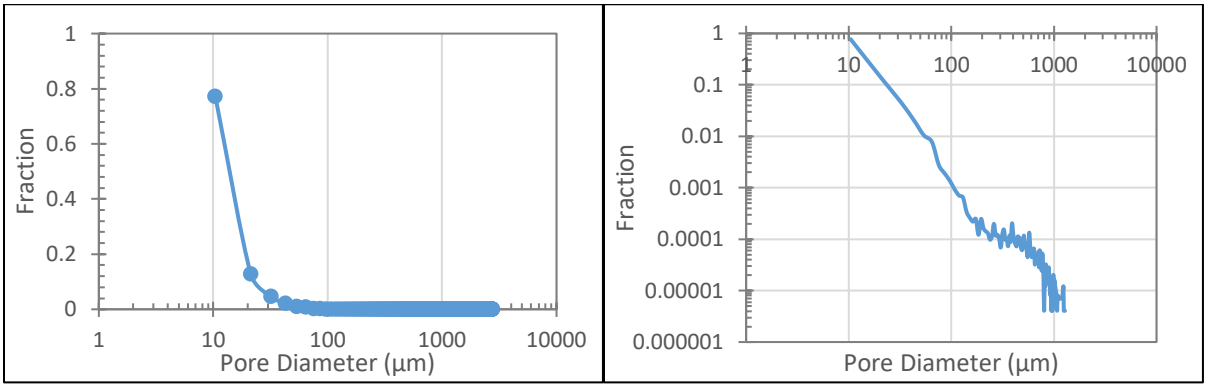

Figure 3.5: *Indi-8 pore-size distribution on semi-log (left) and log-log (right) axes.*

3.3.1.e - Indiana Limestone 10md (Indi-10)

Fig. 3.6 shows frequency plots on semi-log and log-log axes of the Indi-10 sample.

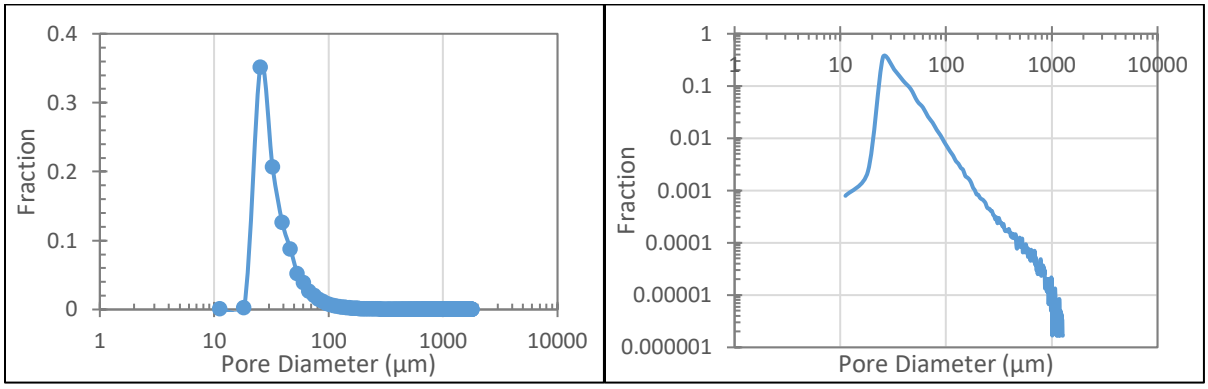

Figure 3.6: *Indi-10 pore-size distribution on semi-log (left) and log-log (right) axes.*

3.3.1.f – Indiana Limestone 239md (Indi-239)

Fig. 3.7 shows frequency plots on semi-log and log-log axes of the Indi-239 sample.

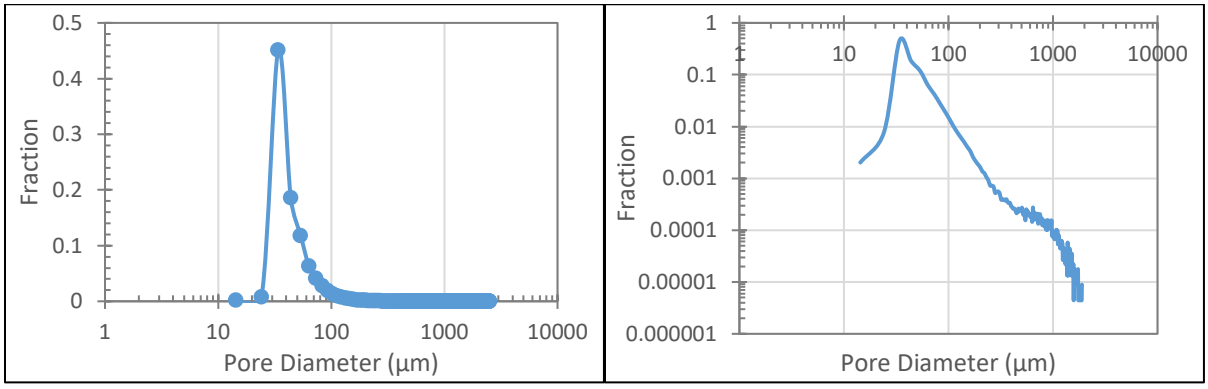

Figure 3.7: *Indi-239 pore-size distribution on semi-log (left) and log-log (right) axes.*

3.3.1.g - Travertine 70md (Trav-70)

Fig. 3.8 shows frequency plots on semi-log and log-log axes of the Trav-70 sample.

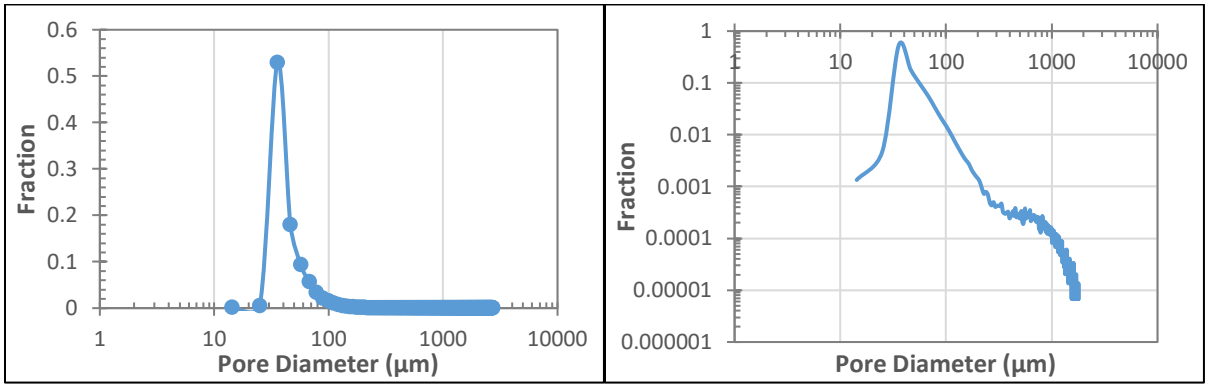

Figure 3.8: *Trav-70 pore-size distribution on semi-log (left) and log-log (right) axes.*

3.3.1.h - Travertine 600md (Trav-600)

Fig. 3.9 shows frequency plots on semi-log and log-log axes of the Trav-600 sample.

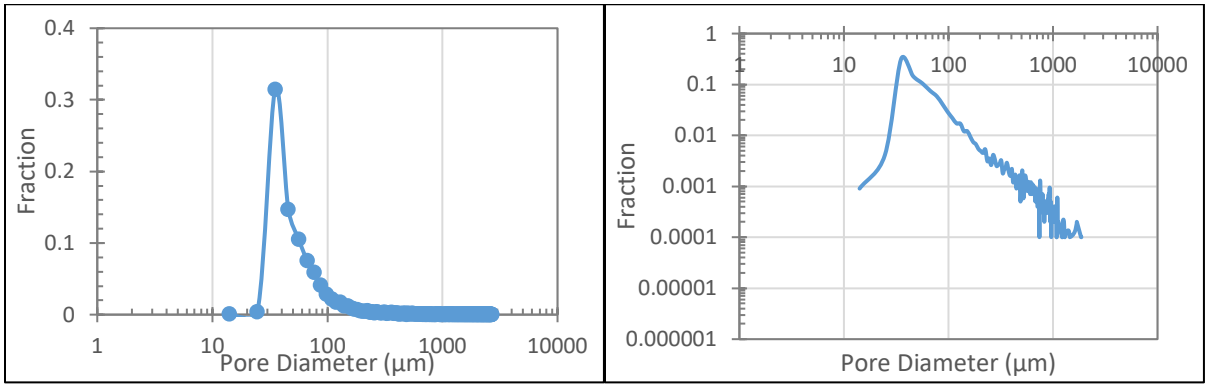

Figure 3.9: *Trav-600 pore-size distribution on semi-log (left) and log-log (right) axes.*

Figs. 3.2 – 3.9 show semi-log and log-log graphs of computed pore-size distributions for each rock. There are several things to note from these distribution results. Firstly, the distributions for Indi-6 and Indi-8 do not show the characteristic bell shape on semi-log axes. This is because the smallest-resolved pore size is also the size with the highest frequency, which is not the case for the other distributions. Secondly, in the log-log plots some samples show a distinct secondary plateau or peak,

especially DP2-33. This may indicate the presence of vugs within the sample, or the bimodal nature of the pore structure. The value of the log-log plots is that they can show these large pore diameters that are present within the rock but not seen on the semi-log plot due to the low frequency of occurrence.

3.3.2 – Pore-Size Distribution Comparisons

In this section, semi-log and log-log distributions are superimposed onto one plot for the same rock type. The *x*-axis maximum value has been reduced from 10,000 in the above section to 1,000 to allow for better comparison of the distribution shape. In the semi-log plot, large pores with small frequency are difficult or impossible to distinguish. The log-log plots are better for visualizing these large pores, which will have an impact on the image analysis measurements such as those listed in **Table 3.3.** As in the previous section, first the comparison plots will be displayed and a discussion of results will follow for each rock type.

In the second part of this section, pore-size distribution plots of different rock types with similar optimum values are compared to identify qualitative trends in these distributions.

3.3.2.a – Desert Pink Limestone Comparison

Fig. 3.10 shows a comparison of pore-size distributions for both Desert Pink samples (DP1-33 and DP2-33) plotted on semi-log axes.

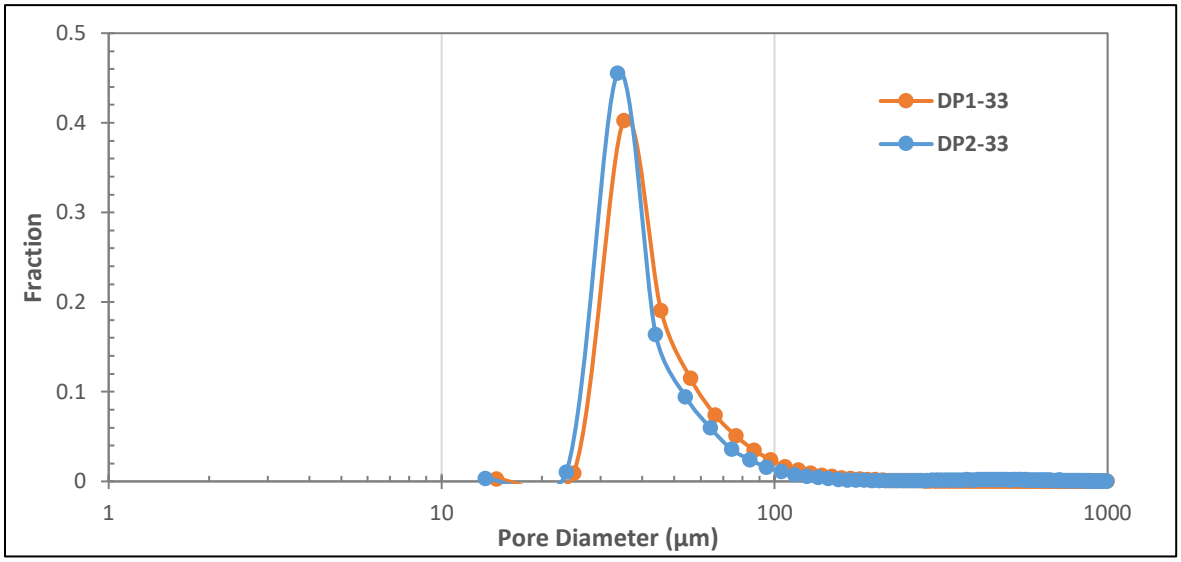

Figure 3.10: Desert Pink pore-size distribution comparison on semi-log axes

Fig. 3.11 shows a comparison of pore-size distributions for both Desert Pink samples plotted on log-log axes.

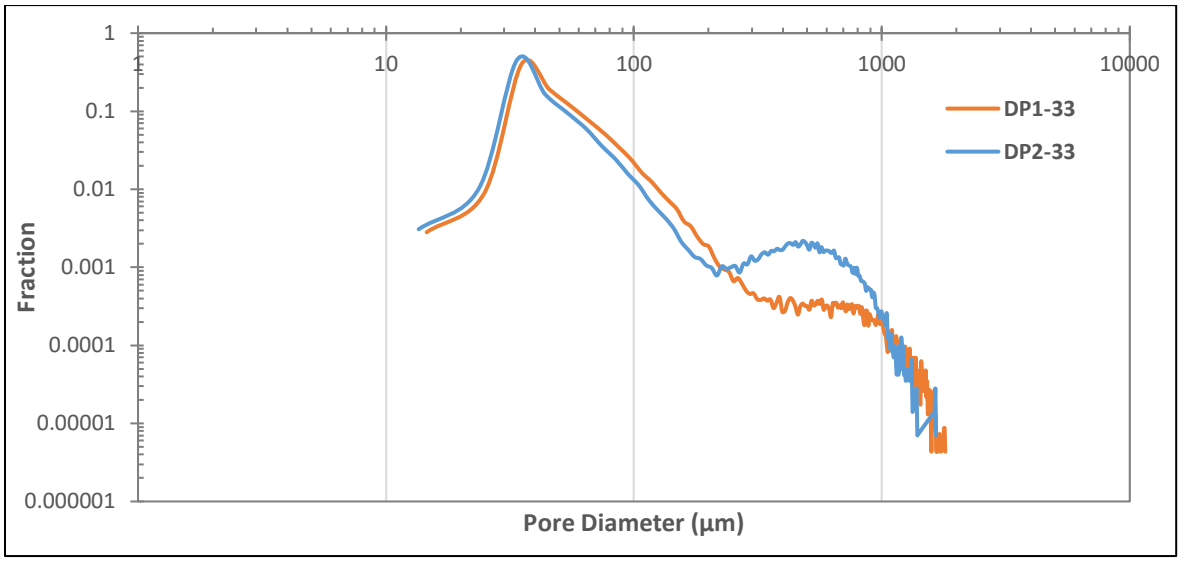

Figure 3.11: Desert Pink pore-size distribution comparison on log-log axes

Fig. 3.10 shows that for the largest frequency of pores (from 10-100 μm), the distributions are very similar. This is to be expected as the two rocks are of the same type, albeit with different porosity. **Fig. 3.11** shows that the DP2-33 sample has a section of larger pores in the 200-1000 μm range compared with DP1-33. This secondary peak is explained by the higher porosity of DP2-33 (38%) compared with DP1-33 (30%). Since the distributions are very similar in **Fig. 3.10**, the higher porosity is most likely due to contribution of these larger pores in the DP2-33 sample. The secondary peak also explains the large discrepancy in mean pore size and volume for DP2-33, shown in **Table 3.3.** Note that while the peak is more pronounced for DP2-33, the DP1-33 sample also shows a distinct plateau around the same pore diameter range.

3.3.2.b – Indiana Limestone Comparisons

Since four separate Indiana Limestone samples are analyzed in this work, a number of comparison plots will be presented. For convenience, **Table 3.4** below reiterates the physical properties and optimum parameters of the four samples. Since the pore-size distributions are measured from digital binary images, the porosity listed is that from the digital analysis. As shown in **Fig. 3.1,** the difference between lab-measured and digital porosity is negligible.

Table 3.4: Indiana Limestone physical properties and optimum acidizing parameters.

Rock Sample	Image Porosity (%)	$PV_{bt,opt}$	$v_{i,opt}$ (cm/min)
Indi-6	13.2	0.34	1.60
Indi-8	13.6	0.34	1.56
Indi-10	12.0	0.58	2.92
Indi-239	21.3	0.75	2.25

3.3.2.c - Indiana Limestone 6md vs. 8md

The Indi-6 and Indi-8 samples are similar in all regards: permeability, porosity, $PV_{bt,opt}$, $v_{i,opt}$, mean pore diameter and mean pore volume. Thus, it should be expected that the pore structure – and thus pore-size distributions – are similar. **Fig 3.12** shows a comparison of pore-size distributions for Indi-6 and Indi-8 samples on semi-log axes.

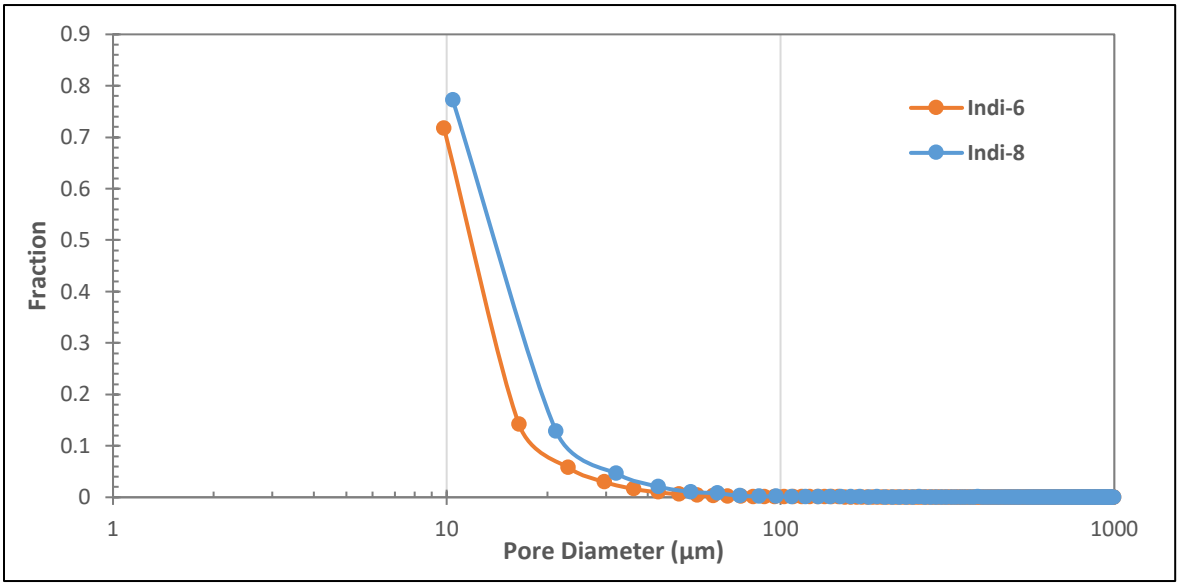

Figure 3.12: *Indi-6 and Indi-8 pore-size distribution comparison on semi-log axes.*

Fig. 3.13 shows a comparison of pore-size distributions for Indi-6 and Indi-8 samples on log-log axes.

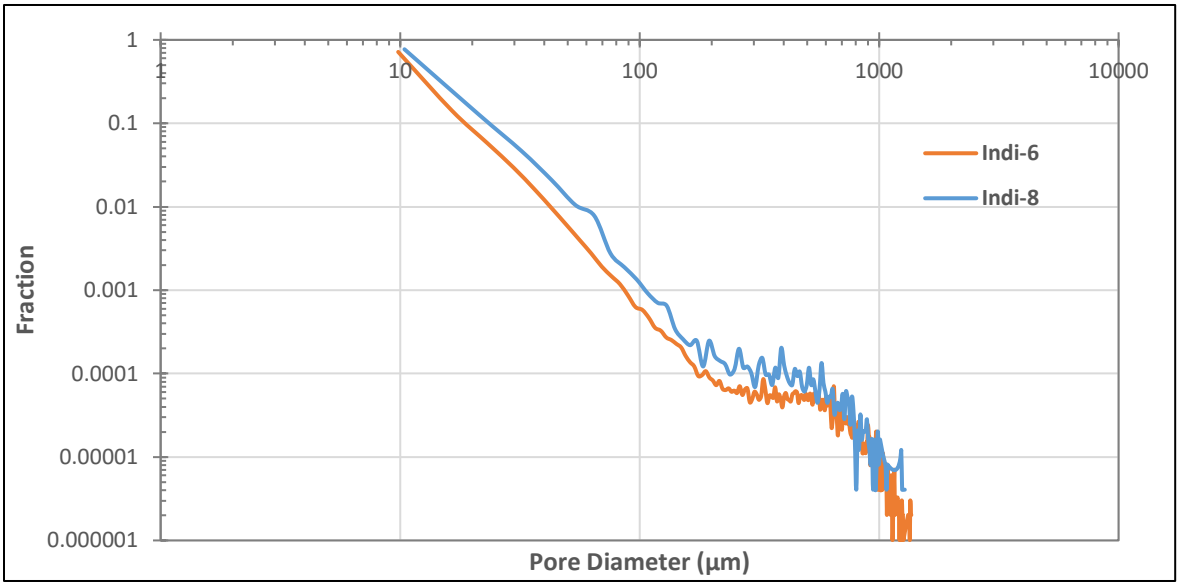

Figure 3.13: *Indi-6 and Indi-8 pore-size distribution comparison on log-log axes.*

As can be seen from **Figs. 3.12** and **3.13**, the distributions for the two samples are very similar. This will be especially apparent once the other Indiana Limestone samples are compared. The semi-log plot shows a slightly higher frequency of the smallest pores in the Indi-8 sample, which likely is why the mean pore diameter for Indi-8 (16.5 um) is slightly lower than that of the Indi-6 sample (17.4 um). Both samples show an almost identical slope on the log-log plot until around 200 µm, where they both plateau before decreasing again at the largest pore sizes. Since the distributions for the two samples and other parameters are very similar, only the Indi-6 sample will be used for subsequent comparisons with higher-permeability Indiana Limestone samples.

3.3.2.d – Indiana Limestone 6md vs. 10md

Fig 3.14 shows a comparison of pore-size distributions for Indi-6 and Indi-10 samples on semi-log axes.

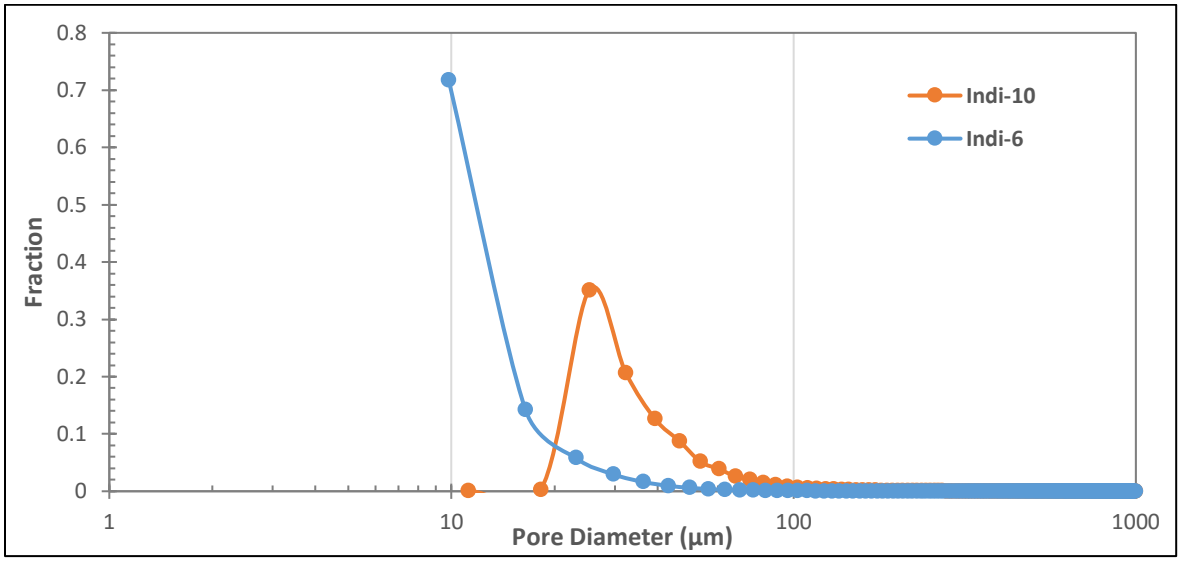

Figure 3.14: *Indi-6 and Indi-10 pore-size distribution comparison on semi-log axes.*

Fig. 3.15 shows a comparison of pore-size distribution for Indi-6 and Indi-10 samples on log-log axes.

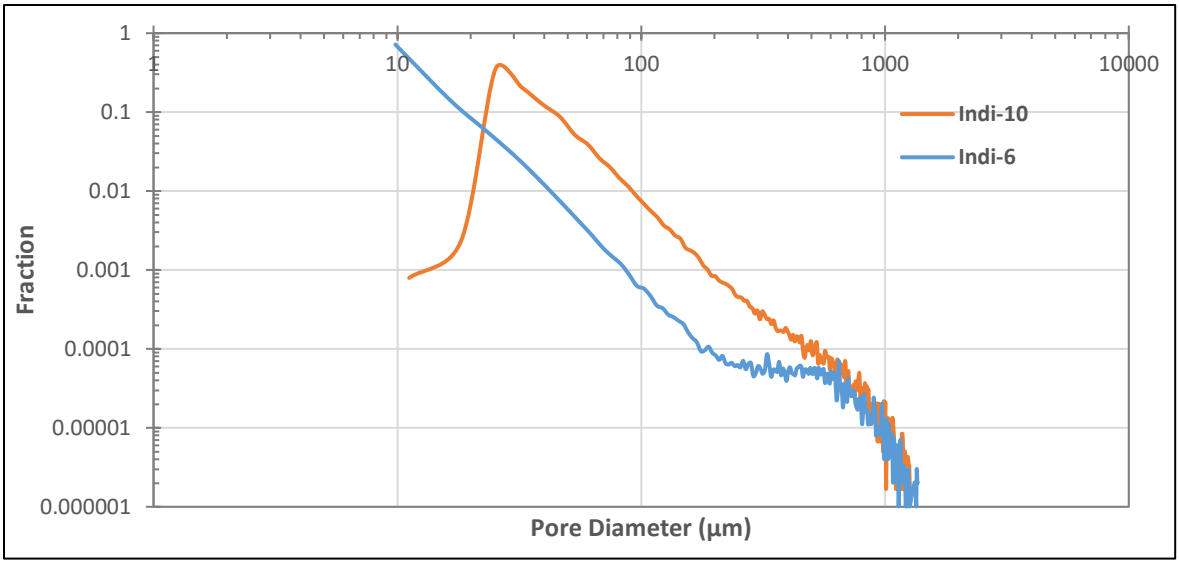

Figure 3.15: *Indi-6 and Indi-10 pore-size distribution comparison on log-log axes.*

From the above figures, the difference in shapes between these two samples is clear. In **Fig. 3.14** the Indi-6 sample has a very high frequency of small pores compared to the Indi-10 sample. This explains the rather large difference in average pore diameter for the Indi-6 sample vs. Indi-10 (17.4 µm vs. 47.8 µm, respectively). The same is shown in **Fig. 3.15**. The Indi-10 sample shows a higher frequency throughout entire range of pore values (excluding the smallest ones).

3.3.2.e – Indiana Limestone 10md vs. 239md

Fig. 3.16 shows a comparison of pore-size distribution for Indi-10 and Indi-239 samples on semi-log axes.

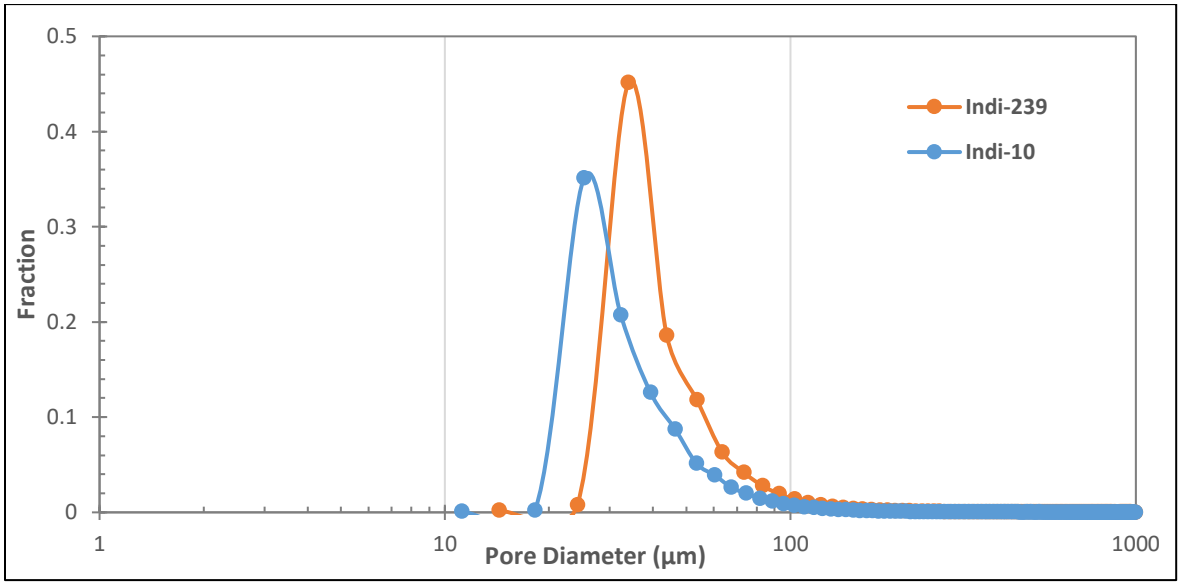

Figure 3.16: *Indi-10 and Indi-239 pore-size distribution comparison on semi-log axes.*

Fig. 3.17 shows a comparison of pore-size distribution for Indi-10 and Indi-239 samples on log-log axes.

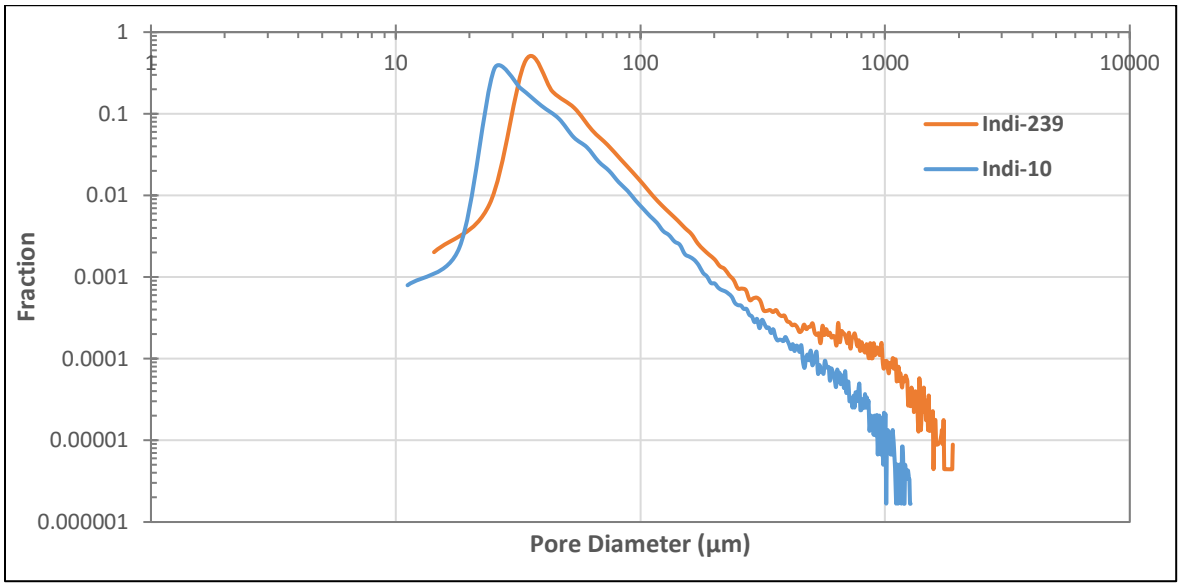

Figure 3.17: *Indi-10 and Indi-239 pore-size distribution comparison on log-log axes.*

As with previous comparisons, the rock with higher pore-size, permeability, and $PV_{bt,opt}$ shows a higher frequency of larger pores. This is observed in **Fig. 3.16** by a shift to the right of the main peak, or mode pore value. Additionally, in **Fig. 3.17,** the Indi-239 sample consistently shows a higher frequency of larger pores and also an extended plateau region that reaches higher pore sizes than the Indi-10 sample. Average pore size for the Indi-10 sample is 47.8 µm and is 62.8 µm for Indi-239.

3.3.2.f – Indiana Limestone Overall Comparison

This comparison plots the three main values of permeability against each other (Indi-8 is excluded since it is so similar to Indi-6, as seen in **Figs. 3.12** and **3.13**). Samples included are Indi-6, Indi-10, and Indi-239. **Fig. 3.18** shows the comparison of the aforementioned samples on semi-log axes.

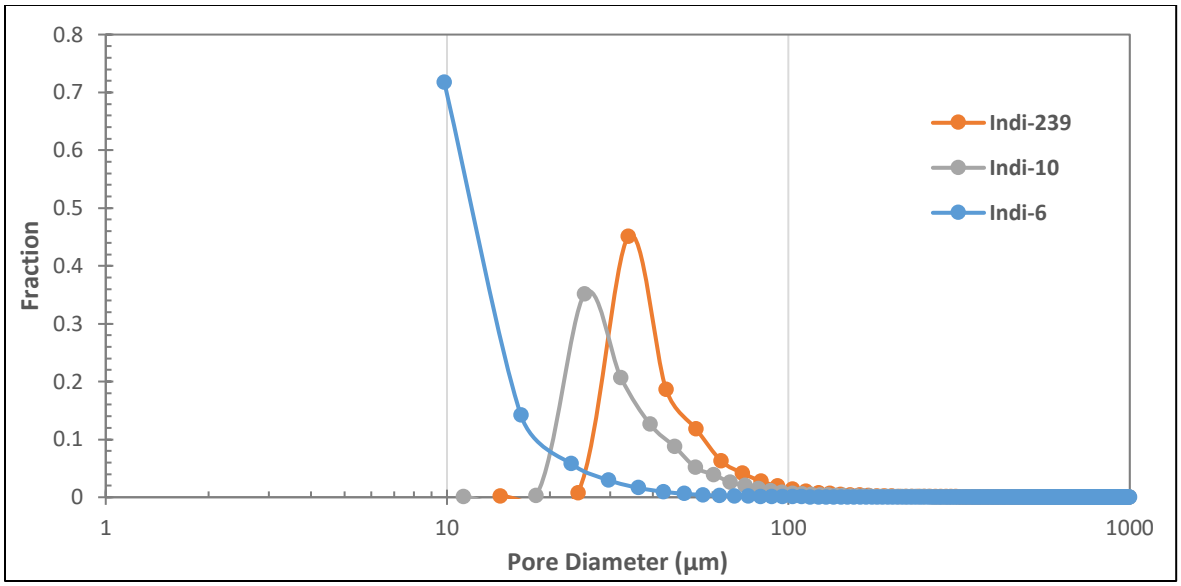

Figure 3.18: *Indi-6, Indi-10, and Indi-239 pore-size distribution comparison on semi-log axes.*

Fig. 3.19 shows a comparison of pore-size distributions for Indi-6, Indi-10, and Indi-239 samples on log-log axes.

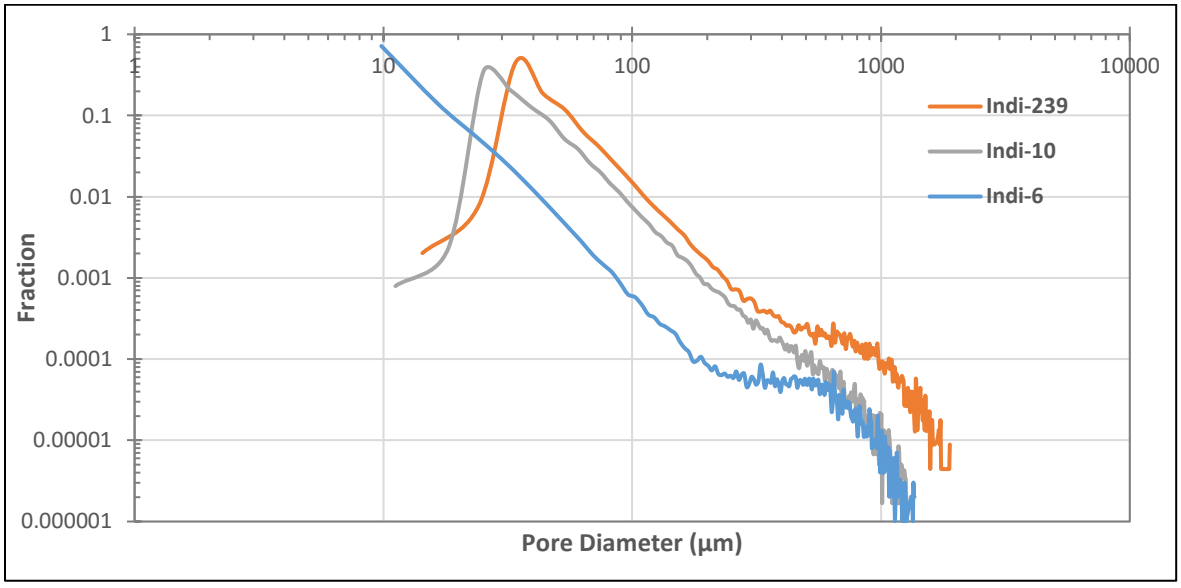

Figure 3.19: *Indi-6, Indi-10, and Indi-239 pore-size distribution comparison on log-log axes.*

Trends discussed in the previous sections remain in the comparison of the three Indiana Limestone samples. As mean pore size and $PV_{bt,opt}$ increase, the location of the peak in the semi-log plot moves to the right, and on the log-log plot the frequency of larger pores remains higher. One note is that despite the consistent trend of rightward peak movement in the semi-log plot, the height (frequency) of the mode value does not have a consistent trend. Although it is tempting to relate the decreased interstitial flux values to the reduction in peak height (2.92 cm/min for Indi-10 and 2.52 cm/min for Indi-239), the Indi-8 sample has the highest frequency of small pores and yet the lowest $v_{i,opt}$ (1.60 cm/min).

3.3.2.g - Travertine Limestone Comparison

Fig. 3.20 shows a comparison of pore-size distributions for Trav-70 and Trav-600 samples on semi-log axes.

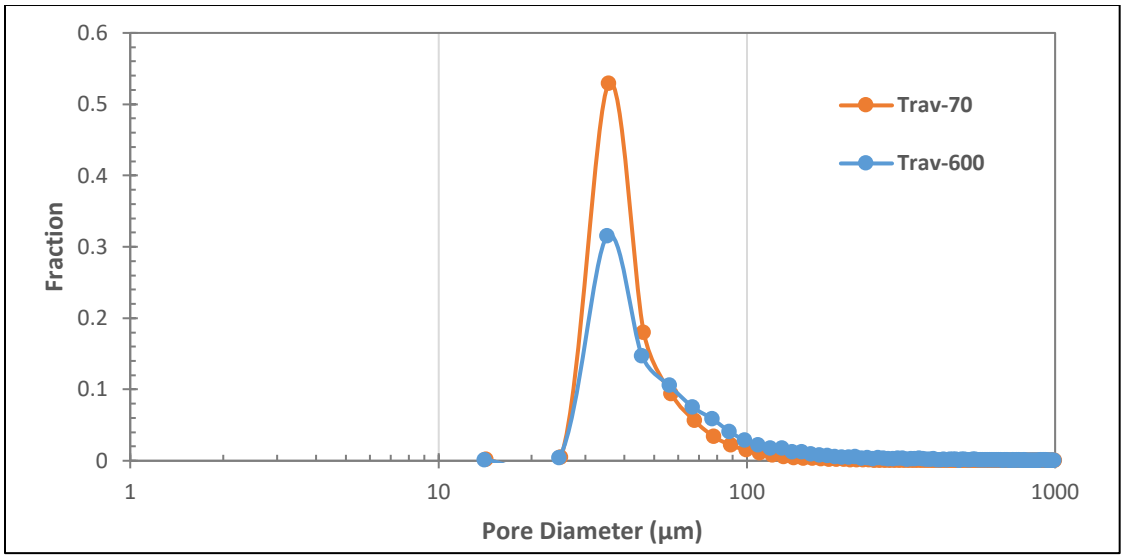

Figure 3.20: *Travertine pore-size distribution comparison on semi-log axes.*

Fig. 3.21 shows a comparison of pore-size distributions for Trav-70 and Trav-600 samples on log-log axes.

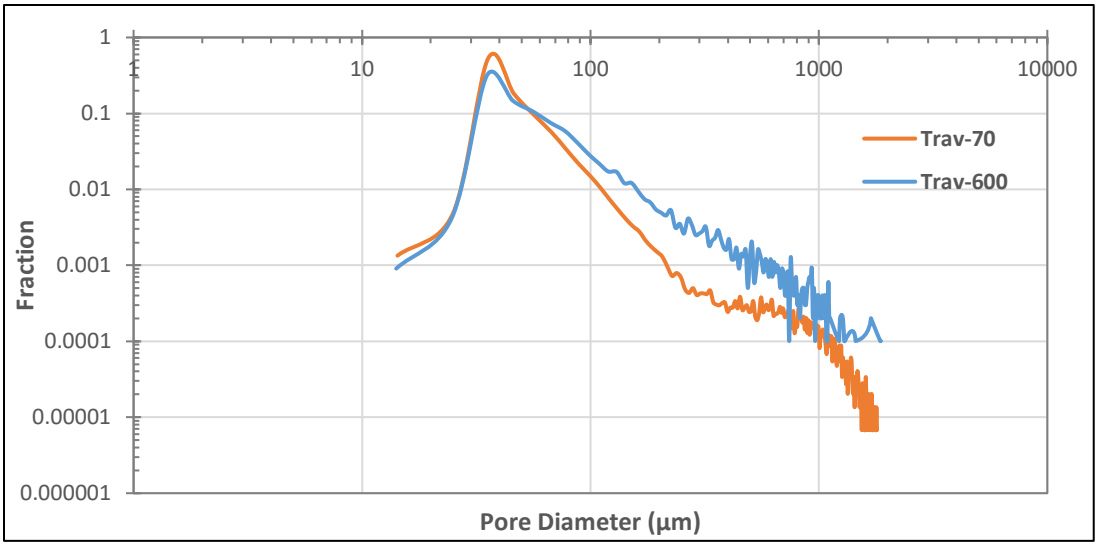

Figure 3.21: *Travertine pore-size distribution comparison on log-log axes.*

The Travertine comparison displays clear differences between the two samples. As with the other rock types, the semi-log plot shows that a lower permeability results in a higher frequency of small pores. However, different from Indiana Limestone, the Travertine peaks in **Fig. 3.20** are not shifted with respect to the *x*-axis. Rather, the peaks occur at the same mode pore value but the Trav-70 sample displays a noticeably higher frequency of these pores. Observing **Fig. 3.21**, Travertine is the only rock type of those studied in this work that displays a significantly different slope of the tail of the log-log plot. The slope is less for the Trav-600 sample, and also remains above the Trav-70 tail (indicating higher frequency of large pores for the Trav-600 sample). These differences indicate a significantly different pore structure of Travertine compared to Indiana Limestone based on qualitative comparison of pore-size distributions. This was also confirmed in acidizing tests, whereby Travertine displayed high degrees of permeability anisotropy as discussed in **Chapter II**. Trav-600 has a larger

$PV_{bt,opt}$ compared with the Trav-70 sample (0.70 vs. 0.49) and a lower $vi_{,opt}$ (20.0 cm/min vs. 24.5 cm/min, respectively).

3.3.2.h – Pore-Size Distribution Comparison Between Different Rock Types

In this section, a comparison of DP1-33, Indi-239, and Trav-600 is made to observe the differences in pore-size distribution among carbonates with different pore structure but similar $PV_{bt,opt}$ values. This comparison is shown in **Fig. 3.22** on semi-log axes. The optimum breakthrough values of the rocks, ordered as they are listed above (and top-to-bottom on the **Fig. 3.22** legend), are 0.64, 0.75, and 0.7.

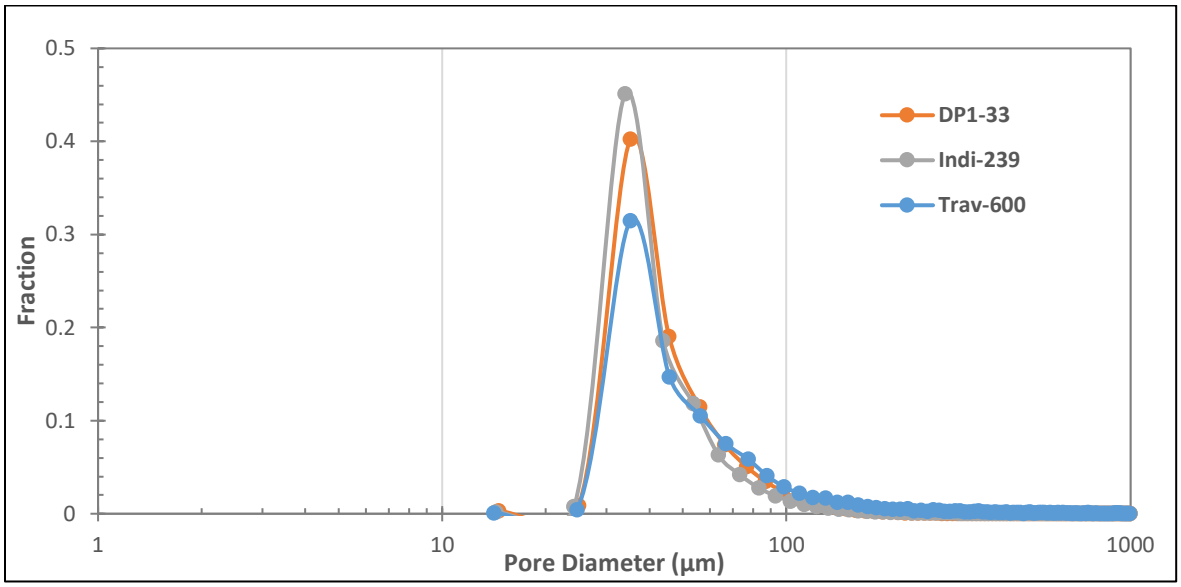

Figure 3.22: *Comparison of rocks with similar* $PV_{bt,opt}$ *(DP1-33, Indi-239, and Trav-600) on semi-log axes.*

Fig. 3.23 shows a comparison of pore-size distribution for rocks with similar $PV_{bt,opt}$ values (DP1-33, Indi-239, Trav-600) on log-log axes.

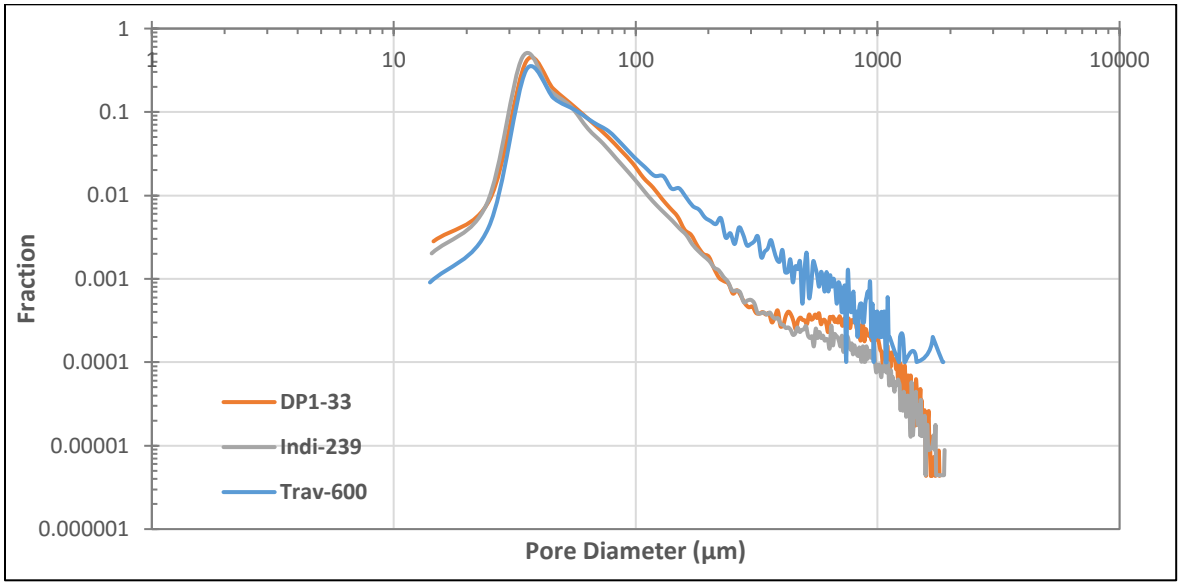

Figure 3.23: *Comparison of rocks with similar* $PV_{bt,opt}$ *(DP1-33, Indi-239, and Trav-600) on log-log axes.*

The pore-size distributions for rocks of comparable $PV_{bt,opt}$ values are strikingly similar, especially those of DP1-33 and Indi-239. Note in **Fig. 3.22** that all samples have approximately the same mode pore value, with slightly different frequency levels. Observing **Fig. 3.23,** DP1-33 and Indi-239 show almost identical patterns on log-log axes, despite the much larger permeability value of Indiana Limestone vs. Desert Pink samples. The permeability (600md) and mean pore volume (3,965,680 um^3) of the plotted Travertine sample is so much higher than the others that it remains above them in the log-log plot, but the slope only diverges after reaching a pore size of approximately 100 µm. Conversely, the median pore size of DP1-33 and Indi-239 is almost identical (44.4µm and 40.2 µm, respectively), although the mean pore volume between these two samples is quite different. Likewise, the median pore diameter of Trav-600 (54.4 µm) is not too much higher than the other two

plotted samples. This suggests that pore diameter is more closely related to $PV_{bt,opt}$ than pore volume, a concept which will be explored further in **Chapter IV.**

Unfortunately, in this study there are no two samples of different rock types that share similar values of $v_{i,opt}$. The two closest values in the study are between Indi-6 and Indi-8. Considering different rock types, the closest values are between Indi-10 (2.92 cm/min) and Desert Pink (3.25 cm/min). **Fig. 3.24** shows a comparison of these distributions on semi-log axes.

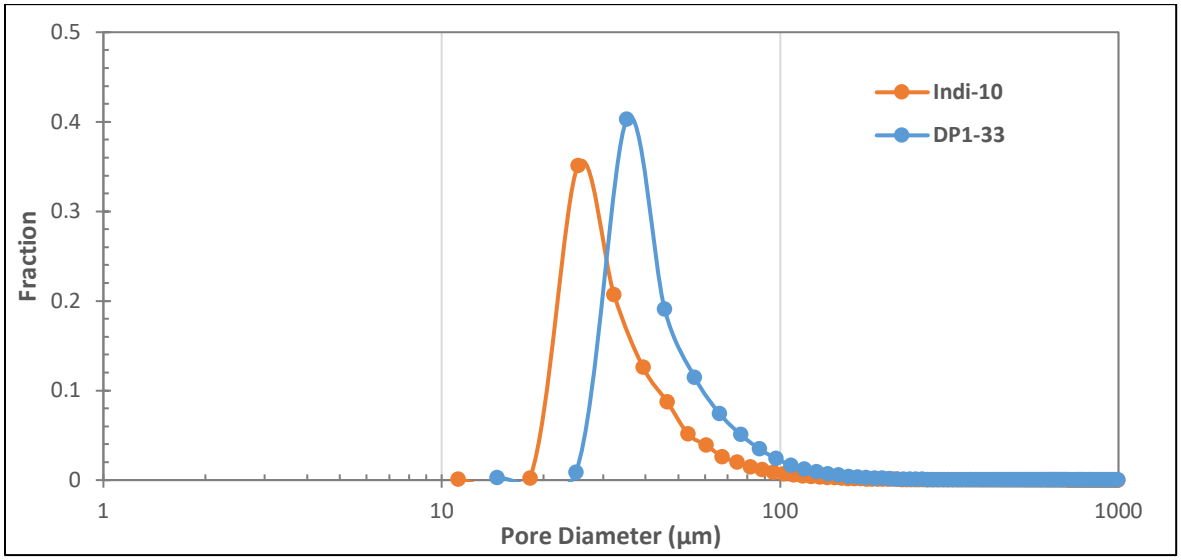

Figure 3.24: *Comparison of rocks with similar* $v_{i,opt}$ *(Indi-10 and DP1-33) on semi-log axes.*

Fig. 3.25 shows a comparison of rocks with similar $v_{i,opt}$ values (Indi-10 and DP1-33) on log-log axes.

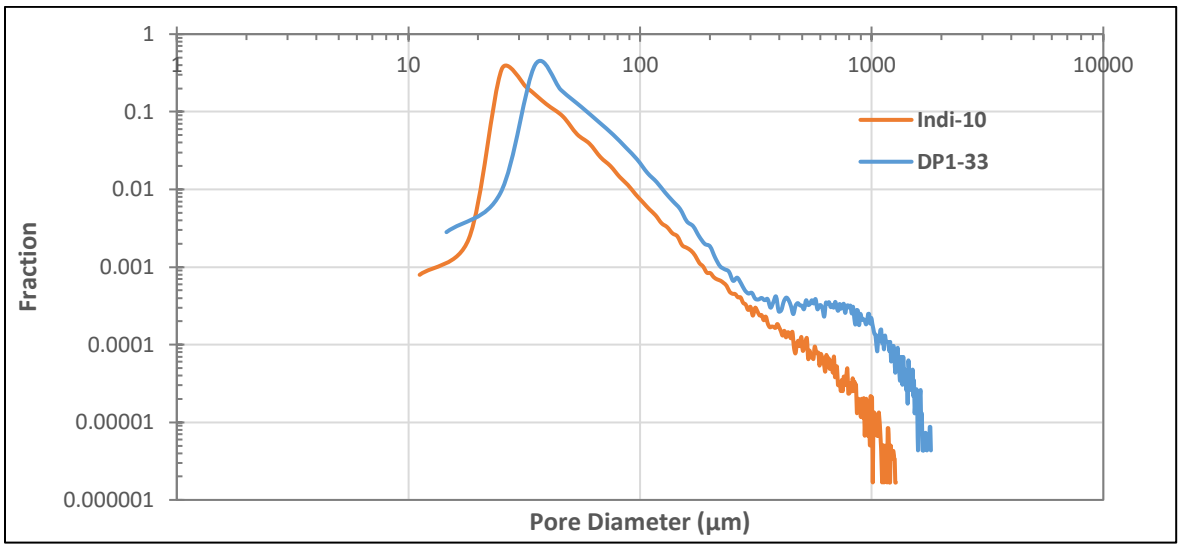

Figure 3.25: *Comparison of rocks with similar* $v_{i,opt}$ *(Indi-10 and DP1-33) on log-log axes.*

Comparison of the above figures does not yield any immediately noticeable similarity as in the $PV_{bt,opt}$ case. Note that the smallest resolved pore for each sample is different. This is due to resolution differences in the sample, which is 8 µm/voxel for DP1-33 and 6.5 µm/voxel for Indi-10. Since Indiana Limestone has a higher resolution, the minimum resolved pore size is smaller. The peak frequency values are similar, but this is also a feature shared among rocks in the $PV_{bt,opt}$ comparison (**Figs. 3.22** and **3.23**) and Trav-600 in that case has a $v_{i,opt}$ value of 20 cm/min. The slopes on the log-log plot in **Fig. 3.25** are similar, but again this is a feature shared by all of the rock samples except Trav-600. Also, recall that the Travertine sample comparison (**Figs. 3.20** and **3.21**) share similar optimum flux values but display different log-log slopes. A trend relating $v_{i,opt}$ to pore structure remains elusive based on qualitative observation of pore-size distributions alone, but the concept will be explored further in subsequent sections of this thesis.

3.4 – Lognormal Fitting of Pore-Size Distributions

In this section, each of the semi-log pore-size distributions is fit with the lognormal function shown in **Eq. 2.1,** with variables μ and σ altered to obtain an optimum fit. Values of μ and σ are displayed in **Table 3.5**, as determined by the distribution fitting toolbox in MATLAB.

Table 3.5: Optimum values of fitted parameters and associated standard error as calculated by the distribution fitting toolbox in MATLAB.

Rock Sample	μ parameter	σ parameter	μ Standard Error	σ Standard Error
DP1-33	3.97	0.588	0.00123	0.00087
DP2-33	4.03	0.827	0.00219	0.00155
Indi-6	2.54	0.512	0.00053	0.00038
Indi-8	2.59	0.531	0.00107	0.00076
Indi-10	3.65	0.513	0.00066	0.00047
Indi-239	3.88	0.540	0.00114	0.00081
Trav-70	3.88	0.530	0.00138	0.00098
Trav-600	4.25	0.824	0.00826	0.00584

As can be seen from the standard error sections of the table, the lognormal fitting was in general very accurate. However, the curve fitting toolbox did have problems reaching the peak values of the pore-size distributions, especially for those with very high frequency peaks such as Indi-6 and Indi-8. Correlations of the values shown in **Table 3.5** versus optimum acidizing parameters will be explored in **Chapter IV**. In addition to the optimum fitted values shown above, other information can be gained from the fitted lognormal distribution. These parameters include the mean, median, mode, variance, skewness, and kurtosis of the fitted distribution. Note that the values of mean and median calculated here are not necessarily the same as those listed in previous sections, as in **Table 3.3.** The previous values are calculated strictly from datasets of labeled pores, while values calculated from the fitted

distribution depend on the accuracy of the fit. **Table 3.6** lists parameters calculated from the fitted distribution.

Table 3.6: Parameters calculated from pore-size distribution fit.

Rock Sample	Mean	Median	Mode	Variance	Skewness	Kurtosis
DP1-33	63.2	53.1	37.6	1649	2.46	9.63
DP2-33	79.0	56.1	28.3	6120	3.40	36.7
Indi-6	14.4	12.6	9.7	62	2.28	6.32
Indi-8	15.3	13.3	10.1	77	2.32	7.01
Indi-10	44.1	38.6	29.7	586	2.28	6.36
Indi-239	56.2	48.6	36.3	1070	2.34	7.39
Trav-70	55.8	48.4	36.6	1009	2.32	6.99
Trav-600	98.3	70.0	35.5	9386	3.38	36.1

Other than the standard error value listed in **Table 3.5,** another way to measure accuracy of distribution fit is to plot the distribution mean pore diameter versus the mean pore diameter calculated from image analysis. This plot is shown below in **Fig. 3.26.**

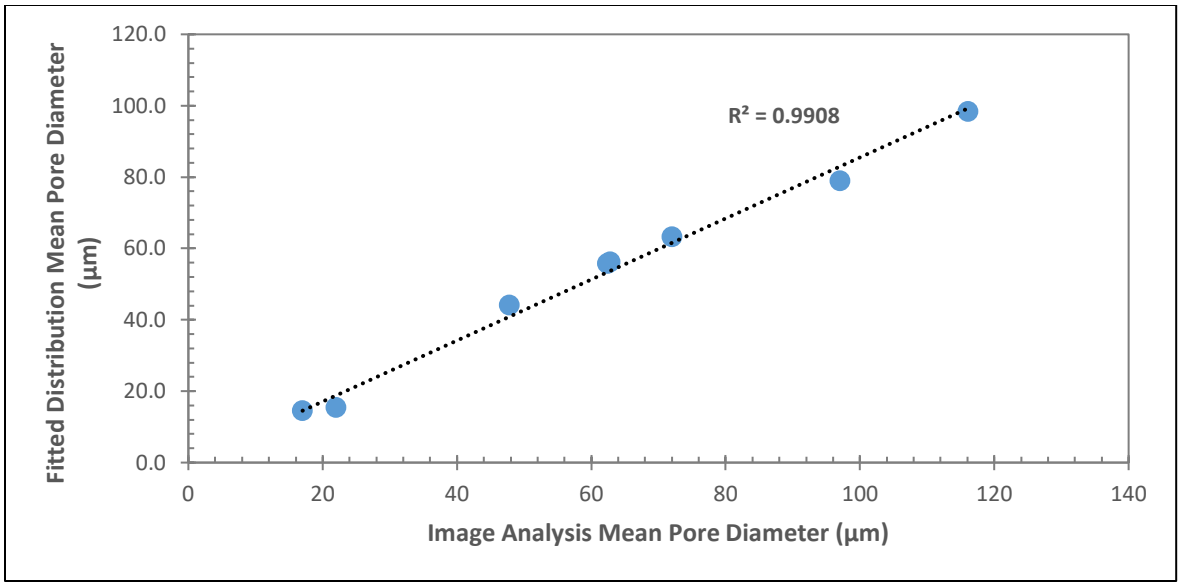

Figure 3.26: *Comparison of mean pore diameters calculated from fitted distribution versus calculated from imaging analysis.*

As can be seen from the above plot, the mean pore diameters show excellent agreement, further verifying the accuracy of the lognormal fit. We also can observe the mode value of the fitted distribution, which represents the pore diameter at which the frequency is highest. This value corresponds well to the location of the peaks of semi-log distributions in **Sections 3.3.1** and **3.3.2** of this thesis. For example, observe **Fig. 3.18**, the comparison of Indi-6, Indi-10, and Indi-239, and compare it with listed mode values in **Table 3.6.** Notice that the mode value increases with Indiana Limestone permeability, and that mode values of Indi-6 and Indi-8 are virtually identical. This is consistent with the Indiana Limestone pore-size distribution comparison. Additionally, note that the mode values listed for Travertine samples are very similar, same as in **Fig. 3.20,** which compares Travertine distributions. Finally, the rocks with similar $PV_{bt,opt}$ compared in **Fig. 3.22** (DP1-33, Indi-239, and Trav-600) also share similar mode values (37.6, 36.3, and 35.5, respectively), in accordance with the plot.

Further analysis of fitted distribution parameters and their relationship with optimum acidizing values will be shown in **Chapter IV.**

CHAPTER IV

DISCUSSION

This chapter will focus on applying results from Chapter III to determine useful correlations with optimum acidizing parameters. The first section shows that permeability and porosity are not enough to determine such a relationship on their own. Subsequent sections use values determined from fitted pore-size distributions to attempt to correlate optimum acidizing parameters with other measurable variables.

4.1– Permeability and Porosity Correlations

This section shows that for the samples considered in this study, optimum acidizing parameters do not show good correlations with either permeability or porosity. This conclusion leads to further investigation of other parameters that may allow more accurate prediction of optimum wormholing conditions.

4.1.1 – $PV_{bt,opt}$ Correlation with Permeability and Porosity

Fig. 4.1 shows a comparison of optimal pore volumes to breakthrough plotted against permeability and porosity of samples used in this study.

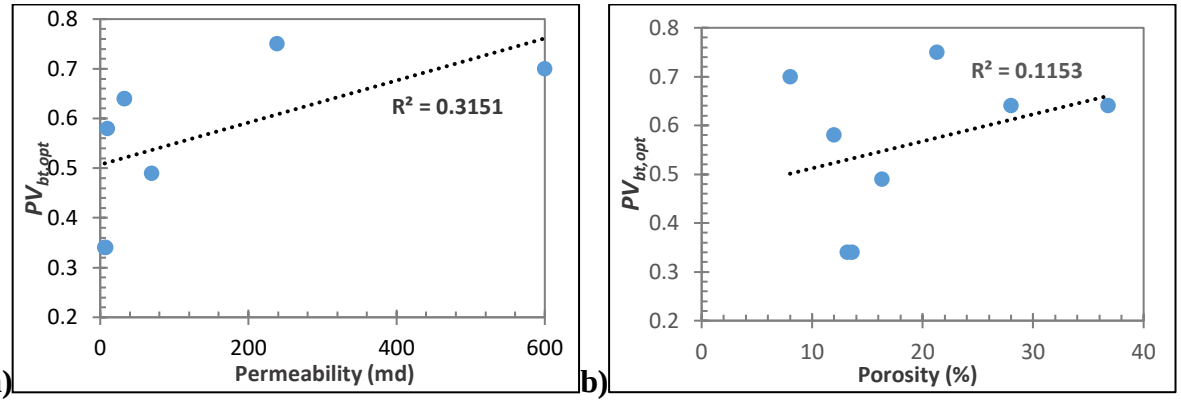

Figure 4.1: *Comparison of* $PV_{bt,opt}$ *vs. a) permeability and b) porosity*

Observing **Figs. 4.1a** and **4.1b**, we find no good correlation between optimum pore-volumes to breakthrough and either permeability or porosity. As has been discussed previously, there does appear to be a trend of increasing $PV_{bt,opt}$ with permeability, but the linear fit proposed in **Fig 4.1a** is far from satisfactory with an R^2 value of 0.3. Using a logarithmic asymptotic fit for the permeability correlation gives a better R^2 value of 0.6, but there does not appear to be any physical reason that $PV_{bt,opt}$ should reach an asymptote as permeability increases. Thus, we cannot be sure which fit is appropriate but in either case the fit is not ideal and prediction of $PV_{bt,opt}$ from permeability values remains difficult. It is worth mentioning that Etten et al., (2015) applied a logarithmic trendline for the comparison in **Fig. 4.1a,** however her study only included 3 Indiana Limestone samples and one Desert Pink sample. In her study there was no justification for use of a logarithmic fit except that it provided the highest R^2 value. In general, $PV_{bt,opt}$ appears to increase with porosity, but no clear trend is discernable according to **Fig. 4.1b.** Although the result is not shown, there is no clear trend of permeability vs. porosity for the rock types used in this work.

4.1.2 – $v_{i,opt}$ Correlation with Permeability and Porosity

Fig. 4.2 shows a comparison of optimal interstitial flux versus permeability and porosity of samples used in this study.

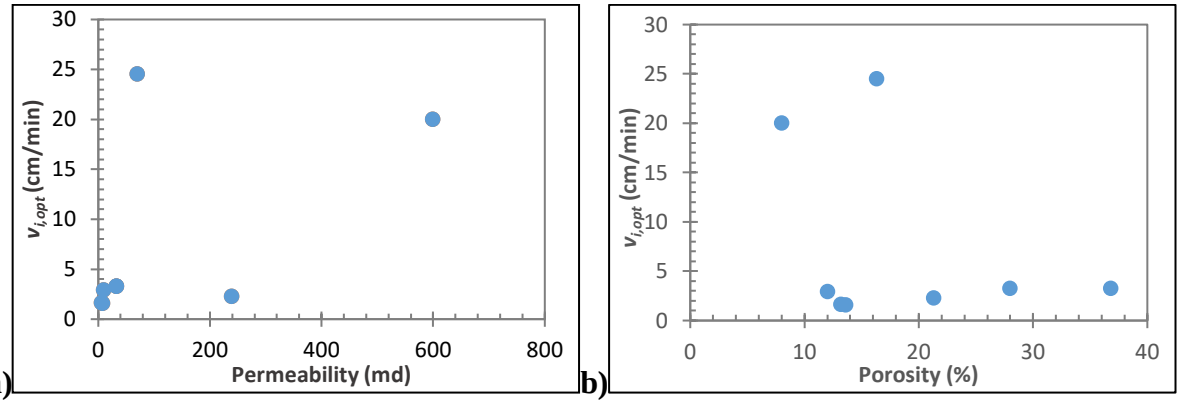

Figure 4.2: Comparison of $v_{i,opt}$ vs. a) permeability and b) porosity.

The correlations for $v_{i,opt}$ are even less observed than those for $PV_{bt,opt}$. The high optimum flux values of the Travertine samples at both low (70 md) and high (600 md) permeability illustrate that a consistent trend between permeability and optimum flux is not present between the rock types discussed in this study, as seen in **Fig. 4.2a**. Similarly, porosity alone is inadequate to accurately predict changes in $v_{i,opt}$, as shown in **Fig. 4.2b.**

4.2 – Fitted Parameter Correlations

The purpose of the above section is to show that neither porosity nor permeability alone is sufficient to accurately predict changes in optimum acidizing parameters across different carbonate types. The following section considers correlations between optimum parameters and the fitted variables, μ and σ (see **Eq 2.1**), calculated from the pore-size distributions and listed in **Table 3.5.** Since the pore-size distribution encompasses a description of the entire rock sample, rather than just a single average value such as permeability or porosity, the idea is that these fitted variables may yield better correlations to optimum acidizing parameters. The assumption made here is that $PV_{bt,opt}$ and $v_{i,opt}$ are controlled by pore structure, which is a concept widely reviewed in **Chapter I** and **Chapter II** of this work.

4.2.1 – $PV_{bt,opt}$ Correlation (μ and σ)

Fig. 4.3 shows the location parameter, μ, from the fitted distribution plotted against optimum pore volumes to breakthrough. The plot is fit with an exponential trendline.

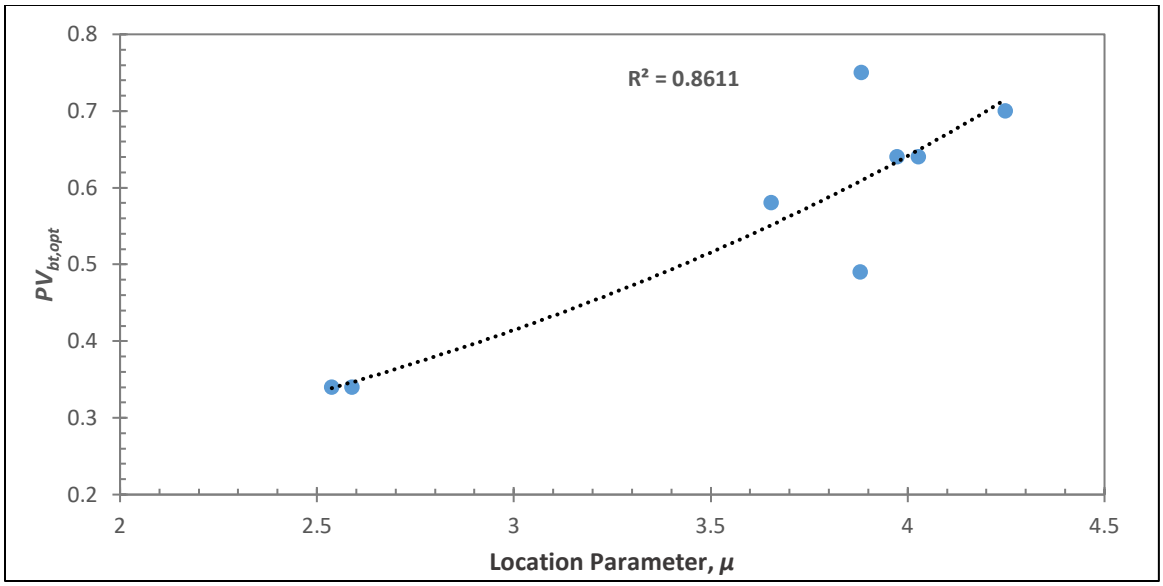

Figure 4.3: $PV_{bt,opt}$ *plotted against lognormal fitted parameter* μ (*exponential trendline).*

The location parameter is related to the mean, median, and mode of the fitted distribution, and thus the *x*-axis location of the peak. As seen in the **Chapter III**, larger $PV_{bt,opt}$ values tended to move the distribution to the right, to higher values of mode pore size. While it is not surprising to see that the location parameter is positively related to $PV_{bt,opt}$, the degree of fit is encouraging, showing an R^2 value of 0.86 for an exponential fit. It is not clear exactly which type of fit is appropriate, as a linear fit also gives a high R^2 value of 0.80. Regardless, there is a clear positive correlation between the two variables that is better than trends with porosity or permeability alone (see **Fig. 4.1**). Thus, we can already see that using the pore-size distribution as a method of quantifying the entire rock structure is a superior method than just an average value of permeability or porosity alone. **Fig. 4.4** shows $PV_{bt,opt}$ plotted against the shape parameter, σ.

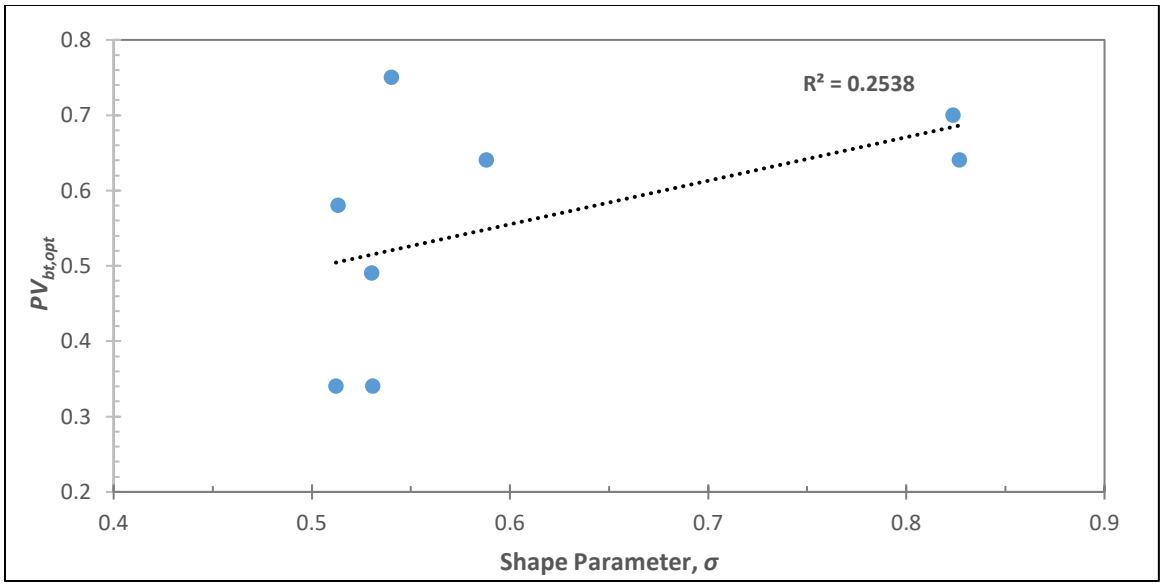

Figure 4.4: $PV_{bt,opt}$ *plotted against lognormal fitted parameter σ (linear trendline).*

The shape parameter is related to the skewness and kurtosis of the fitted distribution. These parameters effect the *y*-axis height (frequency) of the mode value, and the steepness of the distribution tails. It is also somewhat related to the variance. There is no direct correlation between $PV_{bt,opt}$ and σ as shown in **Fig. 4.4.** In general, the shape parameter values are very close to each other except for two outliers, which are DP2-33 and Trav-600 (**Table 3.5**). These are the samples with the highest mean pore volume, mean pore diameter (**Table 3.3**), skewness, and kurtosis (**Table 3.6**). Recall that the distribution of DP2-33 was unique in that it featured a prominent secondary peak especially apparent on the log-log axes (**Figs. 3.3** and **3.11**). Even if these outlier σ values are removed, there remains no trend between the remaining values of shape parameter when compared with $PV_{bt,opt}$. Also note that while not shown in this work, there are no adequate trends between either μ or σ and permeability or porosity.

4.2.2 – $v_{i,opt}$ Correlation (μ and σ)

Fig. 4.5 shows $v_{i,opt}$ plotted against the location parameter, μ, generated from each fitted lognormal distribution.

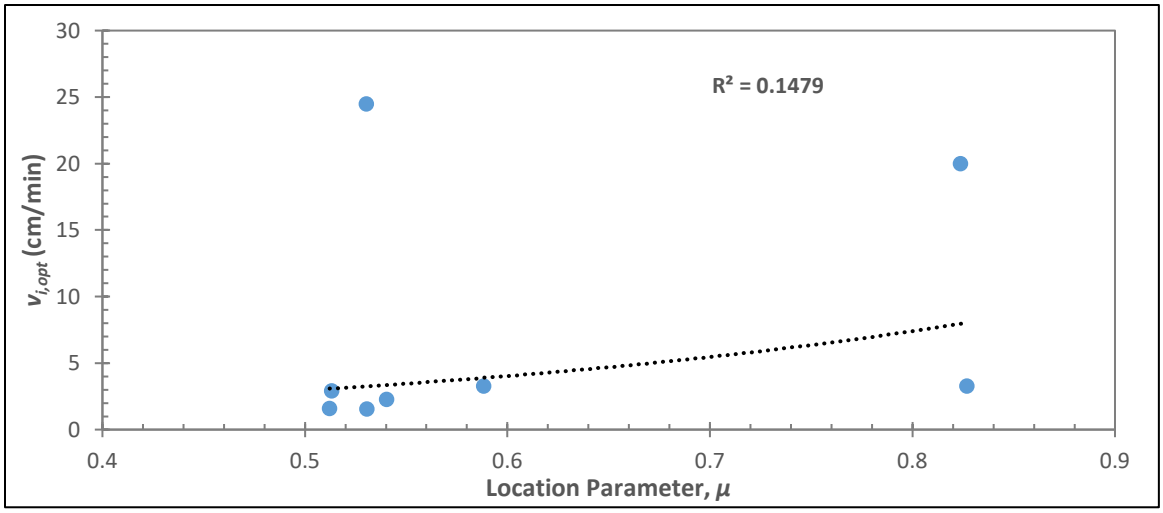

Figure 4.5: $v_{i,opt}$ *plotted against lognormal fitted parameter* μ *(exponential trendline).*

Fig. 4.6 shows $v_{i,opt}$ plotted against the shape parameter, σ, generated from fitted distributions.

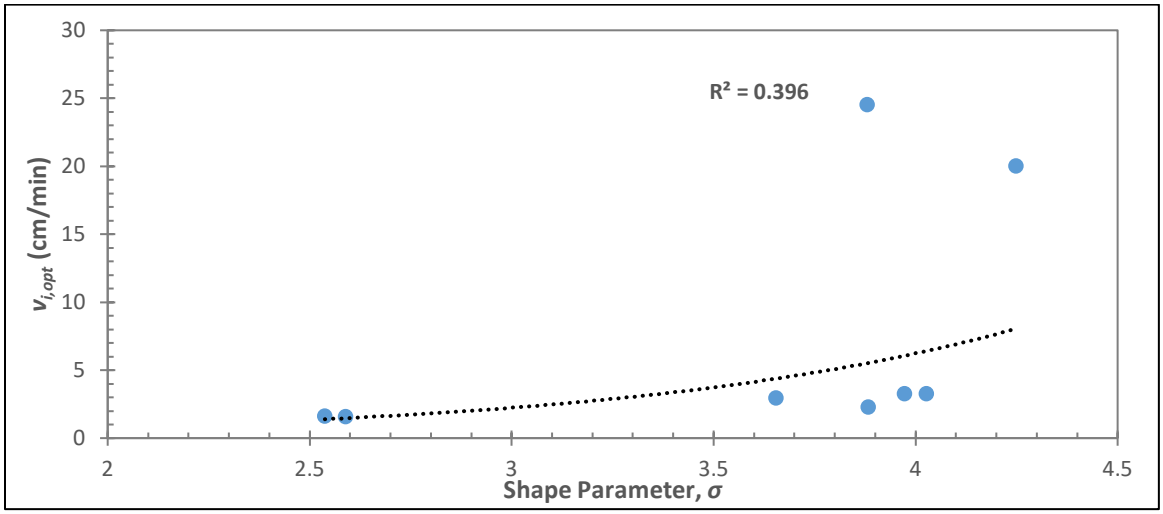

Figure 4.6: $v_{i,opt}$ *plotted against lognormal fitted parameter* σ *(exponential trendline).*

A correlation between $v_{i,opt}$ and fitted distribution variables remains elusive, as no acceptable correlation is found in **Figs. 4.5** and **4.6.** The large variation in optimal flux values, especially for Trav-70 and Trav-600 (24.5 and 20.0 cm/min, respectively) make finding an acceptable correlation difficult. However, even without these large outliers, no trend is seen for either shape or location parameter. The correlation in **Fig. 4.6** is slightly better (R^2 of 0.4 with an exponential trendline), which at least indicates that $v_{i,opt}$ is more affected by distribution shape (skewness and kurtosis) than by the location (mean, median, and mode pore size), which could be useful information for future study.

4.3 – Fitted Distribution Parameter Comparison

While the previous section dealt with correlations relating optimum fitted parameters and acidizing results, additional information is also available from the fitted distribution: namely the mean, median, mode, skewness, and kurtosis of the distributions. These values are presented in **Table 3.6** As mentioned in previous sections, the location parameter is related to the mean, median, and mode, while the shape parameter is related to the skewness and kurtosis. Variance is related to both parameters. Note that mean and median pore diameters in this section are calculated from the fitted distribution, not from the actual digital pore data. This decision is discussed in more detail in **Chapter III** and a plot confirming mean diameter similarity presented in **Fig. 3.26.**

4.3.1 – $PV_{bt,opt}$ Correlation (Mean, Median, Mode, Skewness, Kurtosis, and Variance)

In this section, all plots will be presented first and discussion will follow afterwards. **Fig. 4.7** shows $PV_{bt,opt}$ plotted against the mean, median, and mode pore diameters as calculated from the fitted lognormal distribution. Each plot in **Fig 4.7** is fit with a power-law trendline.

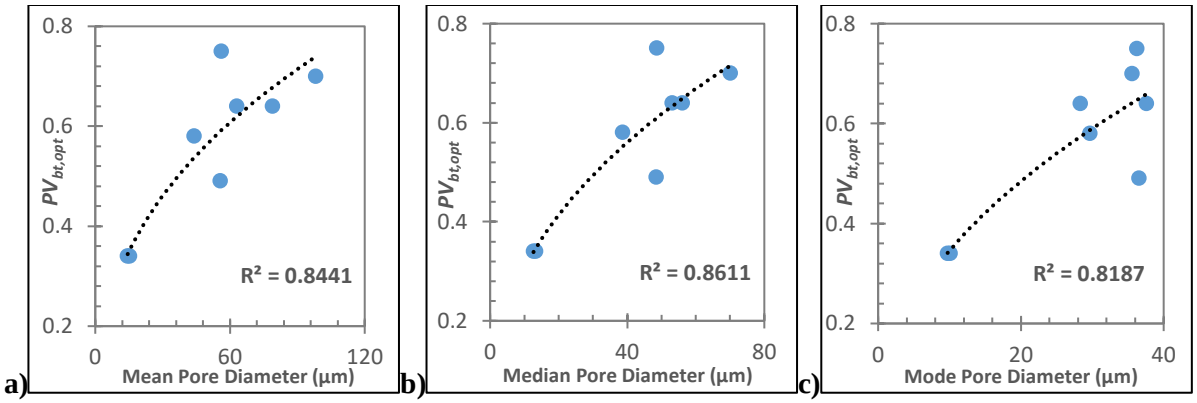

Figure 4.7: $PV_{bt,opt}$ *vs. a) mean pore diameter, b) median pore diameter, and c) mode pore diameter (all fit with power-law trendlines).*

Fig. 4.8 shows $PV_{bt,opt}$ plotted against the fitted distribution skewness, kurtosis, and variance. Trendlines used are as follows: linear for skewness plot, power-law for kurtosis plot, and logarithmic for the variance plot.

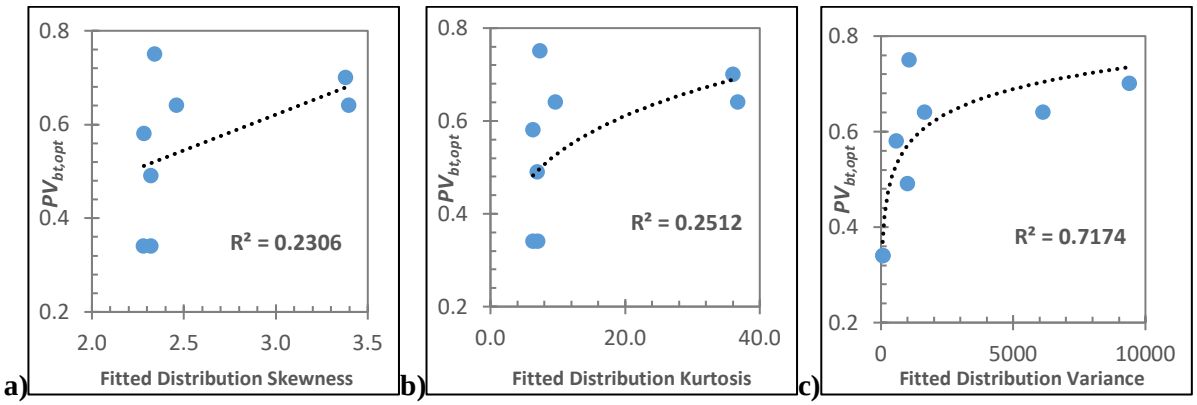

Figure 4.8: $PV_{bt,opt}$ *vs. fitted distribution a) skewness (linear trendline), b) kurtosis (power-law trendline), and c) variance (logarithmic trendline).*

As seen in **Fig. 4.7**, consistently excellent correlations are found between $PV_{bt,opt}$ and mean, median, and mode pore size. This is consistent with both qualitative pore-size distribution results and location parameter correlation results as shown in **Fig. 4.3** (since location parameter is most related to the three parameters in **Fig 4.7**). It is clear that the optimum breakthrough condition across all rock types presented in this study is correlated positively with pore size. **Figs. 4.8a** and **4.8b** show poor

correlations with kurtosis and skewness values, which are better described by the shape parameter. Recall **Fig. 4.4**, which showed a weak correlation between shape parameter and $PV_{bt,opt}$.

On the other hand, **Fig. 4.8c** shows a good correlation with variance, but only if the trendline used is either power-law or logarithmic. Using a linear trendline results in an R^2 value of just 0.3, so the authenticity of the trend is unclear. Variance is a measure of the difference between the smallest and largest pores, so it could be logically used as a measure of heterogeneity of the rock sample with regard to pore size. While not plotted here, variance values in this work have a positive correlation with permeability (also a rough measure of heterogeneity) across all rock types, showing an R^2 value of 0.6 with a linear trendline.

As discussed in **Chapter I**, highly heterogeneous and permeable rocks tend to require more acid to breakthough, indicating higher $PV_{bt,opt}$ values and confirming the trend seen in **Fig. 4.8c**. However, Izgec et al. (2009) presented results that showed vuggy carbonates with large-scale heterogeneities had very low optimum breakthrough values. Thus, we cannot make a final conclusion regarding the variance value's effect on $PV_{bt,opt}$ from the results presented.

4.3.2 – $v_{i,opt}$ Correlation (Mean, Median, Mode, Skewness, Kurtosis, and Variance)

This section presents results similar to the previous one, but instead with correlations relating to the optimum interstitial flux. Again, mean and median values used are from distribution fitting, not from image analysis. Plotted results will be presented, followed by a discussion. **Fig. 4.9** shows $v_{i,opt}$ plotted against the mean, median, and mode pore diameters as calculated from the fitted lognormal distribution. Each plot in **Fig 4.9** is fit with an exponential trendline.

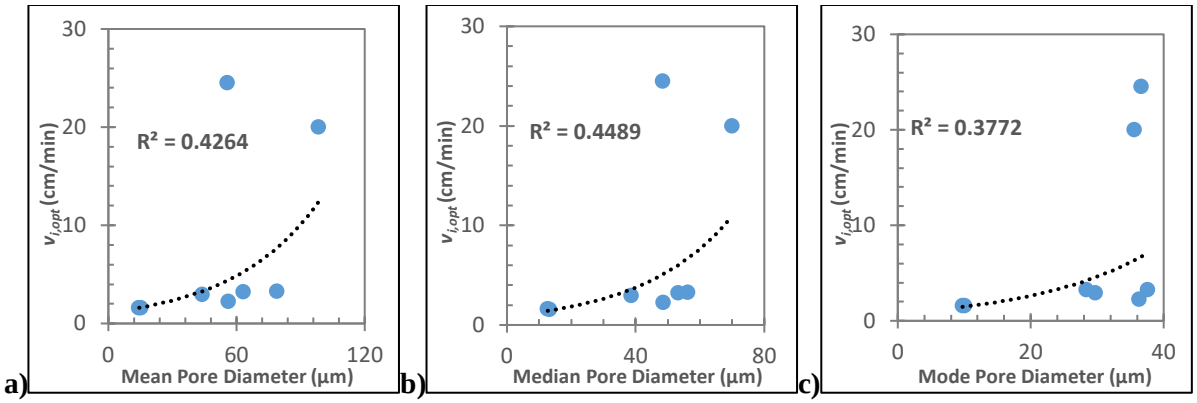

Figure 4.9: $v_{i,opt}$ *vs. a) mean pore diameter, b) median pore diameter, and c) mode pore diameter (all fit with exponential trendlines).*

Fig. 4.10 shows $v_{i,opt}$ plotted against the fitted distribution skewness, kurtosis, and variance. Trendlines are not plotted on any graph since no acceptable trend is found in any case regardless of the type of fit used.

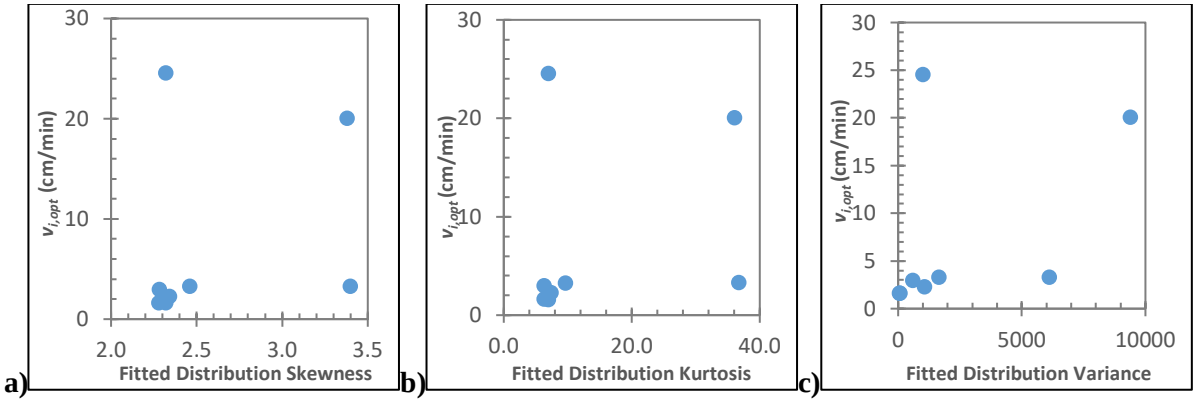

Figure 4.10: $v_{i,opt}$ *vs. fitted distribution a) skewness, b) kurtosis, and c) variance. No acceptable trends are found.*

As seen from **Figs. 4.9** and **4.10**, a prominent trend relating optimum flux to distribution parameters has not been revealed. While the mean, median, and mode trends in **Fig. 4.9** show a better R^2 value than that of the location parameter plot (**Fig. 4.5**), the fit is not ideal and is questionable without inclusion of the high-value Travertine samples. Without these, the exponential trend is no longer

acceptable and the R^2 value drops. The skewness, kurtosis, and variance graphs (**Fig. 4.10**) do not show any trend and so a trendline has not been plotted.

In **Chapter III**, a consistent qualitative trend for $v_{i,opt}$ based on pore-size distribution shape could not be attained. The only noticeable trend is that the optimum velocity seems to drop when approaching high permeability samples, such as from Indi-10 to Indi-239 (2.92 cm/min vs. 2.25 cm/min, respectively) and from Trav-70 to Trav-600 (from 24.5 cm/min to 20.0 cm/min). However, at lower permeability, such as Indi-6, Indi-8, and Indi-10, the interstitial flux rises. It could be that the interstitial flux is actually related to permeability, but core acidizing at high permeability/heterogeneity is difficult to maintain the same pore structure amongst all cores required for the efficiency curve. This is especially noted in the Etten et al. (2015) study, where standard deviation of permeability among Indi-239 cores was 132 md. While the average core permeability in that study was 239 md among 6 cores, the measured permeability ranged from 131md – 480md for these cores used to create the efficiency curve. It is possible that this affected the $v_{i,opt}$ measurement for the "239 md" cores, which is the value used in this current work (2.25 cm/min). A similar argument could be made for Travertine cores, considering the high permeability anisotropy of this rock type. In any case, a final conclusion based on the presented data cannot be made relating $v_{i,opt}$ to pore-size distribution parameters.

4.4 – Image Analysis Comparison – Additional Measures

This section compares some additional results of digital analysis with optimum acidizing parameters. While not the specific focus of this study, these measurements are easily taken by the image analysis software and remain interesting comparisons. In this section, pore count, interfacial area, and mean and median pore volume will be compared to both $PV_{bt,opt}$ and $v_{i,opt}$. **Table 4.1** shows pore count and interfacial area calculated for each rock type. Recall in **Chapter II** that the digital pore volume analyzed was normalized to $0.5cm^3$ for all samples (**Fig. 2.2**). The exception is Indi-8, which did not have enough digital data to reach this volume, so it is excluded from the pore count plots.

Interfacial area is calculated as the total surface area of the interface between pores and matrix space, similar to perimeter but measured for a 3D volume. Since this is represented as a sum of surface areas of each pore in the sample, it is also affected by analysis volume and the Indi-8 sample is excluded.

Table 4.1: Pore count and interfacial area measurements for samples with normalized volumes.

Rock Sample	Pore Count	Total Interfacial Area (cm^2)
DP1-33	230,213	99
DP2-33	142,521	117
Indi-6	922,140	58
Indi-10	596,009	41
Indi-239	225,442	57
Trav-70	147,724	36
Trav-600	9,939	9

Note that when observing the values in each column of **Table 4.1**, it is possible to infer some information about the pore structure of the sample. For example, Indi-6 and Indi-239 samples both show similar total interfacial areas. However, the pore count is vastly different. Thus, the main contribution to pore surface area in Indi-6 is small pores, but the contribution in Indi-239 is from fewer, but much larger pores. This is confirmed qualitatively by observing the pore-size distribution shapes, and quantitatively by observing mean or median volume values for each sample (**Table 3.3**).

4.4.1 – Pore Volume Comparisons

In this section, mean and median volume measurements are compared with optimum acidizing parameters. See **Table 3.3** for values of these measurements. **Fig. 4.11** shows plots of $PV_{bt,opt}$ versus mean and median pore volume. Both of these plots are fit with logarithmic trendlines.

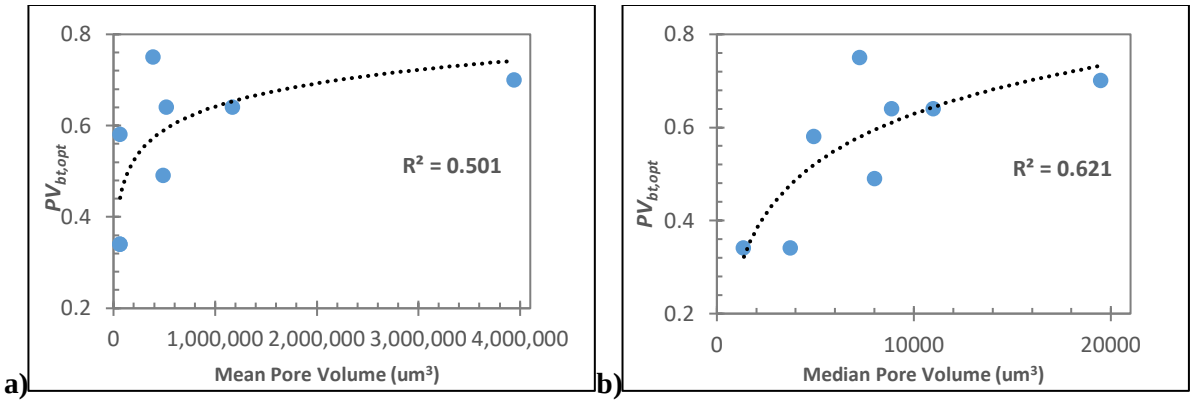

Figure 4.11: $PV_{bt,opt}$ *vs. a) mean pore volume and b) median pore volume (both fit with logarithmic trendlines).*

Optimum pore volume to breakthough shows good correlations in the above plots, especially the median pore volume (**Fig. 4.11b**). This is not entirely surprising, as pore volume tends to increase with pore diameter, which was earlier concluded to be positively related to $PV_{bt,opt}$.

Fig. 4.12 shows plots of $v_{i,opt}$ versus mean and median pore volume, both fit with exponential trendlines.

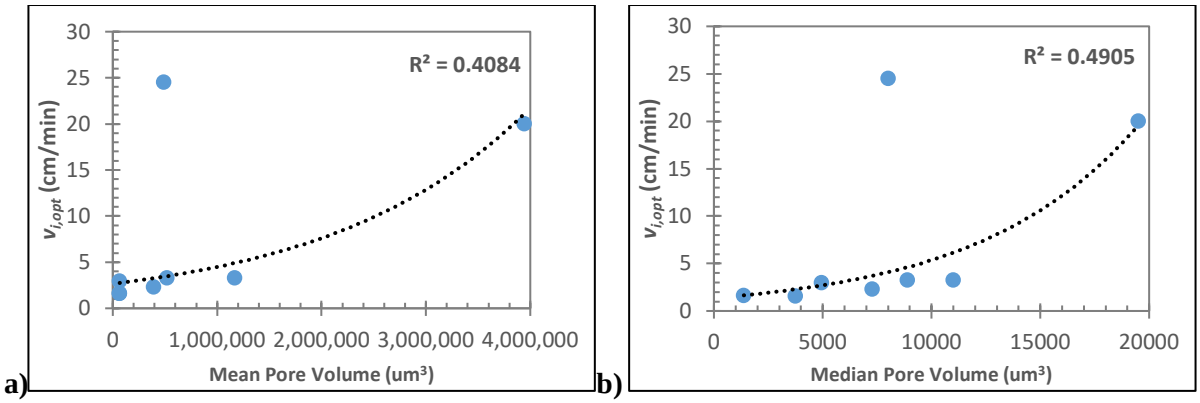

Figure 4.12*:* $v_{i,opt}$ *vs. a) mean pore volume and b) median pore volume (both fit with exponential trendlines).*

While Travertine samples remain outliers in the $v_{i,opt}$ plots, a positive correlation is noticeable in both comparison cases, especially the in the case of the non-Travertine samples. These plots are some of the better-correlated ones for optimum flux, according to the R^2 value.

4.4.2 – Pore Count Comparisons

Pore counts are listed in **Table 4.1** and plotted against optimum acidizing parameters in **Fig. 4.13** below.

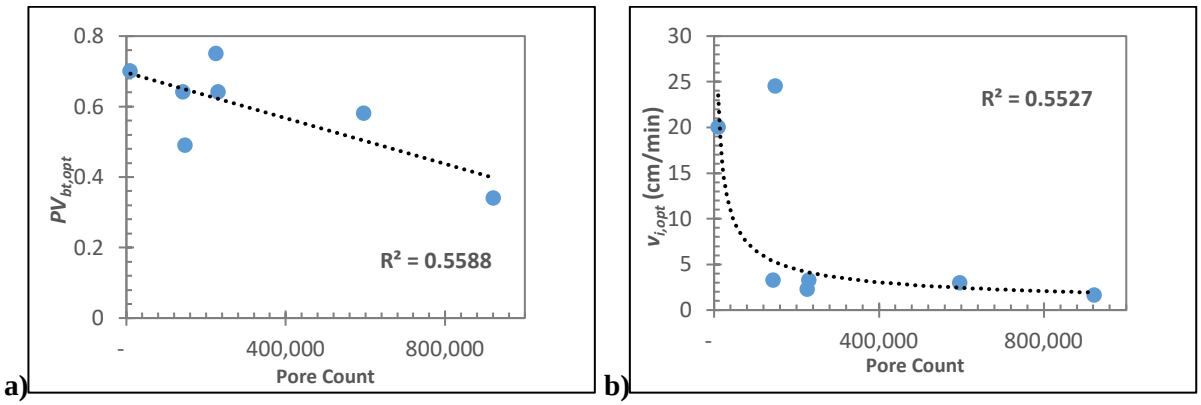

Figure 4.13: *Pore count comparisons for a)* $PV_{bt,opt}$ (linear trendline) *and b)* $v_{i,opt}$ (power-law trendline).

Both charts show a decrease in optimum conditions as pore count increases. However, the magnitude of change is much different. In the $PV_{bt,opt}$ case, a linear trend is observed while in the $v_{i,opt}$ case an power-law decrease is observed. In both cases, the R^2 values are fairly low for the given trendline, but a clear inverse relationship is observed, especially in the case of **Fig. 4.13a**. A possible explanation for the optimum breakthrough trend is that as pore count rises, permeability tends to decrease. This trend was found in the pore count results shown in **Table 4.1** across both Travertine and Indiana Limestone samples. For a given sample volume, a large pore count indicates small, discrete, unconnected pores. These samples have a lower permeability compared with samples with fewer large pores, and so the optimum breakthrough is lower since the acid can more easily find a preferred path in low-permeability samples. An explanation for optimum flux is more difficult, since there are not any conclusive trends in this paper from which to make a convincing argument. Since interstitial flux is inversely related to the area available for flow, a larger pore count could indicate either a higher porosity or a larger area available for fluid flow. Thus, according to the v_i equation (**Eq 4.1**), either of these conditions may indicate a smaller value of optimum interstitial flux.

$$vi = \left(\frac{q}{A * \phi}\right) \quad \text{.....(4.1)}$$

4.4.3 – Interfacial Area Comparisons

Fig. 4.14 shows plots of optimum acidizing parameters ($PV_{bt,opt}$ and $v_{i,opt}$) versus interfacial area.

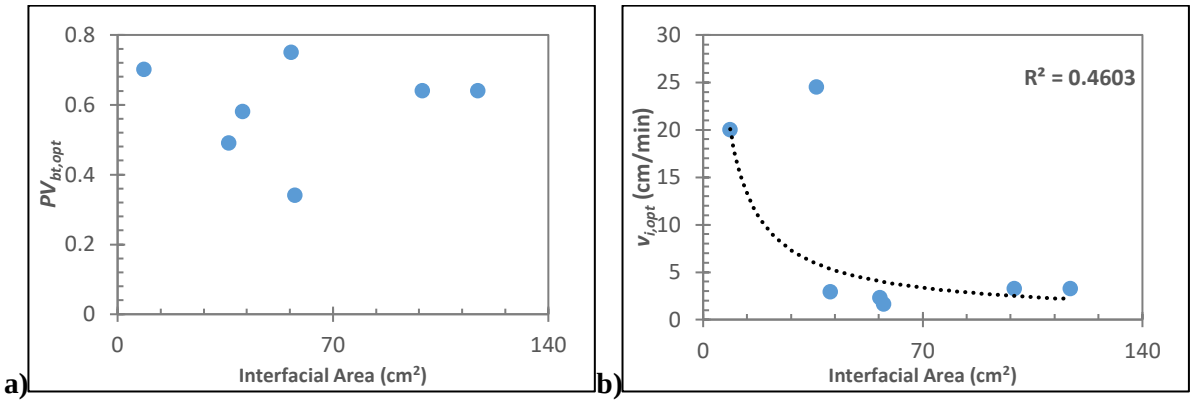

Figure 4.14: Interfacial area comparison with a) $PV_{bt,opt}$ *and b)* $v_{i,opt}$ (power-law trendline).

Optimum pore-volumes to breakthough show no discernable trend when compared with interfacial area. On the other hand, **Fig. 4.14b** shows an inverse relationship between interfacial area and optimum interstitial flux. This plot looks very similar to **Fig. 4.13b,** and since pore count is oftentimes related to interfacial area, a similar explanation for the $v_{i,opt}$ relationship in the previous case may explain the trend seen in **Fig. 4.13b.**

4.5 – Comments on Methodology

A unique aspect of this study was the use of two separate scales for experiments and comparison of results between these scales. Core-scale acidizing was performed to determine the optimum wormholing parameters, while small cubes were scanned with micro-CT to ultimately label individual pores and create pore-size distributions. As seen in **Table 2.2**, there is a discrepancy seen between the porosity of cores and some micro-CT samples. Specifically, the micro-CT porosities of Trav-70, Indi-239, and DP2-33 samples were significantly higher than the average core porosity to

which they were compared. For convenience, **Table 4.2** lists these three samples and shows the porosity discrepancy. Also listed are the number of cores used to create the efficiency curve, and thus the number of cores which the porosity is averaged over.

Table 4.2: Comparison of samples with high porosity variation between sample scales

Rock Sample	Average Core Porosity (%)	Micro-CT Sample Porosity (%)
DP2-33	25 (9 samples)	38
Trav-70	7 (4 samples)	17
Indi-239	16 (6 samples)	23

The explanation for the porosity discrepancy for Trav-70 and Indi-239 can be attributed to imprecise cutting of the sample cube. As can be seen in **Fig. 4.15,** chips of the rock face and corners were removed during drilling, which caused the bulk volume to be underestimated when calculating porosity. Due to this, calculated porosity of the cubes is higher than it should be.

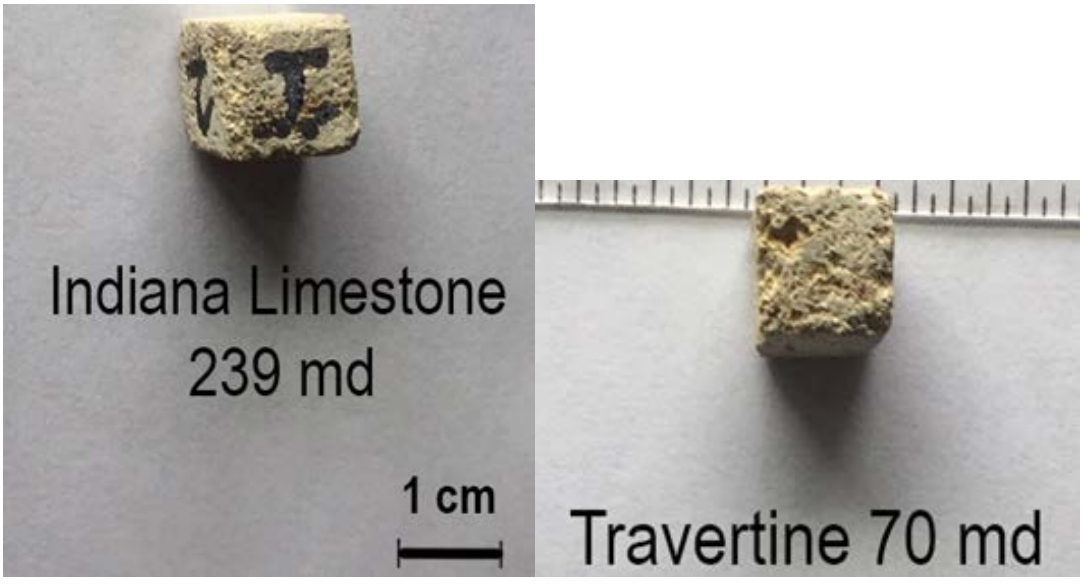

***Figure 4.15**: Indi-239 and Trav-70 samples show chips and wear along their surfaces.*

In the case of DP1-33, the cube was cut precisely, however by using the micro-CT image stacks to look inside the rock, a large vug was found. This can also be seen in the log-log pore-size distribution comparison (**Fig. 3.11**). This large internal chamber is an anomaly, but due to the small size of the cube it had a large effect on increasing the porosity of the sample. In general, small samples will tend to show larger porosity values than large samples. This is because anomalous effects (such as drill chippings or internal chambers) have a larger effect on porosity for a smaller-size volume (Ehrenberg, 2007). **Fig. 4.16** displays a plot from Ehrenberg's work (2007) comparing small 1 in. x 1 in. plug porosities with whole core porosities.

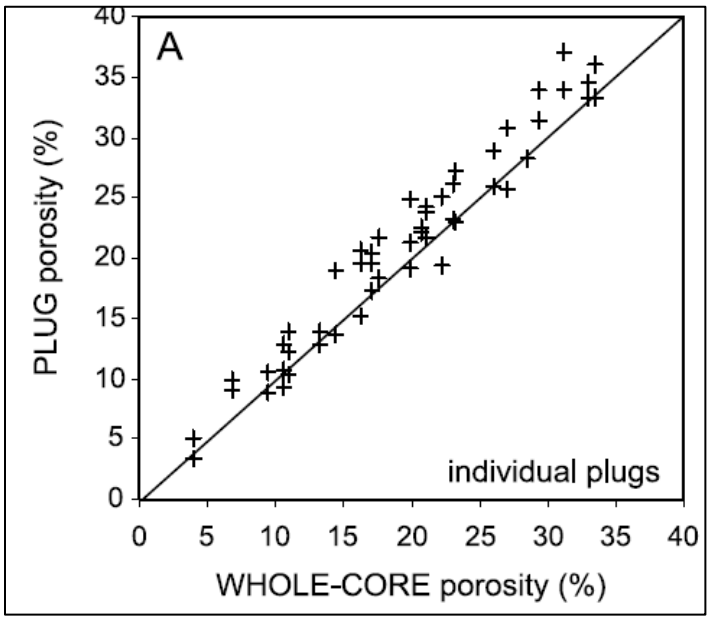

***Figure 4.16**: Size-dependency of porosity measurements from 1 in. diameter plugs vs. 3 in. diameter cores (Ehrenberg, 2007).*

Fig. 4.17 shows a similar plot to the one above from the current study, with core porosity on the *x*-axis and micro-CT sample porosity on the *y*-axis. While the extreme values of DP-2, Trav-70, and Indi-239 have been explained above, note that in general the porosity of smaller samples is larger than for the cores, which matches the work of Ehrenberg (2007).

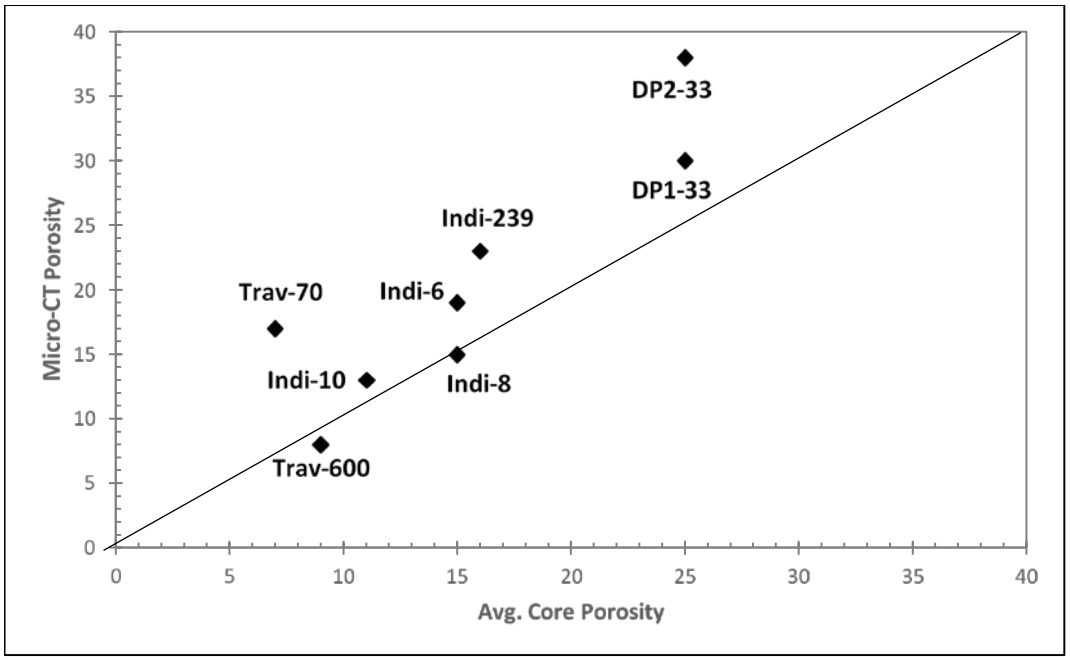

***Figure 4.17**: Micro-CT sample porosity vs. acidized core porosity. The plot shows that porosity measured for small samples tends to be higher than for larger scale samples in the current study.*

The higher porosities present in the micro-CT samples would likely have little effect on the semi-log representations of pore-size distributions presented in the study. As seen in the Desert Pink comparison (**Fig. 3.10**), despite the large increase of porosity of DP2-33 over DP1-33, (38% vs. 30%, respectively) the semi-log comparison of the two rocks remain virtually identical. It is only in the log-log comparison (**Fig. 3.11**) that we see the effect of the large vug in the DP2-33 sample. Observing **Table 3.5**, we see that the μ value for the two Desert Pink samples is very similar. The σ parameter, on the other hand, does change dramatically from DP1-33 to DP2-33. This indicates that changes in porosity affect the shape parameter more than the location parameter, which could be why there is a better correlation between μ parameter and $PV_{bt,opt}$ that with the σ parameter. Since no correlations were found between $v_{i,opt}$ and either μ *or* σ, we cannot say with certainty what the effect would be on the $v_{i,opt}$ correlation.

CHAPTER V

CONCLUSIONS AND RECOMMENDATIONS

5.1 – Conclusions

This study presents core acidizing data and pore-size distributions constructed from image analysis of digital micro-CT scans of various carbonate rock samples. In addition to qualitative comparison of pore-size distributions, a lognormal function was used to fit the distributions and optimize two variables, μ and σ, which were subsequently plotted against optimum acidizing parameters to search for useful correlations. The third part of this study compares measurements on individual pores derived from image analysis to enhance understanding of relationships between pore-scale features on optimum acidizing parameters. The conclusions of the study can be summarized as follows:

1. Pore structure of carbonate rocks affects optimum acidizing conditions and the effects of different pore structures can be visualized digitally by constructing pore-size distributions and comparing them qualitatively.
2. The image processing pipeline used in this work, including Otsu thresholding and Median blur 3D filtering, is sufficient to process raw Micro-CT images of resolutions ranging from 5 – 8 μm/voxel.
3. Rock pore-size distributions are sufficiently described by a lognormal distribution function, and fitting of this function can yield variables that show better correlations with optimum acidizing parameters than permeability or porosity alone.
4. Optimum pore-volumes to breakthough is positively correlated with pore size across all rock types studied in this work. Similarly definitive conclusions for optimum flux could not be made.
5. Micro-CT scanning combined with digital image analysis can yield pore-scale measurements difficult or impossible to obtain with conventional methods.

5.2 – Recommendations

After completion of this study, the following recommendations are made for future work in this field. The following points also encompass some limitations to the current study.

1. Open-source software used in this study was not specifically designed to quantify pores in complex geological media. If future studies are to be performed with the intent of constructing reliable, reproducible results, investment into premium software must be made.
2. This study was limited to pore-size distribution and analysis of simple pore measurements. Undoubtedly, optimum acidizing parameters are also related to heterogeneity and pore connectivity. Such measurements or processes (Euler number calculation, connected component labeling, nearest neighbor analysis) were attempted in this study with the open-source software available, but sufficient results were not obtained. To further enhance understanding of acidizing parameters, the means to perform connectivity analysis are absolutely necessary (see recommendation #1).
3. Future work relating to this thesis should focus on intermediate permeability samples, especially for Travertine and Indiana Limestone. Care must be taken in the acidizing process to minimize variance of core permeability for creation of acid efficiency curves to ensure the most accurate optimum parameters are obtained.
4. The procedures performed in this thesis should be extended to other carbonate rock types, such as Texas Cream Chalk and Winterset Limestone (at a range of permeabilities) to confirm or refute the results found in this study. Specifically, more data is needed to determine how optimum flux correlates to various pore-scale measures.

REFERENCES

Akanni, O. O. & Nasr-El-Din, H. A. (2015). The accuracy of carbonate matrix-acidizing models in predicting optimum injection and wormhole propagation rates. In *SPE Middle East Oil & Gas Show and Conference*. SPE-172575.

Andrä, H., Combaret, N., Dvorkin, J., Glatt, E., Han, J., et al. (2013). Digital rock physics benchmarks—part I: imaging and segmentation. *Computers & Geosciences, 50:* 25-32.

Bazin, B. (2001). From matrix acidizing to acid fracturing: a laboratory evaluation of acid/rock interactions. *SPE Production & Facilities, 16*(1), 22-29. SPE-66566-PA.

Bolte, S. & Cordelieres, F. P. (2006). A guided tour into subcellular colocalization analysis in light microscopy. *Journal of Microscopy, 224*(3), 213-232.

Buijse, M. A. & Glasbergen, G. (2005). A semi-empirical model to calculate wormhole growth in carbonate acidizing. In *SPE Annual Technical Conference and Exhibition*. SPE-96892-MS.

Buijse, M.A. (2000). Understanding wormholing mechanisms can improve acid treatments in carbonate formations. *SPE Production & Facilities, 15* (3), 168-175. SPE-65068-PA.

Cheng, H., Zhu, D., & Hill, A. D. (2016). The effect of evolved CO_2 on wormhole propagation in carbonate acidizing. In *SPE International Conference and Exhibition on Formation Damage Control*. SPE-178962-MS.

Costanza-Robinson, M. S., Estabrook, B. D., & Fouhey, D.F. (2011). Representative elementary volume estimation for porosity, moisture saturation, and air-water interfacial areas in unsaturated porous media: data quality implications. *Water Resources Research, 47*(7), W07513.

Daccord, G., Touboul, E., & Lenormand, R. (1989). Carbonate acidizing: toward a quantitative model of the wormholing phenomenon. *SPE Production Engineering, 4*(01), 63-68. SPE-16887-PA.

Dong, K. (2012). Experimental investigation for the effect of the core length on the optimum acid flux in carbonate acidizing. Master's thesis, Texas A&M University, College Station, Texas.

Dong, K. (2015). Theoretical and experimental study on optimal conditions in carbonate acidizing. Doctoral dissertation, Texas A&M University, College Station, Texas.

Dong, K., Jin, X., Zhu, D., & Hill, A. D. (2014). The effect of the core length on the optimum acid flux in carbonate acidizing. In *SPE International Symposium on Formation Damage Control*. SPE-168146-MS.

Economides, M. J., Hill, A. D., Ehlig-Economides, C., & Zhu, D. (2012). *Petroleum Production Systems*, second edition. Englewood Cliffs, New Jersey: PTR Prentice Hall.

Ehrenberg, S. N. (2007). Whole core versus plugs: Scale dependence of porosity and permeability measurements in platform carbonates. *AAPG bulletin 91*(6), 835-846.

Etten, J., Zhu, D., & Hill, A.D. (2015). The combined effect of permeability and pore structure on carbonate matrix acidizing. In *EUROPEC 2015*. SPE-174313-MS

Fredd, C. N. & Fogler, H. S. (1998). Influence of transport and reaction on wormhole formation in porous media. *AIChE Journal*, *44*(9), 1933-1949.

Fredd, C. N. & Fogler, H. S. (1999). Optimum conditions for wormhole formation in carbonate porous media: Influence of transport and reaction. *SPE Journal*, *4*(03), 196-205. SPE-56995-PA.

Fredd, C. N. & Miller, M. J. (2000). Validation of carbonate matrix stimulation models. In *SPE International Symposium on Formation Damage Control*. SPE-58713-MS.

Freire-Gormaly, M., Ellis, J. S., Bazylak, A., & MacLean, H. L. (2015). Comparing thresholding techniques for quantifying the dual porosity of Indiana Limestone and Pink Dolomite. *Microporous and Mesoporous Materials*, *207*, 84-89.

Furui, K., Burton, R. C., Burkhead, D. W., Abdelmalek, N. A., Hill, A. D., et al. (2010). A comprehensive model of high-rate matrix acid stimulation for long horizontal wells in carbonate reservoirs. In *SPE Annual Technical Conference and Exhibition*. SPE-134265.

Gharbi, O. & Blunt, M. J. (2012). The impact of wettability and connectivity on relative permeability in carbonates: a pore network modeling analysis. *Water Resources Research*, *48*(12), W12513.

Glasbergen, G., Kalia, N., & Talbot, M. S. (2009). The optimum injection rate for wormhole propagation: myth or reality? In *8th European Formation Damage Conference*. SPE-121464-MS.

Haralick, R. M., Sternberg, S. R., & Zhuang, X. (1987). Image analysis using mathematical morphology. *IEEE transactions on pattern analysis and machine intelligence*, (4), 532-550.

Hoefner, M. L. & Fogler, H. S. (1989). Fluid-velocity and reaction-rate effects during carbonate acidizing: application of network model. *SPE Production Engineering*, *4*(01), 56-62. SPE-15573-PA.

Huang, T., Hill, A. D., & Schechter, R. S. (1997). Reaction rate and fluid loss: The keys to wormhole initiation and propagation in carbonate acidizing. In *International Symposium on Oilfield Chemistry*. SPE-37312-MS.

Hung, K. M., Hill, A. D., & Sepehrnoori, K. (1989). A mechanistic model of wormhole growth in carbonate matrix acidizing and acid fracturing. *Journal of Petroleum Technology*, *41*(01), 59-66. SPE-16886-PA.

Iassonov, P., Gebrenegus, T., & Tuller, M. (2009). Segmentation of X-ray computed tomography images of porous materials: A crucial step for characterization and quantitative analysis of pore structures. *Water Resources Research*, *45*(9), W09415.

Izgec, O. (2009). Reactive flow in vuggy carbonates: methods and models applied to matrix acidizing of carbonates. Doctoral dissertation, Texas A&M University, College Station, Texas.

Izgec, O., Zhu, D., & Hill, A.D. (2010). Numerical and experimental investigation of acid wormholing during acidization of vuggy carbonate rocks. *Journal of Petroleum Science and Engineering*, *74*(1), 51-66.

Ji, Y., Baud, P., Vajdova, V., & Wong, T. F. (2012). Characterization of pore geometry of Indiana limestone in relation to mechanical compaction. *Oil & Gas Science and Technology–Revue d'IFP Energies Nouvelles*, *67*(5), 753-775.

Kalia, N., Mohanty, K., & Balakotaiah, V. (2006). Wormholing in radial flow. In *2006 AIChE Annual Meeting*. American Institute of Chemical Engineers.

Kosugi, K. (1999). General model for unsaturated hydraulic conductivity for soils with lognormal pore-size distribution. *Soil Science Society of America Journal*, *63*(2), 270-277.

Liu, M., Zhang, S., & Mou, J. (2012). Effect of normally distributed porosities on dissolution pattern in carbonate acidizing. *Journal of Petroleum Science and Engineering*, *94*, 28-39.

Lucia, F. J., Martin, A. J., Solomon, S. T., & Hartmann, D. J. (1999). Characterization of petrophysical flow units in carbonate reservoirs: Discussion. *AAPG bulletin*, *83*(7), 1161-1163.

Maheshwari, P., Ratnakar, R. R., Kalia, N., & Balakotaiah, V. (2013). 3-D simulation and analysis of reactive dissolution and wormhole formation in carbonate rocks. *Chemical Engineering Science*, *90*, 258-274.

Otsu, N. (1975). A threshold selection method from gray-level histograms. *Automatica*, *11*(285-296), 23-27.

Panga, M. K., Ziauddin, M., & Balakotaiah, V. (2005). Two-scale continuum model for simulation of wormholes in carbonate acidization. *AIChE Journal*, *51*(12), 3231-3248.

Ruzyla, K. (1986). Characterization of pore space by quantitative image analysis. *SPE Formation Evaluation*, *1*(04), 389-398. SPE-13133-PA.

Schechter, R. S. & Gidley, J. L. (1969). The change in pore size distribution from surface reactions in porous media. *AIChE Journal*, *15*(3), 339-350.

Schindelin, J., Arganda-Carreras, I., Frise, E., Kaynig, V., Longair, M., et al. (2012), "Fiji: an open-source platform for biological-image analysis", *Nature Methods*, *9*(7): 676-682, PMID 22743772

Sezgin, M. (2004). Survey over image thresholding techniques and quantitative performance evaluation. *Journal of Electronic Imaging*, *13*(1), 146–165.

Wand, M. P. (1997). Data-based choice of histogram bin width. *The American Statistician*, *51*(1), 59-64.

Wang, Y., Hill, A. D., & Schechter, R. S. (1993). The optimum injection rate for matrix acidizing of carbonate formations. In *SPE Annual Technical Conference and Exhibition*. SPE-26578-MS.

Youssef, S., Rosenberg, E., Gland, N. F., Kenter, J. A., Skalinski, M., et al., (2007). High resolution CT and pore-network models to assess petrophysical properties of homogeneous and

heterogeneous carbonates. In *SPE/EAGE Reservoir Characterization and Simulation Conference*. SPE-111427-MS.

Zakaria, A. S., Nasr-El-Din, H. A., & Ziauddin, M. (2015). Predicting the performance of the acid-stimulation treatments in carbonate reservoirs with nondestructive tracer tests. *SPE Journal*. SPE-174084-PA.

Ziauddin, M.E. & Bize, E. (2007). The effect of pore scale heterogeneities on carbonate stimulation treatments. In *SPE Middle East Oil and Gas Show and Conference.* SPE-104627-MS.